LECTURES ON TROPICAL CYCLONES

Roger K. Smith

Date: June 2, 2006

Contents

Chapter 1

OBSERVATIONS OF TROPICAL CYCLONES

Tropical cyclones are intense, cyclonically[1]-rotating, low-pressure weather systems that form over the tropical oceans. Intense means that near surface sustained[2] wind speeds exceed 17 ms^{-1} (60 km h^{-1}, 32 kn). Severe tropical cyclones with near surface sustained wind speeds equal to or exceeding 33 ms^{-1} (120 km h^{-1}, 64 kn) are called hurricanes over the Atlantic Ocean, the East Pacific Ocean and the Caribbean Sea, and Typhoons over the Western North Pacific Ocean. Typically the strongest winds occur in a ring some tens of kilometres from the centre and there is a calm region near the centre, the eye, where winds are light, but for moving storms, the wind distribution may be asymmetric with the maximum winds in the forward right quadrant. The eye is so-called because it is normally free of cloud, except perhaps near the surface, but in a mature storm it is surrounded by a ring of deep convective cloud that slopes outwards with height. This is the so-called eyewall cloud. At larger radii from the centre, storms usually show spiral bands of convective cloud. Figure 1.1 shows a satellite view of the eye and eyewall of a mature typhoon, while Fig. 1.2 shows photographs looking out at the eyewall cloud from the eye during aircraft reconnaissance flights.

1.1   Structure

The mature tropical cyclone consists of a horizontal quasi-symmetric circulation on which is superposed a thermally-direct[3] vertical (transverse) circulation. These are sometimes referred to as the *primary* and *secondary* circulations, respectively, terms which were coined by Ooyama (1982). The combination of these two component circulations results in a spiralling motion. Figure 1.3 shows a schematic cross-section

---

[1]Cyclonic means counterclockwise (clockwise) in the northern (southern) hemisphere.

[2]The convention for the definition of sustained wind speed is a 10 min average value, except in the United States, which adopts a 1 min average.

[3]Thermally direct means that warm air rising, a process that releases potential energy.
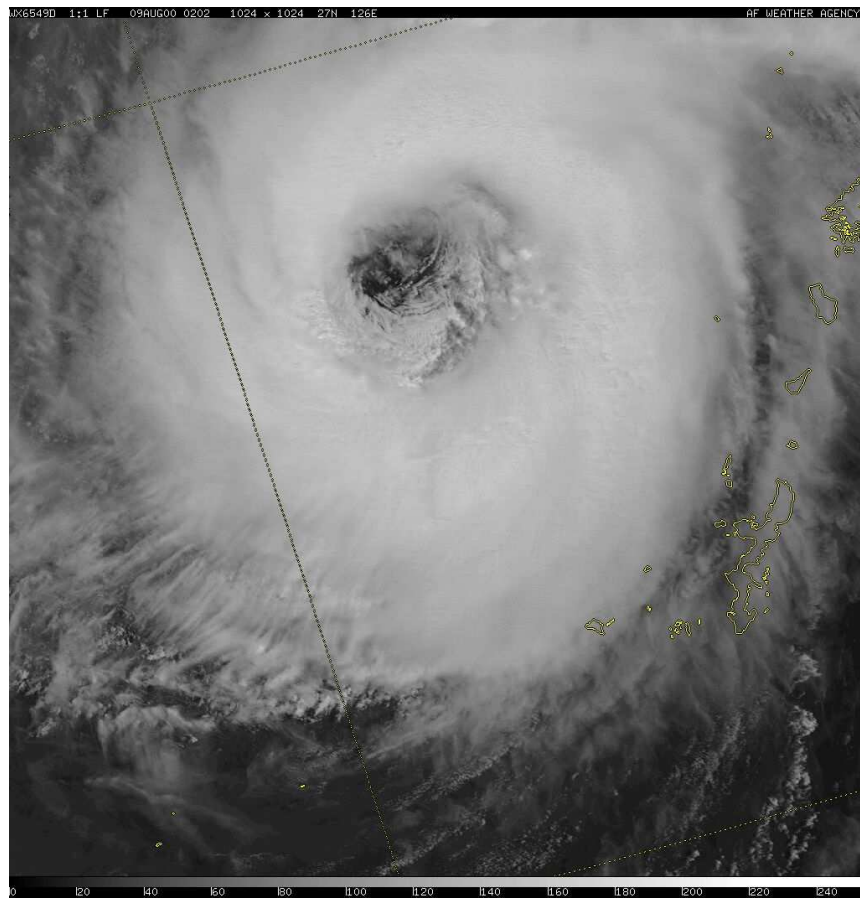
Figure 1.1: Infra-red satellite imagery of a typhoon.

of prominent cloud features in a mature cyclone including the eyewall clouds that surround the largely cloud-free eye at the centre of the storm; the spiral bands of deep convective outside the eyewall; and the cirrus canopy in the upper troposphere. Other aspects of the storm structure are highlighted in Fig. 1.4. Air spirals into the storm at low levels, with much of the inflow confined to a shallow boundary layer, typically 500 m to 1 km deep, and it spirals out of the storm in the upper troposphere, where the circulation outside a radius of a few hundred kilometres is anticyclonic. The spiralling motions are often evident in cloud patterns seen in satellite imagery and in radar reflectivity displays. The primary circulation is strongest at low levels in the eyewall cloud region and decreases in intensity with both radius and height as shown by the isotachs of mean tangential wind speed on the right-hand-side of the axis in Fig. 1.4. Superimposed on these isotachs are the isotherms, which show the warm core structure of the storm, with the largest temperatures in the eye. Outside the eye, most of the temperature excess is confined to the upper troposphere.

On the left side of the axis in Fig. 1.4 are shown the isolines of equivalent potential temperature, θ_e, referred to also as the moist isentropes. Note that there

(a)

(b)

Figure 1.2: Aerial photographs of the eye wall looking out from the eyes of (a) Hurricane Allen (1983), and (b) Typhoon Vera (19xx)

is a strong gradient of θ_e in the eyewall region and that the moist isentropes slope radially outwards with height. This important feature, which we make use of in discussing the dynamics of tropical cyclones in section 2.10, is exemplified also by the θ_e-structure observed in Hurricane Inez (1966), shown in Fig. 1.5. Since θ_e is approximately conserved in moist flow, even in the presence of condensation, the pattern of the isentropes reflects the ascent of air parcels in the eyewall from the boundary layer beneath to the upper-level outflow. The large inward radial gradient of θ_e is a consequence of the rapid increase in the moisture flux from the ocean on account of the rapid increase of wind speed with decreasing radius as the eyewall is

approached.
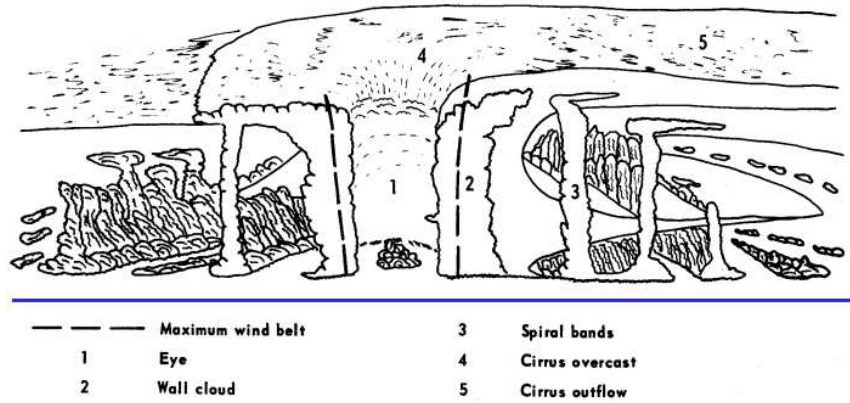
Figure 1.3: Schematic cross-section of cloud features in a mature tropical cyclone. Vertical scale greatly exaggerated. (From Gentry, 1973)
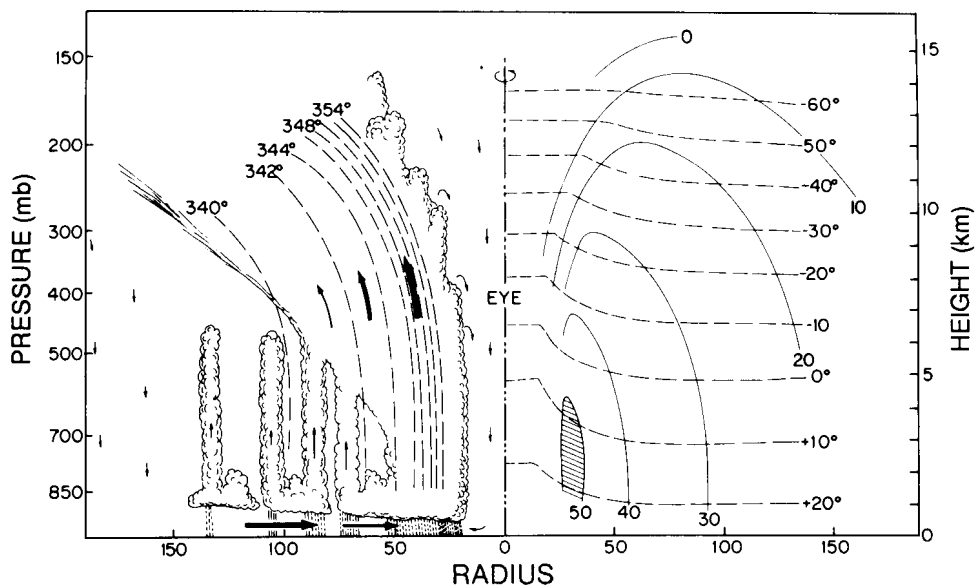
Figure 1.4: Radial cross-section through an idealized, axisymmetric hurricane. On left: radial and vertical mass fluxes are indicated by arrows, equivalent potential temperature (K) by dashed lines. On right: tangential wind speed in m s^{-1} is indicated by solid lines and temperature in ^{o}C by dashed lines. (From Wallace and Hobbs, 1977 and adapted from Palmén and Newton, 1969)

The "classical" structure of a tropical cyclone core is exemplified by that of Hurricane Gilbert at 2200 UTC on 13 September 1988. At this time Gilbert was an
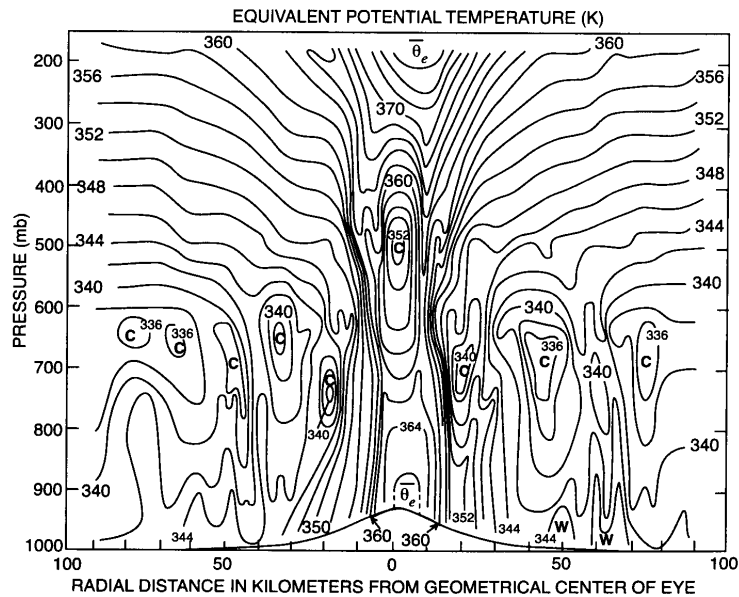
Figure 1.5: Vertical cross-sections of equivalent potential temperature (K) in Hurricane Inez of 1964 (From Hawkins and Imbembo 1976)

intense hurricane with a maximum wind speed in excess of 80 m s^{-1} and it had the lowest sea-level pressure ever measured (888 mb) in the Western Hemisphere. The following description is adapted from that of Willoughby (1995). The storm was especially well documented by data gathered from research aircraft penetrations.

1.1.1 Precipitation patterns, radar observations

A composite of radar reflectivity observed in Gilbert's core from one of the research aircraft is shown in Fig. 1.6. The eye is in the center of the picture, and is surrounded by the eyewall with maximum radar reflectivities of 40-47 dBZ[4]. The reflectivity in the eye is below the minimum detectable signal for the radar. During the flight, visual observation showed the eye to be free of clouds at and above flight level with blue sky visible overhead. Below flight level, broken stratocumulus in the lowest 1 km of the eye partially obscured the sea surface. In the radar image, the radius from the centre of the eye to the inner edge of the eyewall is about 8 km. The outer edge of the eyewall is less than 20 km from the center. Surrounding the eyewall is a "moat" where the reflectivities are less than 25 dBZ, which is equivalent to a factor of more than 100 lower rainfall rates than in the eyewall. As the aircraft flew across the moat at 3 km altitude, it was in rain beneath an overcast sky, and low stratocumulus obscured the surface. Beyond the outer edge of the moat (75 km from

---

[4]The decibel, abbreviated dBZ is a measure of the intensity of the backscattered radar beam and is related to the intensity of precipitation in the storm.
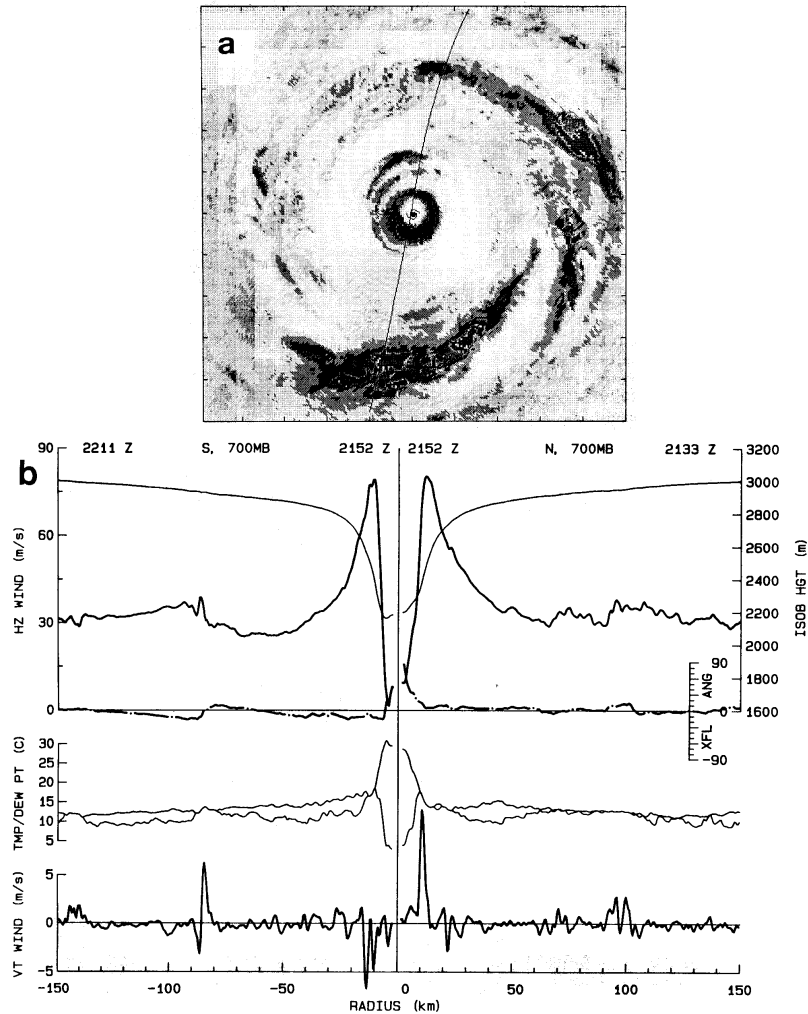
Figure 1.6: (a) Plan-position indicator (PPI) radar reflectivity composite of Hurricane Gilbert at about 2200 UTC on 13 September 1988, when it was at maximum intensity near 19.9N, 83.5W. (b) Fight-level measurements from research aircraft. The abscissa is distance along a north-south pass through the centre. The top panel shows wind speed (dark solid line), 700 mb height (light solid line), and crossing angle ($\tan^{-1} u/v$, dash-dotted line). Winds are relative to the moving vortex centre. The middle panel shows temperature (upper curve) and dewpoint. When $T_D > T$, both are set to $\frac{1}{2}(T + T_D)$. The bottom panel shows vertical wind. (From Black and Willoughby 1992)

the centre), the radar image shows precipitation organized into spirals that appear to be coalescing into a second ring of convection around the inner eye. Whereas the maximum reflectivities in the spirals are about 45 dBZ, which is a value comparable with that in the eyewall, reflectivities are ≤ 30 dBZ over much of the area

outside the moat. Radar shows patterns of precipitation, but radar images contain important clues for visualization of the flow also. Echo-free areas, such as the eye and the moat, generally indicate vortex-scale descent. The highly reflective echoes contain both convective updrafts and precipitation-induced downdrafts. The individual echoes may be arranged in rings that encircle the centre, or in open spirals. The lower reflectivities over most of the rings and spirals are stratiform rain falling from overhanging anvil cloud; the higher reflectivities are embedded convective cells. Based upon a typical radar reflectivity-rainfall relationship[5] the rainfall rate is less than 4 mm h^{-1} in the stratiform areas and greater than 45 mm h^{-1} in the strong convective cells, which typically cover only a few percent of the hurricane as a whole. Corresponding radial profiles of flight-level wind, 700 mb geopotential height, temperature, and dewpoint observed by the aircraft are shown in Fig. 1.6b. These are discussed below.

1.1.2 Wind structure

The strongest horizontal wind (> 80 m s^{-1}) is in the eyewall, only 12 km from the calm at the axis of rotation. This is typical of a tropical cyclone, although in weaker storms the radius maximum wind speed is larger, ranging up to 50 km or more. Outside the eyewall, the wind drops abruptly to about 30 m s^{-1} at the outer edge of the moat and then rises to 35 m s^{-1} in the partial band of convection surrounding the moat. The cross-flow angle ($\tan^{-1} u/v$, where u and v are the radial and tangential wind components) at 700 mb is $< 10^o$. There is a tendency for radial flow toward the wind maxima from both the inside and the outside, which indicates that the horizontal wind converges into these features, even in the mid-troposphere. Not surprisingly, convective-scale vertical motions (updrafts), or on the south side of the eyewall in this case, downdrafts, often lie where the inflows and outflows converge just a kilometer or two radially outward from the horizontal wind maxima. The strongest vertical motions, even in this extremely intense hurricane, are only 5-10 m s^{-1}. There is a statistical tendency for the downdrafts to lie radially outward from the updrafts, as occurs, for example, 80 km south of Gilbert's centre.

1.1.3 Thermodynamic structure

The air temperature shows a steady rise as the aircraft flies inwards towards the eyewall and then a rapid rise as it enters the eye. Thus the warmest temperatures are found in the eye itself, not in the eyewall clouds where the latent heat occurs. These warm temperatures must arise, therefore, from subsidence in the eye. The dynamics of the eye and the reasons for this subsidence are discussed in section 2.7.

At most radii in Fig. 1.6b, the dewpoint depression[6] is on the order of 4°C.

---

[5]$Z = 300R^{1.35}$, where Z is the reflectivity (in mm^6 m^{-3}) and R is the rainfall rate (mm h^{-1}); see Jorgensen and Willis 1982

[6]The difference between the temperature and the dewpoint temperature
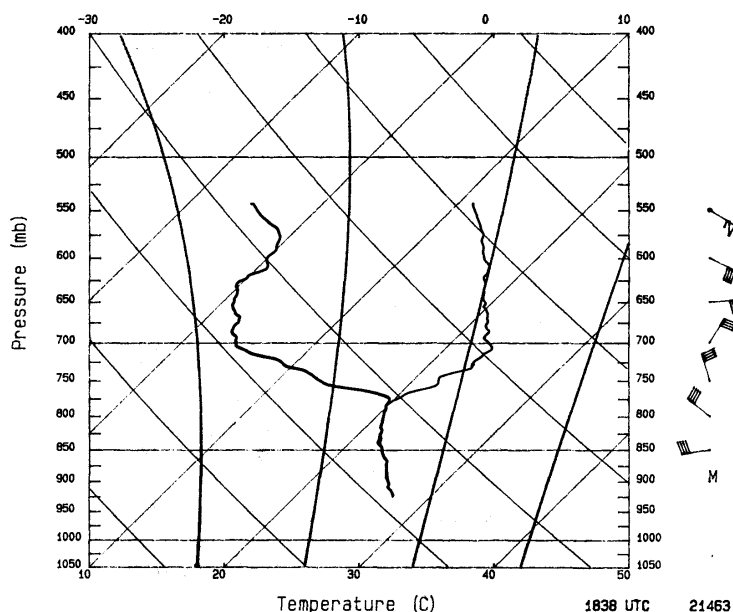
Figure 1.7: A dropsonde observation in the eye of Hurricane Hugo, near 14.7°N 54.8°W at 1838 UTC September 1989. Temperature is the right hand curve and dewpoint is the left. Nearly vertical curving lines are moist adiabats. Lines sloping up to the left are dry adiabats; those sloping up to the right are isotherms; and horizontal lines are isobars (From Willoughby 1995).

The air is saturated only where convective vertical motions pass through flight level. Inside the eye, the temperature is greater than 28°C and the dewpoint is less than 0°C. These warm and dry conditions are typical of the eyes of extremely intense tropical cyclones. A sounding in the eye of Hurricane Hugo on 15 September 1989, when its structure was much like Gilbert's even though its central pressure was 34 mb higher, is shown in Fig. 1.7. An inversion at 700 mb separates air with a dewpoint depression of about 20°C from saturated air that follows a moist adiabat down to the sea surface. Above the inversion, the air detrains from the eyewall near the tropopause and flows downward as part of a thermally indirect, forced subsidence in the eye. It is moistened a little by entrainment from the eyewall and evaporation of virga. Below the inversion, the air is cooler and nearly saturated as a result of inflow under the eyewall, inward mixing, and evaporation from the sea inside the eye.

1.1.4 Vertical cross-sections

Research aircraft transects in Hurricane Hilda 1964 were obtained at five different levels enabling the vertical structure of the storm to be documented. Cross-sections of azimuthal wind and temperature anomaly are shown in Fig. 1.8. Again, as is typical, the primary circulation in Hurricane Hilda (Fig. 1.8a) is strongest just

above the frictional boundary layer. Below 500 mb, it has little vertical shear, but in the upper troposphere, it becomes weaker and less symmetric, and the radial outflow is a large fraction of the swirling motion. Near the tropopause beyond 200 km radius, the vortex turns anticyclonic because of angular momentum loss to the sea on the inflow leg of the secondary circulation (Riehl 1963).
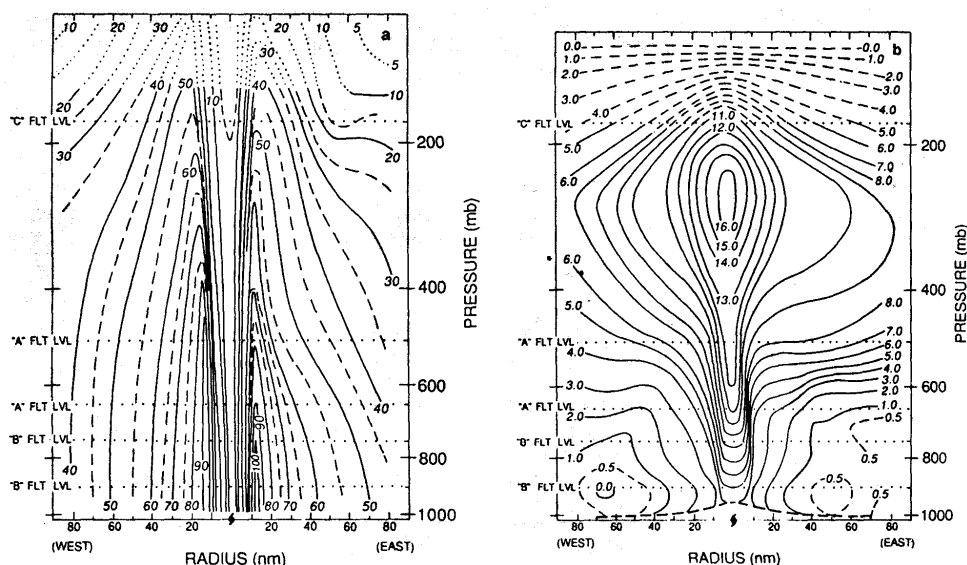
Figure 1.8: Vertical cross-sections of (a) azimuthal wind (kt), and (b) temperature anomaly (K) in Hurricane Hilda of 1964 (From Hawkins and Rubsam 1968)

Figure 1.9 illustrates a schematic secondary circulation in a tropical cyclone such as Gilbert. This circulation is forced by an intense frictional destruction of angular momentum at the surface (section 2.8), by strong latent heat release in the inner eyewall clouds (section 2.5), weaker heating in the outer eyewall clouds, and extensive but weak cooling caused by frozen precipitation melting along the radar bright band[7], and similarly extensive and weak heating due to condensation and freezing in the anvil above the bright band.

The low-level inflow in the heating-induced thermally direct gyres in Fig. 1.9 is distinct from the frictional inflow - see Fig. 1.10 below. The swirling wind in the friction layer is generally a little weaker than that just above. Thus, only the heating-induced inflow can supply an excess of angular momentum beyond that required to balance frictional loss. Observations show that the eyewall updrafts slope outward along constant angular momentum surfaces (Jorgensen 1984a,b; Marks and Houze 1987). The updraft slope from the vertical is the ratio of the vertical shear to the vertical component of the vorticity (Palmén 1956) and has typical values of 30°-60°

---

[7]The bright band is a layer seen in vertical radar scans through cloud and coincides with the melting layer just below the 0^oC isotherm. Melting ice particles have enhanced reflectivity.
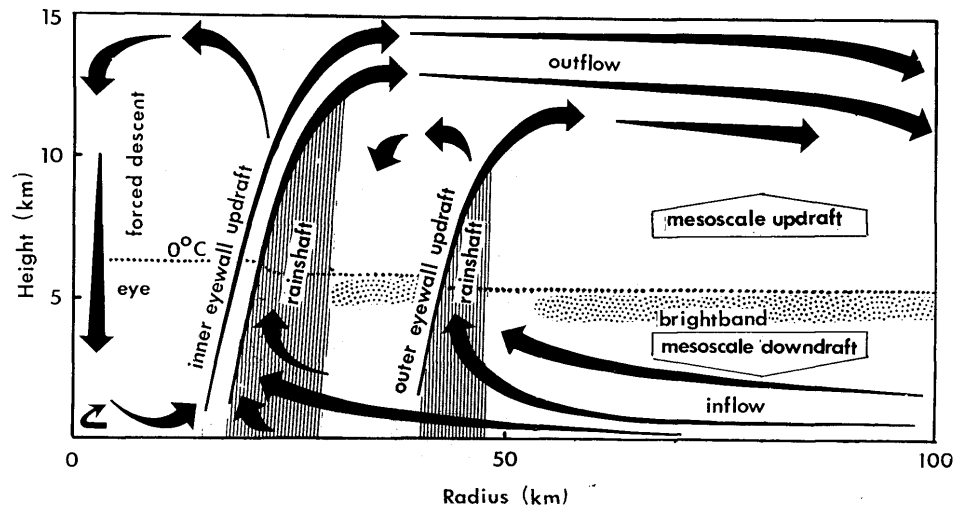
Figure 1.9: Schematic of the secondary circulation and precipitation distribution for a tropical cyclone similar to Hurricane Gilbert at the time in Fig. 1.6. (From Willoughby 1988)

(Black 1993), contrary to some claims that eyewalls are vertical (e.g. Shea and Gray 1973).

Outside the eye, latent heat release above the 0°C isotherm drives mesoscale updrafts. Below the 0°C isotherm, condensate loading and cooling due to melting of frozen hydrometeors drive mesoscale downdrafts. The mesoscale vertical velocities are typically tens of centimeters per second.

The secondary circulation controls the distribution of hydrometeors and radar reflectivity. Ascent is concentrated in convective updraft cores, which typically cover 10% of the area in the vortex core and more than half of the eyewall. The vertical velocity in the strongest 10% of the updraft cores averages 3-5 m s^{-1}. Except for "supercell storms"[8] sometimes observed in tropical storms (Gentry *et al.* 1970; Black 1983), convective cells with updrafts > 20 m s^{-1} appear to be rare. Much of the condensate falls out of the outwardly sloping updrafts, so that the rain shafts are outside and below the region of ascent. The eyewall accounts for 25%-50% of the rainfall in the vortex core, but perhaps only 10% of the rainfall in the vortex as a whole. In the rain shafts, precipitation loading and, to a lesser extent, evaporation force convective downdrafts of a few meters per second. Any condensate that remains in the updrafts is distributed horizontally in the upper troposphere by the outflow. It forms the central dense overcast that usually covers the tropical cyclone's core, and much of it ultimately falls as snow to the melting level where it forms the radar brightband. Nearly all the updrafts glaciate by -5°C because of ice multiplication and entrainment of frozen hydrometeors (Black and Hallett 1986).

---

[8]A supercell storm is one which has a single intense rotating updraft.

Above the boundary layer, the secondary circulation and distributions of radar reflectivity and hydrometeors are much like those in a tropical squall line (Houze and Betts 1981). They have the same extensive anvil, mesoscale up- and downdrafts, and brightband. The boundary layer flows and energy sources are, however, much different. As a squall line propagates, it draws its energy from the water vapour stored in the undisturbed boundary layer ahead of it, and leaves behind a cool wake that is capped by warm, dry mesoscale downdraft air under the anvil. However, as an eyewall propagates inward, but draws energy primarily from behind (outward) rather than ahead (inward). Frictional inflow feeds the updraft with latent heat extracted from the sea under the anvil. The reason for the difference between an eyewall and a squall line is the increased rate of air-sea interaction in the strong primary circulation of a tropical cyclone.

1.1.5 Composite data

Because of the difficulty and expense of gathering enough data for individual storms to construct vertical cross-sections such as those in Figs. 1.5 and 1.8, composite data sets have been constructed on the basis of data collected for very many similar storms at many time periods. The technique was pioneered by W. Gray and collaborators at the Colorado State University and is explained by Frank (1977). The idea is to construct eight octants of 45° azimuthal extent and eight radial bands extending from 0-1°, 1-3°, 3-5°, 5-7°, 9-11°, 11-13° and 13-15°. Data from individual soundings are assigned to one of these subregions according to their distance and geographical bearing relative to the storm centre. The data in these subregions are then averaged to define a composite storm.

Vertical cross-sections of the mean radial and tangential wind components in hurricanes, based on composite data from many storms are shown in Figs. 1.10. Note that the radial wind component increases inwards with decreasing radius at low levels, is inward but relatively small through the bulk of the troposphere and is outward in the upper troposphere.

1.1.6 Strength, intensity and size

It is important to distinguish between the "intensity" of the cyclone core and the "strength" of the outer circulation. Intensity is conventionally measured in terms of maximum wind or minimum sea-level pressure; strength is a spatially-averaged wind speed over an annulus between 100 and 250 km from the cyclone centre. Another useful parameter is size, which may be defined as the average radius of gale force winds ($\geq$17 m s^{-1}), or of the outer closed isobar (ROCI). Observations show that size and strength are strongly correlated, but neither is strongly correlated with intensity.

The climatology of size is well established for the Atlantic and North Pacific. On average, typhoons are 1.5° lat. larger than Atlantic hurricanes. Small tropical cyclones (ROCI < 2° lat.) are most frequent early in the season (August), and large
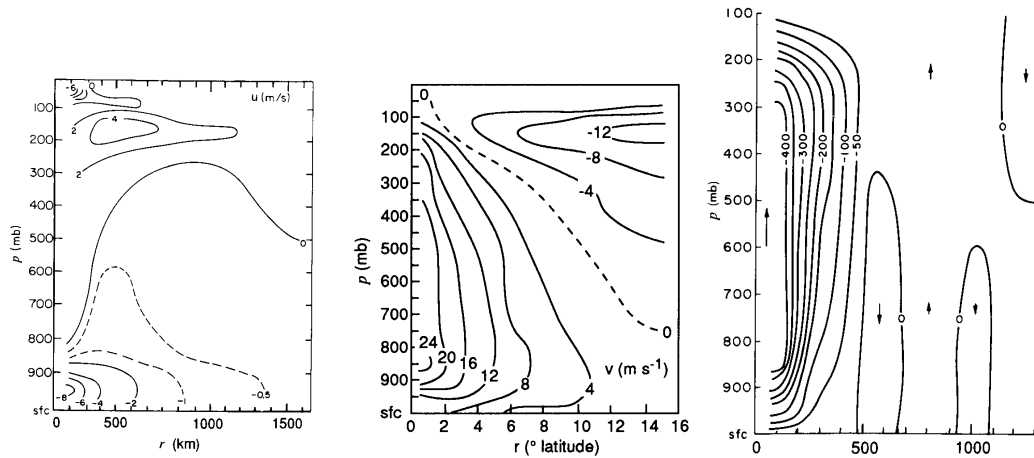
Figure 1.10: (From Gray, 1979; Frank 1977)

ones (ROCI > 10° lat.) late in the season (October). Large tropical cyclones are most common at 30°N, which is the average latitude of recurvature.

The life cycle of an Atlantic tropical cyclone begins with a formative stage during which the outer circulation contracts a little as the core intensifies. During the immature stage, the intensity increases to a maximum as the size remains constant. In the mature stage, the tropical cyclone grows, but no longer intensifies. In the decaying stage, the inner core winds decrease as the circulation continues to grow. The ROCI is typically 2.5° lat. in the immature stage and twice that value in the decaying stage a week e maximum intensity, start of rapid growth, and recurvature[9] of the track tend to coincide.

A detailed study of reconnaissance aircraft data from the western North Pacific confirms the low correlation between strength and intensity, and essentially no correlation between time changes in strength and intensity. That is, strength is equally likely to increase or decrease as a typhoon intensifies. Commonly, intensification precedes strengthening, and weakening of the core precedes that of the outer circulation. Classification of the observations by eye size [small (radius ≤ 15 km), medium (16-30 km), large (30-120 km), and eyewall absent] reveals correlations between intensity and strength, even though none could be found for the sample as a whole. These correlations may become evident because eye size acts as a proxy for phase of the typhoon life cycles.

Some relevant references are: Brand 1972; Merrill 1984; and Weatherford and Gray 1988a,b)

---

[9]See section 1.XX
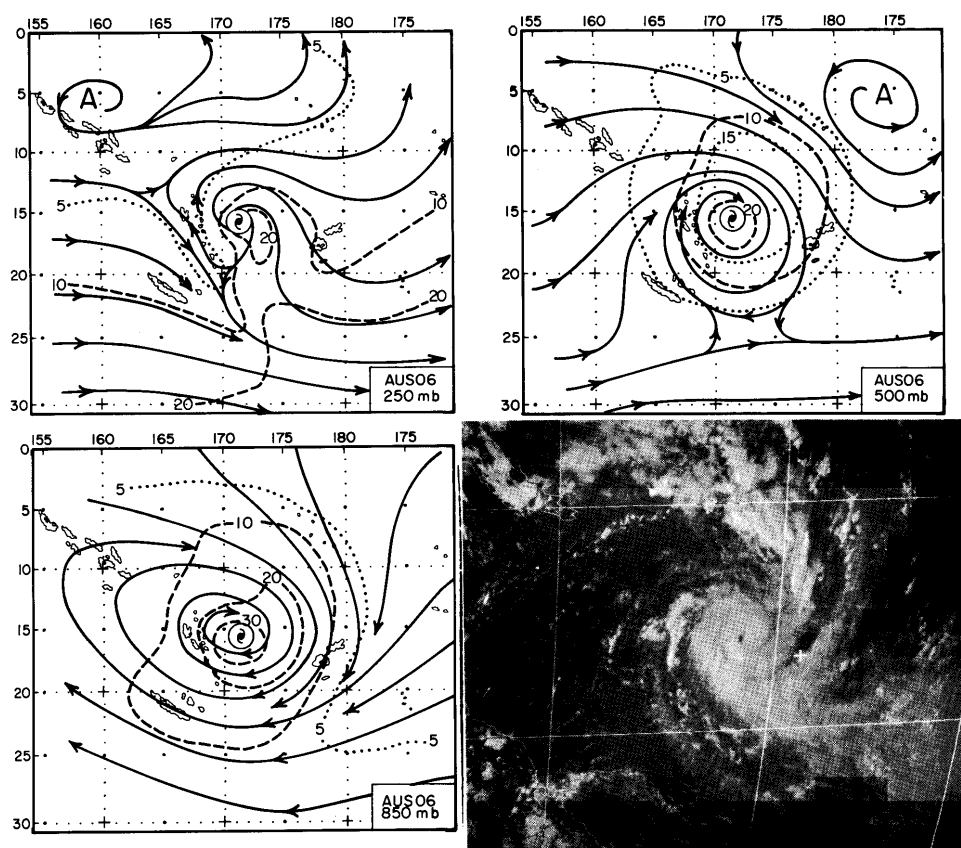
Figure 1.11: Streamline isotach analyses at 250, 500, and 850 mb for a composite Southern Hemisphere tropical cyclone, together with a typical visible satellite image. (From Holland 1984)

1.1.7 Asymmetries

Normally only the inner-core regions of intense tropical cyclones show a significant degree of axial-symmetry. As shown in Fig. 1.11 for a Southern Hemisphere cyclone, the axisymmetric core is typically surrounded by a less symmetric outer vortex that merges into the synoptic environment. In the lower troposphere, the cyclonic circulation may extend more than 1000 km from the centre. The boundary between cyclonic and anticyclonic circulation slopes inward with height, so that the circulation in the upper troposphere is primarily anticyclonic except near the centre. The flow asymmetries in this region have a significant effect on the vortex motion (Chapter 5). In tropical cyclones that originate in the monsoon trough, the asymmetric flow is often associated with a band of convection that joins the cyclone to the trough (Holland 1984).

Spiral-shaped patterns of precipitation characterize radar and satellite images of tropical cyclones (Fig. 1.12). The earliest radar observations of tropical cyclones

detected these bands, which are typically 5-50 km wide and 100-300 km long. Nevertheless, many aspects of their formation, dynamics, and interaction with the symmetric vortex are still unresolved. The precipitation-free lanes between bands tend to be somewhat wider than the bands. As the tropical cyclone becomes more intense, the inward ends of the bands approach the center less steeply and then approximate arcs of circles.
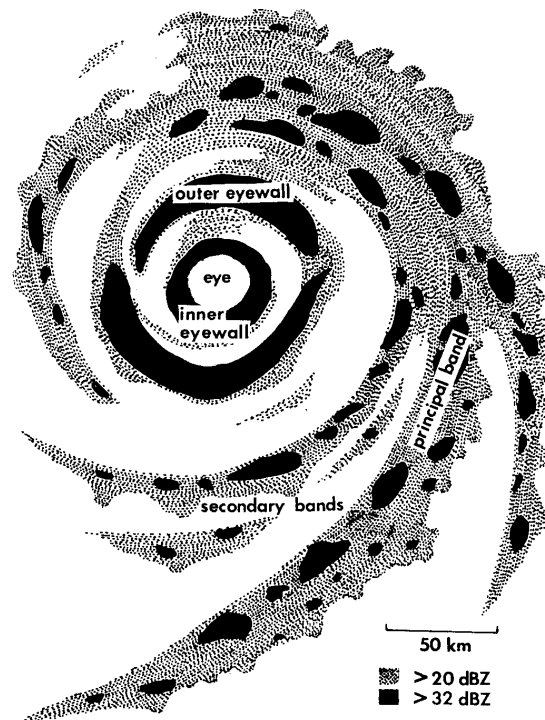
Figure 1.12: Typical banded radar reflectivity pattern in a Northern Hemisphere tropical cyclone with 50-60 m s^{-1} maximum wind in a sheared environmental flow (From Willoughby 1988)

A dynamical distinction exists between convective bands that spiral outward from the center and convective rings that encircle the center. Because the bands often join a ring or appear to wrap around the centre (Dvorak 1984), this distinction is often difficult to make in radar or satellite images.

Although precipitation in some bands is largely from stratiform clouds, condensation in most bands tends to be concentrated in convective cells rather than spread over wide mesoscale areas. Convective elements form near the inner, upwind edges of the bands, move through the bands, and dissipate on the outward, downwind edges. As the cells cross the band, they also move inward along the band. The dissipating elements feed an extensive anvil and generate widespread stratiform precipitation through horizontal advection of convective debris.

Some key observational studies of spiral bands are summarized by Willoughby

(1995), who gives a comprehensive list of references.

Dual-Doppler radar observations of a rainband in Supertyphoon Abby 1983 confirmed inflow from the inward (concave) side, a locus of mesoscale ascent along the concave edge of the band, and a locus of mesoscale descent along the outer (convex) side. This pattern of inflow stemmed from the band's steep inward crossing angle of 25°. The roots of the updrafts lay in convergence between the swirling flow and gust fronts that are produced by the downdrafts. The updrafts leaned outward from the typhoon center toward the convex side of the band and fed an extensive anvil that spread downwind from the band. The band moved more slowly than the surrounding winds, i.e., it propagated upwind. Even though the band was over land at 36°N, the equivalent potential temperature at the surface was 355 K, and this band should be considered representative of squall-line bands in hurricanes.

These Abby observations contrast with aircraft and radar observations of a "band" in Hurricane Floyd 1981. In the Floyd case, the low-level air spiraled inward more steeply than the band, so that the band intercepted the radial inflow on its outer, convex side. The inflow passed under the anvil between the convective-scale, precipitation-driven downdrafts to feed an updraft on the inner, concave side of the band. As in Typhoon Abby, the updraft sloped outward over the downdraft and fed an anvil extending away from the tropical cyclone center. The 20∘K decrease in low-level θ_e across the band indicates that the band was a barrier to inflow. Independent observations in Hurricane Earl emphasized that cooling and shallowing of the boundary layer occurred as the vortex-scale inflow passed under or between the cells of the bands (Fig. 1.13). This reduction in boundary-layer energy may have inhibited convection nearer the centre. Sometimes the band may draw air from both sides. An important difference between a convective ring and a spiral band is that the swirling wind feeds the updraft in a band from the concave side, whereas the radial flow feeds the updraft in a convective ring primarily from the convex side.

Some bands appear to move outward, while others maintain a fixed location relative to the translating tropical cyclone centre. Moving bands, and other convective features, are frequently associated with cycloidal motion of the tropical cyclone centre, and intense asymmetric outbursts of convection (supercells) are observed to displace the tropical cyclone centre by tens of kilometres.

1.2 Formation regions

Tropical cyclones form in many parts of the world from initial convective disturbances sometimes referred to as cloud clusters. As the clusters evolve from a loosely organized state into mature, intense storms, they pass through several characteristic stages, but a uniform terminology does not exist to describe these stages over the different regions of the globe. Indeed there has been much debate in the literature about the meaning of such terms as "tropical cyclogenesis", "tropical-cyclone formation," and "tropical-cyclone development" (see e.g. McBride 1995). There are differing opinions also as to when genesis has occurred and intensification has com-
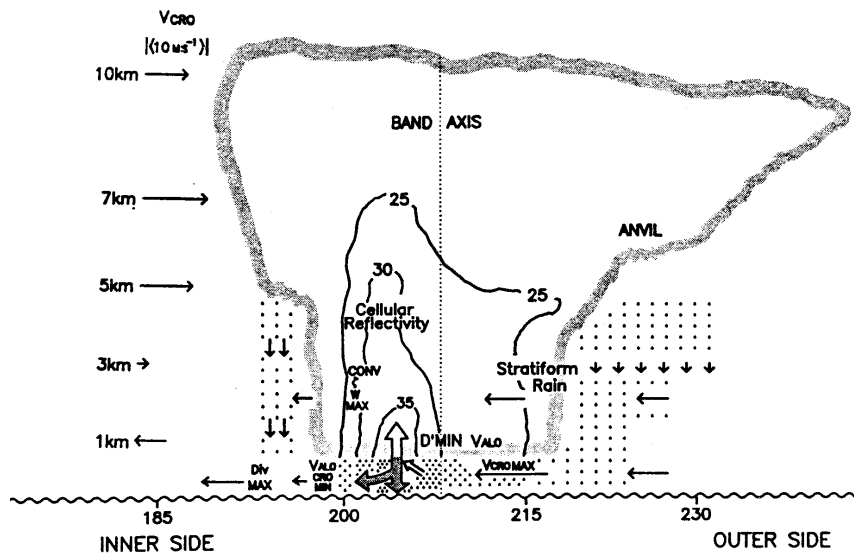
Figure 1.13: Thermodynamic structure of a rainband in Hurricane Earl 1986. The grey outline shows the cloud boundary, and the contours show radar reflectivity. Heavy horizontal and vertical arrows indicate the cross-band (V_{cro}) and convective vertical flows; lighter arrows indicate mesoscale subsidence. (From Powell 1990b)
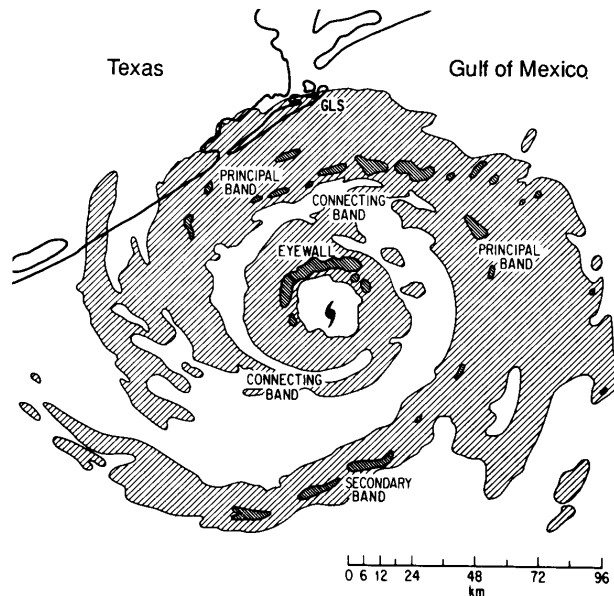
Figure 1.14: Radar echo pattern seen in Hurricane Alicia (1983) labelled according to the schematic to Fig. 1.14. Contours are for 25 and 40 dBZ. (From Marks and Houze 1987)

menced. McBride *op. cit.* remarks that the existence of a (warm) core region can be identified by the time that the system is classified as a tropical cyclone (i.e., mean wind speeds exceeding 17.5 m s^{-1} or 34 kt). Further development of the maximum wind speeds beyond 17.5 m s^{-1} will be referred to as *intensification.* This stage includes the evolution of the core into a well-defined radar eye.

Generally a larger scale (i.e., thousand kilometre) vortex already exists when the core develops and much of the research into tropical cyclone formation has examined the formation of the large-scale vortex in which the core forms. The distinction between core formation and large-scale vortex formation is important because different dynamical processes may be involved.

Here we follow McBride and refer to tropical cyclone *formation* as the transition from the cloud cluster state to the tropical cyclone stage with winds exceeding 17.5 m s^{-1}. Changes in wind speed of the outer vortex are referred to as outer structure change, or strength change, or size change.
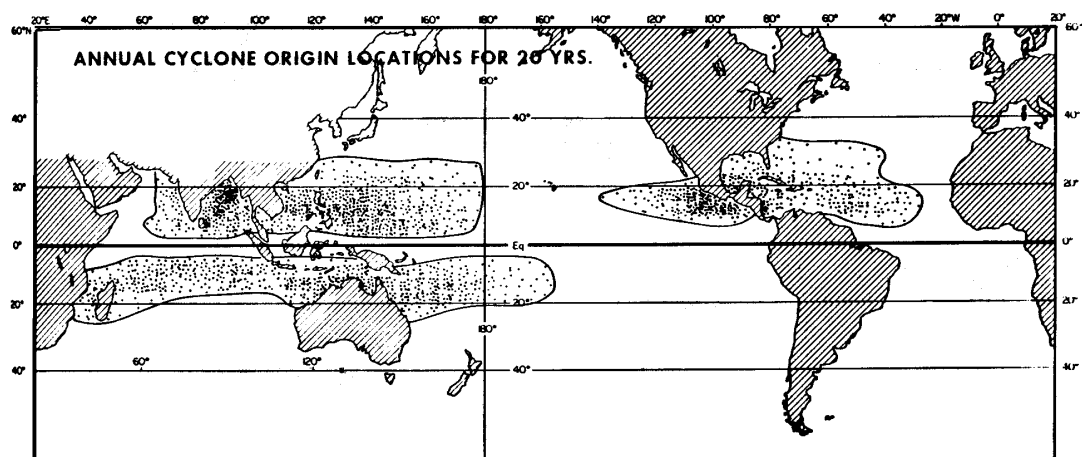
Figure 1.15: Locations of tropical cyclone formation over a 20-year period. (From Gray, 1975)

Each year approximately 80 tropical cyclones occur throughout the world, and about two thirds of these reach the severe tropical cyclone stage. Gray (1975) documented the initial detection points of each cyclone for a 20-year period fig. 1.15. Preferred regions of formation are over the tropical oceans and it is significant that these coincide broadly with regions of high sea surface temperatures (SSTs) (1.16). The warmest waters occur in the Western Pacific, the so-called "warm pool region", while the ocean temperatures in the Southeast Pacific is relatively cold. Indeed, climatological studies by Palmén (1948, 1957) and Gray (1995) have shown that tropical cyclogenesis occurs only in regions where the sea surface temperature is above 26.5°C and where the depth of the 26°C isotherm is 60 m or more. No formations occur within about 2.5^o lat. of the equator. Most of the formations (87%) occur between 20°N and 20°S (Fig. 1.17). Another interesting statistic is the frequency of tropical

cyclones per 100 years within any point as shown in Fig. 1.18.

ANNUAL MEAN
GLOBAL SEA SURFACE TEMPERATURES
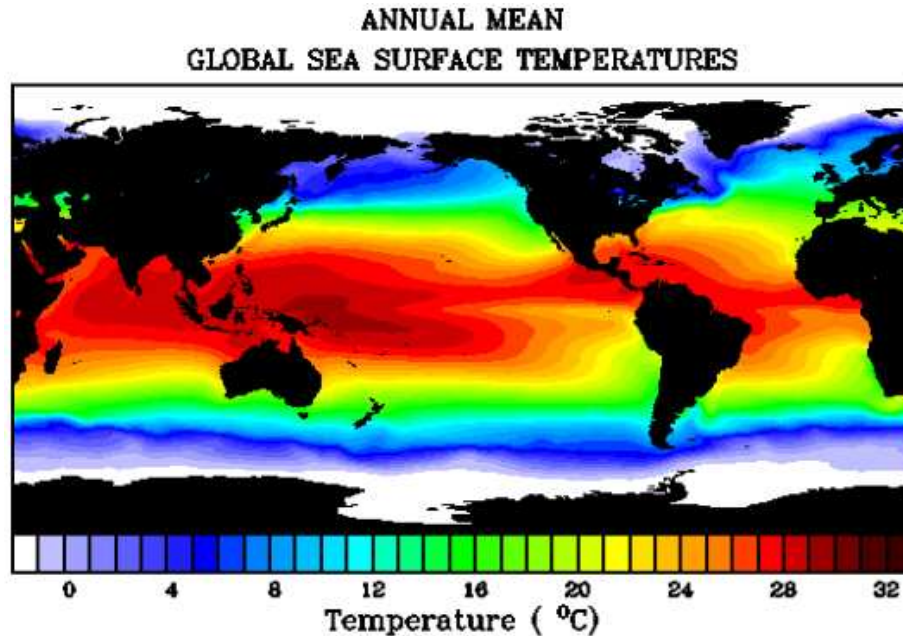
Temperature (°C)

Figure 1.16: Annual mean sea-surface temperature (° C). (From ???)

About two thirds of all cyclones occur in the Northern Hemisphere, and twice as many tropical cyclones occur in the Eastern as in the Western Hemisphere. These differences are due in part to the absence of tropical cyclones in the South Atlantic and the eastern South Pacific. Tropical cyclones are seasonal phenomena, and most basins have a maximum frequency of formation during the late summer to early fall period. The Southern Hemisphere peak occurs in January to March and the Northern Hemisphere peak is from July to September. The most active region is the Northwest Pacific Ocean, where typhoons occur in all seasons.

The seasonal distribution of formation locations is governed by two major factors. One is the association between tropical cyclone formation and SST, with the highest values of SST occurring during the late summer. Notice that regions of warm water also extend farther from the equator in the Northern Hemisphere in association with the Gulf Stream and the Kuroshio currents. However, SST is only one factor, as is evidenced by the absence of cyclones in the South Atlantic despite similar values of SST at certain times of the year.

The second factor in the seasonal distributions is related to the seasonal variations in the location of the monsoon trough. As discussed by Gray (1968), the Inter-Tropical Convergence Zone (ITCZ), which extends semi-continuously around the globe, may occur as a convergence line between trade easterlies from the Northern and Southern Hemispheres, or as a convergence zone in westerly monsoon flow. In this latter configuration, the monsoon westerlies usually have trade easterlies on
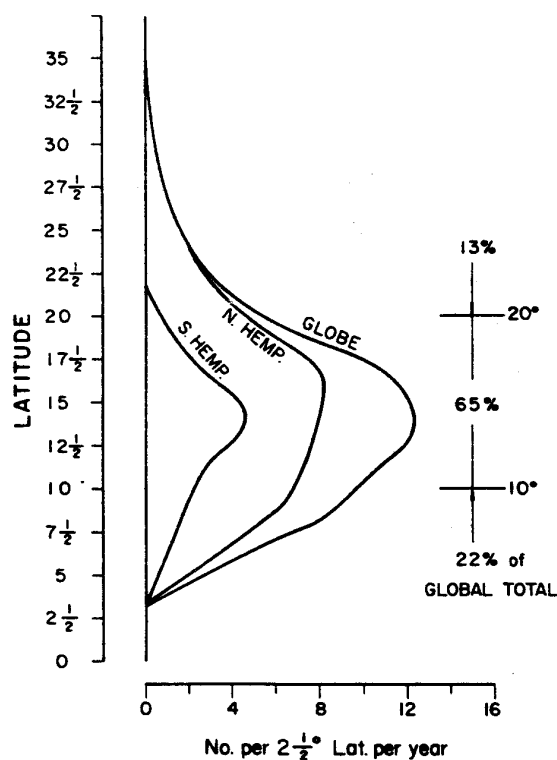
Figure 1.17: Latitudes at which initial disturbances that later became tropical cyclones were first detected. (From Gray 1975)

their poleward side. The shear line separating the monsoon westerlies from easterlies is known as the monsoon trough or monsoon shear line and is a climatologically preferred region for tropical cyclone formation. Typical upper- and lower-level flow patterns for the two modes of the ITCZ are illustrated schematically in Fig. 1.19. The trade convergence line of the ITCZ typically has large vertical wind shear. When monsoon westerlies are present, the low-level monsoon shear line is overlain (in the mean seasonal pattern) by the upper-level subtropical ridge. In western North Pacific, the ridge above the monsoon trough during the summer is called the subequatorial ridge. This configuration of trade easterlies overlain with westerlies and monsoon westerlies overlain with easterlies gives a (seasonal-mean) vertical wind shear close to zero, with westerly shear on the poleward side and easterly shear on the equatorward side (bottom panel. Fig. 1.19).

The only region of cyclone formation not associated with a monsoon trough is the North Atlantic. Possible explanations for this anomaly are discussed below.

In the first global climatology of tropical cyclogenesis, Gray (1968, 1975, 1979) found that cyclone formation is related to six environmental factors:

(i) large values of low-level relative vorticity;
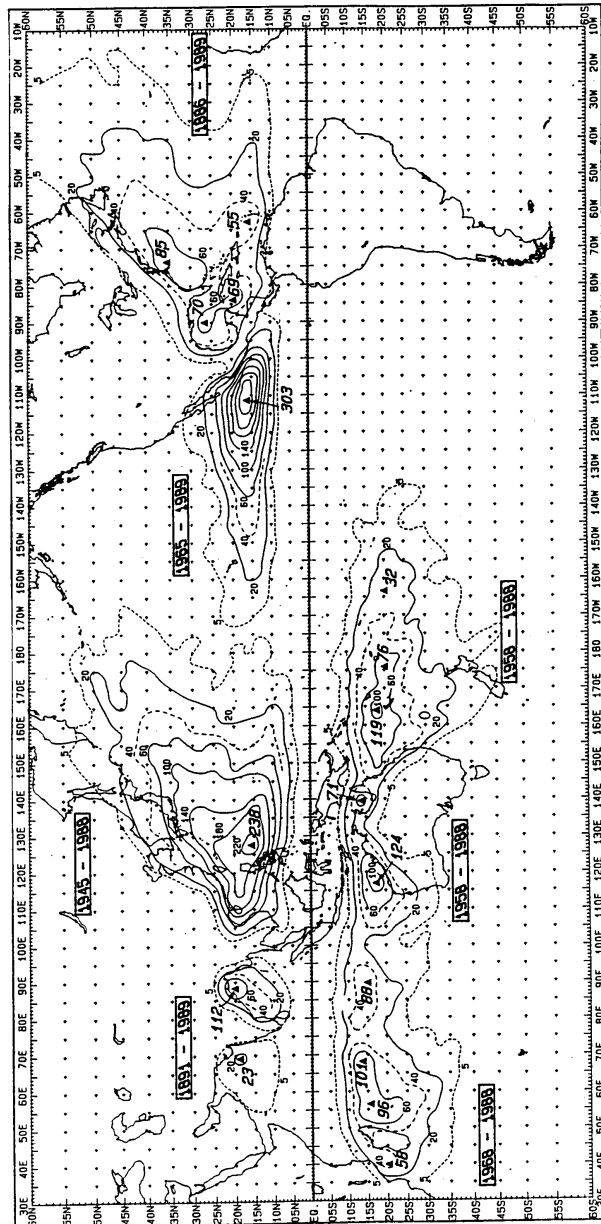
Figure 1.18: Frequency of tropical cyclones per 100 years within 140 km of any point. Solid triangles indicate maxima, with values shown. Period of record used is shown in boxes for each basin. (From WMO, 1993)

(ii) a location at least a few degrees poleward of the equator, giving a significant value of planetary vorticity;

(iii) weak vertical shear of the horizontal winds; iv) sea-surface temperatures (SSTs) exceeding 26°C, and a deep thermocline;
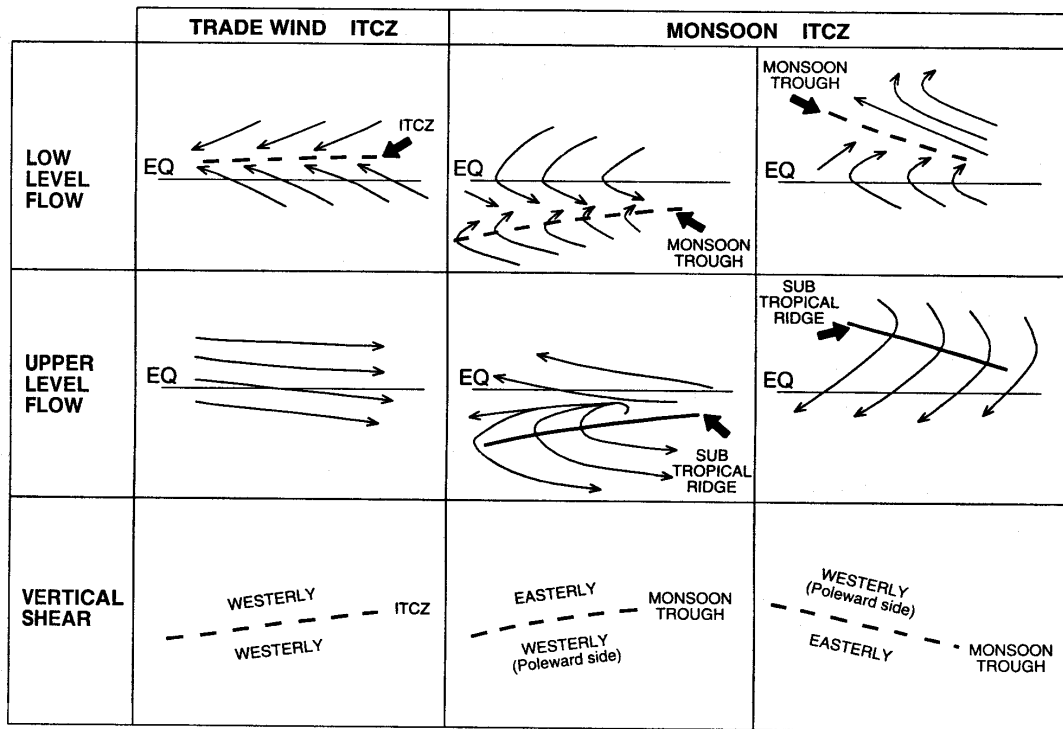
Figure 1.19: Schematics of trade-wind (left) and monsoon-type (two right columns) ITCZ flow regimes. The monsoon regimes are subdivided into those typical of the Australian/Southeast Indian Ocean ITCZ during January (middle) and the western North Pacific basin during August (right). Vertical wind shear between the low-level and upper-level flow is indicated in the lower panels.

  (v) conditional instability through a deep atmospheric layer; and

  (vi) large values of relative humidity in the lower and middle troposphere.

     The first three factors are functions of the horizontal dynamics, while the last three are thermodynamic parameters. Gray defined the product of (i), (ii), and (iii) to be the dynamic potential for cyclone development, while the product of (iv), (v), and (vi) may be considered the thermodynamic potential. The diagnosed tropical cyclone formation frequency derived by Gray (1975) using the above parameters is quite similar to the observed formation locations in (Fig. 1.15). However, the combination or the above six parameters were "tuned" to agree with the mean seasonal and geographical distributions of tropical cyclone development. As discussed by Gray (1975) and McBride (1981a), the thermodynamic parameters vary slowly in time and would be expected to remain above any threshold values necessary for tropical cyclone development throughout the cyclone season. On the other hand, the dynamic potential can change dramatically through synoptic activity. Thus, it

was hypothesized by Gray that cyclones form only during periods when the dynamic potential attains a magnitude above its regional climatological mean.

Frank (1987) noted that the above six environmental parameters are not independent. In the tropics, regions of high sea-surface temperatures are invariably correlated with conditional instability due to the weak horizontal temperature gradients in the lower troposphere. High humidities in the middle levels also tend to occur in convective clusters over warm waters, and virtually all areas with widespread deep convection are associated with mean ascending motion. Thus, Frank reduced the list to four parameters by combining (i) and (ii) into the absolute vorticity at low levels, deleting (v), and adding mean upward vertical motion to (vi). A number of observational studies have derived parameters relevant to the potential of an individual disturbance to develop into a cyclone.

1.2.1 Large-scale conditions for formation

The observational studies have isolated a number of synoptic-scale aspects that have an important role in the formation process:

(i) Tropical cyclones form from pre-existing disturbances containing abundant deep convection;

(ii) The pre-existing disturbance must acquire a warm core thermal structure throughout the troposphere;

(iii) Formation is preceded by an increase of lower tropospheric relative vorticity over a horizontal scale of approximately 1000 to 2000 km;

(iv) A necessary condition for cyclone formation is a large-scale environment with small vertical wind shear;

(v) An early indicator that cyclone formation has begun is the appearance of curved banding features of the deep convection in the incipient disturbance;

(vi) The inner core of the cyclone may originate as a mid-level meso-vortex that has formed in association with a pre-existing mesoscale area of altostratus (i.e., a Mesoscale Convective System or MCS); and

(vii) Formation often occurs in conjunction with an interaction between the incipient disturbance and an upper-tropospheric trough.

Evidence for these seven observations are discussed in detail by McBride (1995).

1.3 Tropical-cyclone tracks

Figure 1.20 shows the tracks of all tropical cyclones (maximum winds > 17 m s^{-1}) for the period 1979-1988 and Fig. 1.21 shows the mean direction of all hurricanes during the period indicated. Tropical cyclones form over the warm tropical oceans and typically move westwards and polewards, although tracks of individual storms can be quite erratic. To a first approximation tropical cyclones are steered by a mass-weighted average of the broadscale winds through the depth of the troposphere. It is common for storms that reach sufficiently high latitudes to recurve and move eastwards. Tropical cyclones rapidly lose their intensity when they move over land, but they often continue to produce copious amounts of rain. In many cases of landfalling storms, the majority of damage is caused by widespread flooding rather than by strong winds. Near the coast, however, much damage may be caused by high winds and by coastal storm surges. The dynamics of tropical-cyclone motion is discussed in Chapter 5.
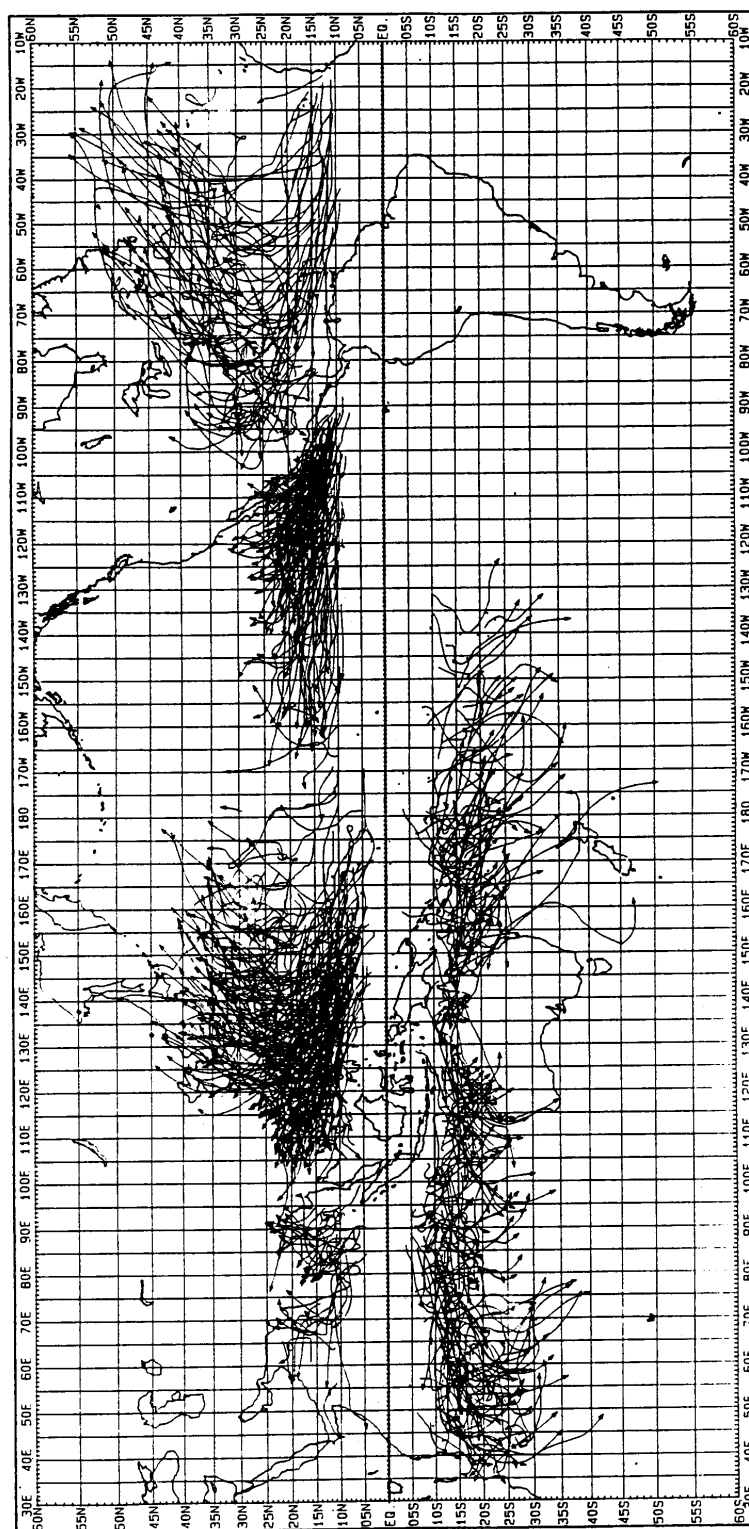
Figure 1.20: Tracks of all tropical cyclones (maximum winds > 17 ms^{-1}) for the period 1979-1988. (From WMO, 1993)
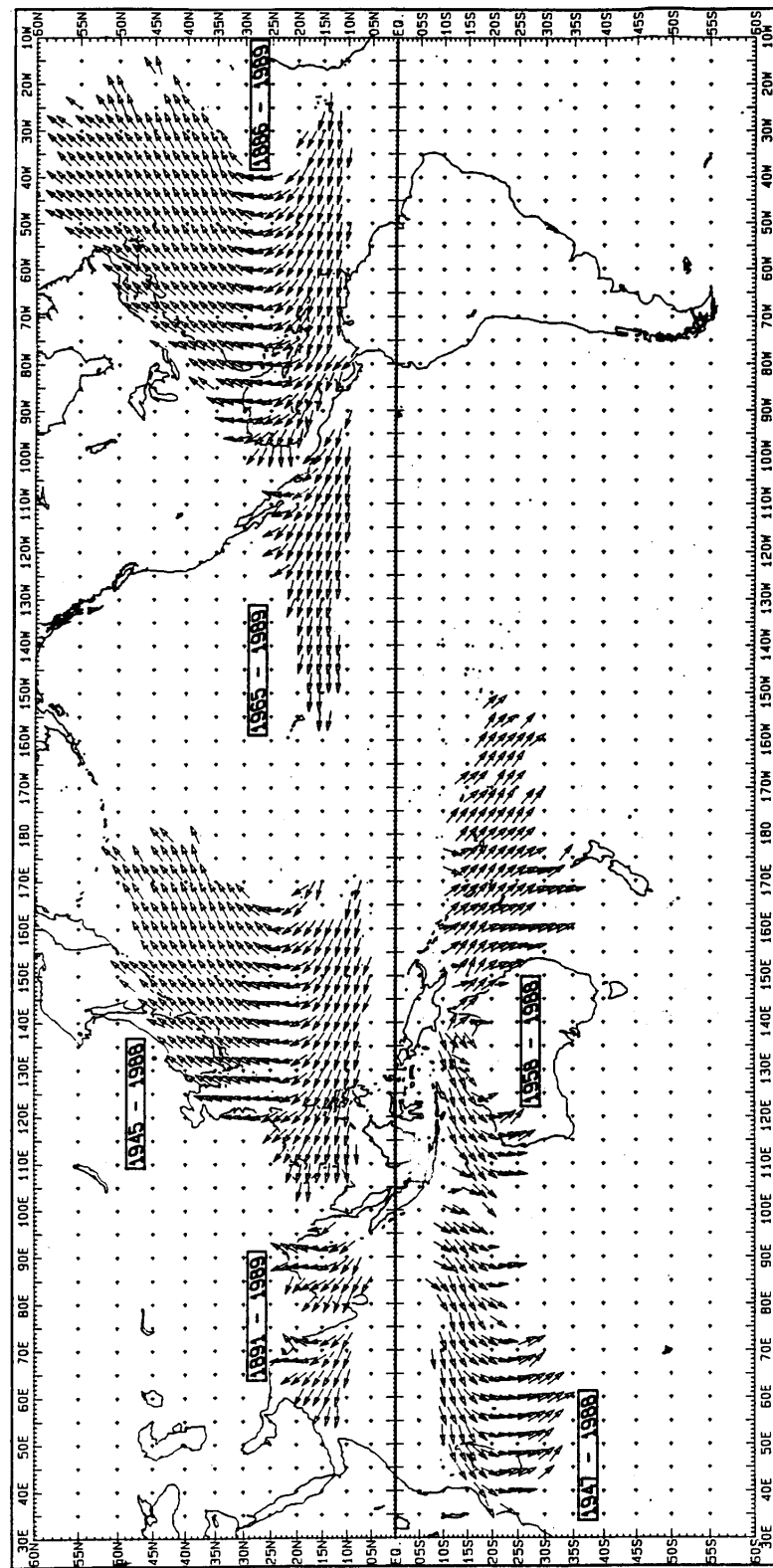
Figure 1.21: Mean direction of tropical cyclone motion over the periods indicated. (From WMO, 1993)

Chapter 2

DYNAMICS OF MATURE TROPICAL CYCLONES

2.1 The primary and secondary circulation

To a good first approximation the mature tropical cyclone consists of a horizontal quasi-symmetric circulation on which is superposed a thermally-direct vertical (transverse) circulation. These are sometimes referred to as the "primary circulation" and "secondary circulation", respectively, terms which were coined by Ooyama (1982). The former refers to the tangential flow rotating about the central axis, and the latter to the "in-up-and-out circulation" (low and middle level inflow, upper-level outflow). When these two components are combined, the picture emerges of air parcels spiralling inwards, upwards and outwards. The combined spiralling circulation is energetically direct because the rising branch of the secondary circulation near the centre is warmer than the subsiding branch, which occurs at large radial distances (radii > 500 km).

In this chapter we examine the dynamics of the spiralling circulation of tropical cyclones on the basis of the physical laws governing fluid motion and thermodynamic processes that occur. For simplicity we study the dynamics of a stationary axisymmetric hurricane-like vortex. In later chapters we consider the dynamics of tropical-cyclone motion and examine the asymmetric features of storms. We start by giving an overall picture of the dynamics and then go into detail about particular important aspects. First we introduce the governing equations and the important concept of buoyancy.

2.2 The equations of motion

To begin with we consider the full hydrostatic equations of motion, but with the density tendency in the continuity equation omitted. The primitive equations of motion comprising the horizontal momentum equation, the hydrostatic equation,

the continuity equation, the thermodynamic equation and the equation of states for frictionless motion in a rotating frame of reference on an f-plane may be expressed in cylindrical polar coordinates, (r, λ, z), as:

$$\frac{\partial u}{\partial t} + u\frac{\partial u}{\partial r} + \frac{v}{r}\frac{\partial u}{\partial \lambda} + w\frac{\partial u}{\partial z} - \frac{v^2}{r} - fv = -\frac{1}{\rho}\frac{\partial p}{\partial r}, \tag{2.1}$$

$$\frac{\partial v}{\partial t} + u\frac{\partial v}{\partial r} + \frac{v}{r}\frac{\partial v}{\partial \lambda} + w\frac{\partial v}{\partial z} + \frac{uv}{r} + fu = -\frac{1}{\rho r}\frac{\partial p}{\partial \lambda}, \tag{2.2}$$

$$\frac{\partial w}{\partial t} + u\frac{\partial w}{\partial r} + \frac{v}{r}\frac{\partial w}{\partial \lambda} + w\frac{\partial w}{\partial z} = -\frac{1}{\rho}\frac{\partial p}{\partial z} - g, \tag{2.3}$$

$$\frac{1}{r}\frac{\partial \rho r u}{\partial r} + \frac{1}{r}\frac{\partial \rho v}{\partial \lambda} + \frac{\partial \rho w}{\partial z} = 0, \tag{2.4}$$

$$\frac{\partial \theta}{\partial t} + u\frac{\partial \theta}{\partial r} + \frac{v}{r}\frac{\partial \theta}{\partial \lambda} + w\frac{\partial \theta}{\partial z} = \dot{\theta} \tag{2.5}$$

$$\rho = p_* \pi^{\frac{1}{\kappa}-1}/(R_d\theta) \tag{2.6}$$

where (u, v, w) is the velocity vector in component form, ρ is the air density, f is the Coriolis parameter, p is the pressure, θ is the potential temperature $\dot{\theta}$ is the diabatic heating rate, $\pi = (p/p_*)^\kappa$ is the Exner function, R_d is the specific gas constant for dry air, $\kappa = R_d/c_p$, c_p is the specific heat at constant pressure, and $p_* = 1000$ mb. The temperature is defined by $T = \pi\theta$. For tropical-cyclone scale motions it is a good approximation to make the hydrostatic approximation, whereupon Eq. (2.3) reduces to

$$\frac{\partial p}{\partial z} = -\rho g. \tag{2.7}$$

Multiplication of Eq. (2.2) by r and a little manipulation leads to the equation

$$\frac{\partial M}{\partial t} + u\frac{\partial M}{\partial r} + \frac{v}{r}\frac{\partial M}{\partial \lambda} + w\frac{\partial M}{\partial z} = -\frac{r}{\rho}\frac{\partial p}{\partial \lambda}, \tag{2.8}$$

where

$$M = rv + \frac{1}{2}fr^2, \tag{2.9}$$

is the absolute angular momentum per unit mass of an air parcel about the rotation axis. If the flow is axisymmetric (and frictionless), the right-hand-side of (2.8) is zero and the absolute angular momentum is conserved.

Exercise 2.1 Assuming the most general form of the mass conservation equation:

$$\frac{\partial \rho}{\partial t} + \frac{1}{r}\frac{\partial(\rho r u)}{\partial r} + \frac{1}{r}\frac{\partial(\rho v)}{\partial \lambda} + \frac{\partial(\rho w)}{\partial z} = 0,$$

show that the absolute angular momentum per unit volume,

$$M_v = \rho \left(rv + \frac{1}{2} fr^2 \right),$$

satisfies the equation:

$$\frac{\partial M_v}{\partial t} + \frac{1}{r} \frac{\partial (ruM_v)}{\partial r} + \frac{1}{r} \frac{\partial (vM_v)}{\partial \lambda} + \frac{\partial (wM_v)}{\partial z} = -r \frac{\partial p}{\partial \lambda}.$$

2.3 The primary circulation

Important aspects of the basic structure of a mature tropical cyclone can be deduced from two simple equations that express an exact balance of forces in the vertical and radial directions. These equations enable one to develop a simple theory for the primary circulation.
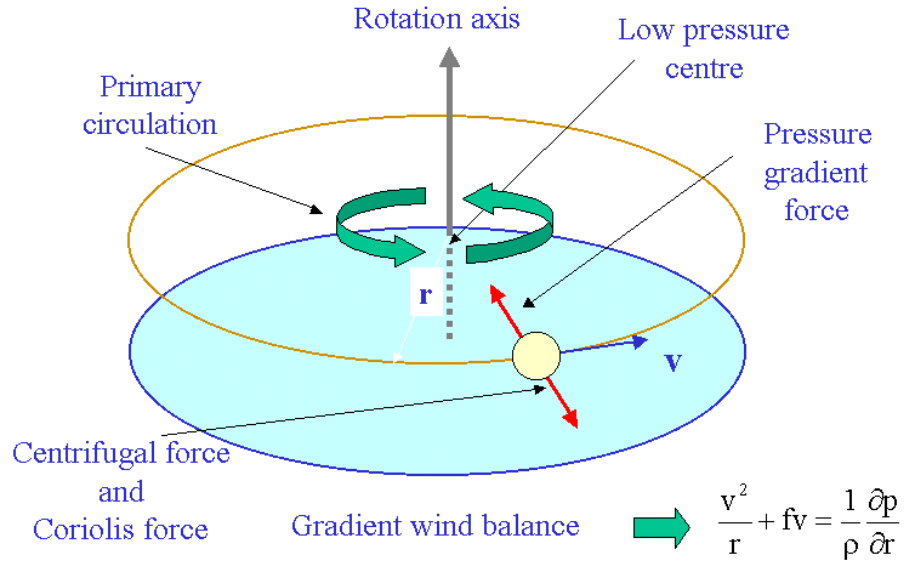
Figure 2.1: Schematic diagram illustrating the gradient wind force balance in the primary circulation of a tropical cyclone.

Let us assume that the flow is steady ($\partial/\partial t \equiv 0$) and let us ignore the secondary circulation, i.e. we assume that the radial velocity is identically zero (see Fig. 2.1). Then Eq. (2.1) reduces to the *gradient wind equation*:

$$\frac{v^2}{r} + fv = \frac{1}{\rho} \frac{\partial p}{\partial r}. \tag{2.10}$$

The force balance expressed by this equation is called *gradient wind balance*. Willoughby (1990) has shown that, in the free atmosphere, the azimuthal-mean tangential circulation of tropical cyclones is in gradient balance to a good approximation.

Taking $(\partial/\partial z)[\rho \times$ Eq. (2.10)$]$ and $(\partial/\partial r)[$Eq. (2.7)$]$ and eliminating the pressure we obtain the *thermal wind equation*

$$g\frac{\partial \ln \rho}{\partial r} + C\frac{\partial \ln \rho}{\partial z} = -\frac{\partial C}{\partial z}. \tag{2.11}$$

where we have defined

$$C = \frac{v^2}{r} + fv \tag{2.12}$$

to represent the sum of the centrifugal and Coriolis forces per unit mass. Equation (2.11) is a linear first-order partial differential equation for $\ln \rho$. The characteristics of the equation satisfy

$$\frac{dz}{dr} = \frac{C}{g}. \tag{2.13}$$

The characteristics are just the isobaric surfaces, because a small displacement (dr, dz) along an isobaric surface satisfies $(\partial p/\partial r)dr + (\partial p/\partial z)dz = 0$. Then, using the equations for hydrostatic balance $(\partial p/\partial z = -g\rho)$ and gradient wind balance $(\partial p/\partial r = C\rho)$ gives the equation for the characteristics. Alternatively, note that the pressure gradient per unit mass, $(1/\rho)(\partial p/\partial r, 0, \partial p/\partial z)$ equals $(C, 0, -g)$, which defines the "generalized gravity", $\mathbf{g_e}$; see Fig. 2.4. The density variation along a characteristic is governed by the equation

$$\frac{d}{dr}\ln \rho = -\frac{1}{g}\frac{\partial C}{\partial z}. \tag{2.14}$$

Given the vertical density profile, $\rho_a(z)$, Eqs. (2.13) and (2.14) can be integrated inwards along the isobars to obtain the balanced axisymmetric density and pressure distributions. In particular, Eq. (2.13) gives the height of the pressure surface that has the value $p_a(z)$, say, at radius R.

Since $\partial C/\partial z = (2v/r + f)(\partial v/\partial z)$, it follows from (2.14) that for a barotropic vortex $(\partial v/\partial z = 0)$, ρ is constant along an isobaric surface, i.e. $\rho = \rho(p)$, whereupon T_v is a constant also.

The thermal wind equation (2.11), or equivalently Eq. (2.14), shows that in a cyclonic vortex in the northern hemisphere $(v > 0)$ with tangential wind speed that decays with height $(\partial v/\partial z < 0)$, $\log \rho$ and hence ρ decrease with decreasing radius along the isobaric surface. Thus the virtual temperature $T_v(r, z)$ and θ increase and the vortex is warm cored (i.e. $\partial T_v/\partial r < 0$). This prediction of the thermal wind equation *is consistent with* the observation that tropical cyclones are warm-cored systems, and that the tangential wind speed decreases with altitude. If the tangential wind speed were to increase with height $(\partial v/\partial z > 0)$ the vortex would be cold cored. Note that the characteristics dip down as the axis is approached on account of Eq. (2.13). The reason for the warm core structure of tropical cyclones is discussed in section 2.5.

The analysis above shows that any steady vortical flow with velocity field $\mathbf{u} = (0, v(r, z), 0)$ is a solution of the basic equation set (2.1) - (2.6), when the density field

satisfies (2.11). Willoughby's observational evidence that the primary circulation of a hurricane is approximately in gradient wind balance makes the foregoing analysis a good start in understanding the structure of this circulation. However the solution neglects the secondary circulation associated with nonzero u and w and it neglects the effects of friction near the sea surface. These are topics of subsequent subsections.

Exercise 2.2 Show that in terms of the Exner function, Eqs. (2.10) and (2.7) may be written as

$$\chi C = c_p \frac{\partial \pi}{\partial r} \quad \text{and} \quad -\chi g = c_p \frac{\partial \pi}{\partial z}, \tag{2.15}$$

respectively.

Exercise 2.3 Show that Eq. (2.11) may be reformulated as

$$g \frac{\partial (\ln \chi)}{\partial r} + C \frac{\partial (\ln \chi)}{\partial z} = -\frac{\partial C}{\partial z}. \tag{2.16}$$

where $\chi = 1/\theta$.

It is instructive to compare the magnitude of the centrifugal and Coriolis terms in Eq. (2.1), their ratio being

$$Ro(r) = \frac{v}{fr}. \tag{2.17}$$

This equation defines a local Rossby number for the flow. Let r_m be radius of maximum tangential wind speed of a tropical cyclone and v_m the tangential wind speed at this radius. Then Ro is typically on the order of $40 \div (40 \times 10^3 \times 5 \times 10^{-5}) = 20$, typical values for r_m and v_m being 40 km and 40 m s^{-1}, respectively. It follows that the inner core region of a tropical cyclone is approximately in *cyclostrophic balance*, i.e. the Coriolis forces are small compared with the centrifugal forces. However, at a radius of 200 km, where the wind speeds may be on the order of 10 m s^{-1}, $Ro \approx 1$ and these two forces are comparable. As the radius increases further, the circulation becomes more and more *geostrophic*, i.e. Ro becomes small compared with unity and the Coriolis forces become dominant.

2.4 The tropical-cyclone boundary layer

It turns out that the effects of surface friction in a tropical cyclone have a dramatic influence not only on the flow in the layer in which friction acts, the so-called boundary layer, but also on the flow above this layer. The boundary layer is typically about

500 m deep. One obvious effect of friction is to reduce the tangential wind speed near the surface, and therefore the centrifugal and Coriolis forces. However, a scale analysis shows that it has little effect on the pressure field so that the radial pressure gradient in the boundary layer is approximately the same as that immediately above the layer (see e.g. Smith 1968). Thus there is a *net* inward force on air parcels in the boundary layer, which drives inflow in the layer (Fig. 2.2). Far from the rotation axis, both the inflow velocity and the radial mass flux increase with decreasing radius and this leads to *forced* subsidence above the boundary layer. At inner radii, where the inflow and mass flux begin to decline, air is discharged from the boundary layer into the vortex above. In other words, the presence of the boundary layer *forces* vertical motion in the main part of the vortex above the boundary layer. In the tropical cyclone, the air in the boundary layer is moistened as it spirals inwards over the warm ocean. This moistening elevates the pseudo-equivalent potential temperature of the boundary-layer air, θ_{eb}, so that $\partial \theta_{eb}/\partial r < 0$. We consider now the fate of this moist air and return in Chapter 3 to examine in detail the dynamics and thermodynamics of the boundary layer. There we show that given the tangential wind speed distribution for a steady axisymmetric vortex, one can determine the radial distribution of the vertically-averaged wind speed components in the boundary layer as functions of radius as well as the induced vertical velocity at the top of the boundary layer. Given also the vertically-averaged temperature and specific humidity at some large radius and the sea surface temperature beneath the vortex, one can determine the radial variation of the vertically-averaged θ_{eb} in the boundary layer.
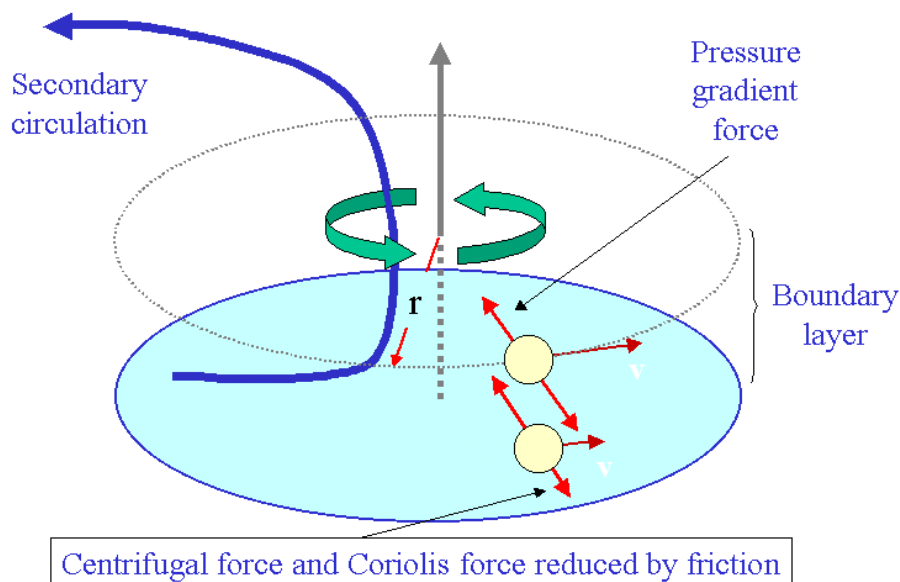
Figure 2.2: Schematic diagram illustrating the disruption of gradient wind balance by friction in the boundary layer leaving a net inward pressure gradient that drives the secondary circulation with inflow in the boundary layer and outflow above it.

2.5   Moist convection and the sloping eyewall

When the inward-spiralling moisture-laden air is forced upwards out of the boundary layer in the inner core region, it expands and cools. Condensation rapidly ensues and as the air continues to rise in the eyewall clouds, latent heat is released and a significant fraction of the condensed water falls out of the clouds as precipitation. The latent heat release is responsible for the warm core in the cyclone, but only a small fraction of the heat released is manifest as an elevated temperature perturbation at a particular height; most of it is offset by the adiabatic cooling that occurs as air parcels rise and expand. We may think of the effect of the heat release on the temperature field as follows. To a first approximation, ascending air parcels conserve their θ_e as indicated in Fig. 2.3. Since the air in the eyewall clouds is saturated, the virtual temperature of an air parcel at a particular pressure level is a monotonically-increasing function of its θ_e, which, in turn, is equal to the θ_e it had when it left the boundary layer. Therefore, at least in the eyewall cloud region the radial gradient of $T_v(z)$ is determined by the radial gradient of θ_e at the top of the boundary layer, which as noted above is negative. In other words, at any level in the cloudy region, $(\partial T_v / \partial r)_p < 0$, which explains why the tropical cyclone has a warm core, at least outside the eye. The reason that the eye is warm also is examined in section 2.7. The discussion section 2.4 indicates that the boundary layer in a mature hurricane controls not only the rate at which air ascends at a particular radius, but determines also the radial gradient of virtual temperature (and hence density) above the boundary layer, at least in regions of ascent.

From mass continuity, the air that converges in the boundary layer must flow outwards above the boundary layer, a fact that accounts for the outward slope of the eyewall and of air parcel trajectories. Ascending air parcels approximately conserve their absolute angular momentum, M, as well as their θ_e so that (absolute) angular momentum surfaces and the moist isentropes are approximately coincident (at least where there is cloud) and these surfaces slope outwards with height as indicated schematically in Fig. 2.3.

We emphasize that in the foregoing picture of the warm-core structure of a tropical cyclone, the latent heat release in clouds serves merely to maintain the conservation of pseudo-moist entropy characterized by θ_e along air-parcel trajectories. The warm-core itself is seen as a result of the increase in θ_e with decreasing radius as determined by the thermodynamic processes in the boundary layer, which are examined in detail in Chapter 3. This picture was first proposed by Emanuel (1986) and forms the basis for his steady model for the tropical cyclone described in Chapter 4.

Many early papers consider the role of latent heat release as providing local buoyancy in the eye-wall clouds and suggest that it is this buoyancy that "drives" the secondary circulation. We shall see that this explanation is raises many questions. For example the temperature in the eyewall clouds is typically less than in the eye. Moreover, we have seen that much of the temperature field of the tropical cyclone resides in thermal wind balance. To examine these questions in more detail we need
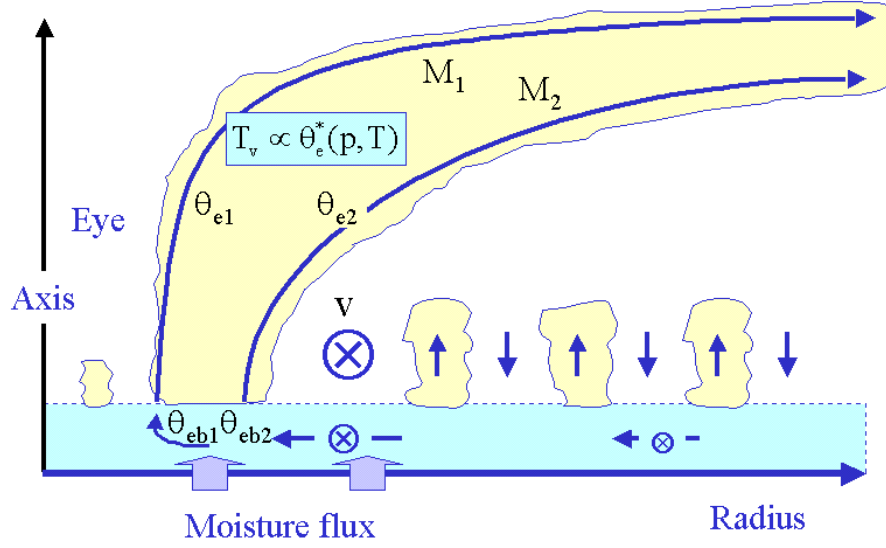
Figure 2.3: Schematic diagram of the secondary circulation of a mature tropical cyclone showing the eye and the eyewall clouds. Air spirals inwards in a shallow boundary layer near the sea surface, picking up moisture as it does so. The absolute angular momentum, M, and equivalent potential temperature, θ_e of an air parcel is conserved after the parcel leaves the boundary layer and ascends in the eyewall clouds. The precise values of these quantities depend on the radius at which the parcel exits the boundary layer. At radii beyond the eyewall cloud, shallow convection plays an important role in moistening and cooling the lower troposphere above the boundary layer and warming and drying the boundary layer as indicated.

to review the concept of air-parcel buoyancy, especially in the context of rapidly-rotating vortices. This is the subject of the next section.

2.6   Buoyancy and generalized buoyancy

The buoyancy of an air parcel in a density-stratified air layer is defined as the difference between the weight of air displaced by the parcel (the upward thrust according to Archimedes principle) and the weight of the parcel itself. This quantity is normally expressed per unit mass of the air parcel under consideration, i.e.

$$b = -g\frac{(\rho - \rho_a)}{\rho},$$ (2.18)

where ρ is the density of the parcel, $\rho_a = \rho_a(z)$ is the density of the environment at the same height z as the parcel, and g is the acceleration due to gravity. Here and elsewhere the vertical coordinate z is defined to increase in the direction opposite to gravity. The calculation of the upward thrust assumes that the pressure within the

air parcel is the same as that of its environment *at the same level*, an assumption that is invalid a rapidly-rotating vortex. In the latter case one can define a generalized buoyancy force, which acts normal to the isobaric surface intersecting the air parcel and which is proportional to the density difference between the parcel and its environment along that surface (see below).

A similar expression for the buoyancy force given in (2.18) may be obtained by starting from the vertical momentum equation and replacing the pressure p by the sum of a reference pressure p_{ref} and a perturbation pressure, p'. The former is taken to be in hydrostatic balance with a prescribed reference density ρ_{ref}, which is often taken, for example, as the density profile in the environment. In real situations, the environmental density is not uniquely defined, but could be taken as the horizontally-averaged density over some large domain surrounding the air parcel. Neglecting frictional forces, the vertical acceleration per unit mass can be written alternatively as

$$\frac{Dw}{Dt} = -\frac{1}{\rho}\frac{\partial p}{\partial z} - g \ \text{ or, } \ \frac{Dw}{Dt} = -\frac{1}{\rho}\frac{\partial p'}{\partial z} + b \qquad (2.19)$$

where w is the vertical velocity, D/Dt is the material derivative, and t is the time presents a similar derivation, but makes the anelastic approximation (Ogura and Phillips, 1962), in which the density in the denominator of (2.18) is approximated by that in the environment. Clearly, the sum of the vertical pressure gradient and gravitational force per unit mass acting on an air parcel is equal to the sum of the vertical gradient of perturbation pressure and the buoyancy force, where the latter is calculated from Eq. (2.18) *by comparing densities at constant height*. The expression for b in (2.19) has the same form as that in (2.18), but with ρ_{ref} in place of ρ_a. However, the derivation circumvents the need to assume that the local (parcel) pressure equals the environmental pressure when calculating b, which, as noted above, is not valid for a rapidly-rotating vortex. The foregoing decomposition indicates that, in general, the buoyancy force is not uniquely defined because it depends on the (arbitrary) choice of a reference density. However, the sum of the buoyancy force and the perturbation pressure gradient per unit mass *is* unique. If the motion is hydrostatic, the perturbation pressure gradient and the buoyancy force are equal and opposite, but they remain non-unique.

Using the gas law ($p = \rho R_d T$ and the usual definition of virtual potential temperature, the buoyancy force per unit mass can be written as

$$b = g\left[\frac{(\theta - \theta_{ref})}{\theta_{ref}} - (\kappa - 1)\frac{p'}{p_{ref}}\right], \qquad (2.20)$$

where θ is the virtual potential temperature of the air parcel in K and θ_{ref} is the corresponding reference value. The second term on the right-hand-side of (2.20) is sometimes referred to as the "dynamic buoyancy", but in some sense this is a misnomer since buoyancy depends fundamentally on the density perturbation and this term simply corrects the calculation of the density perturbation based on the virtual potential temperature perturbation. If the perturbation pressure gradient

terms in (2.19) are written in terms of the Exner function and/or its perturbation, the second term in (2.20) does not appear in the expression for buoyancy.

The expression (2.20) is valid also in a rapidly rotating vortex, but as shown in section 2.5, there exists then a radial component of buoyancy as well. When clouds are involved it may be advantageous to include the drag of hydrometeors in the definition of buoyancy, but we omit this additional effect here.
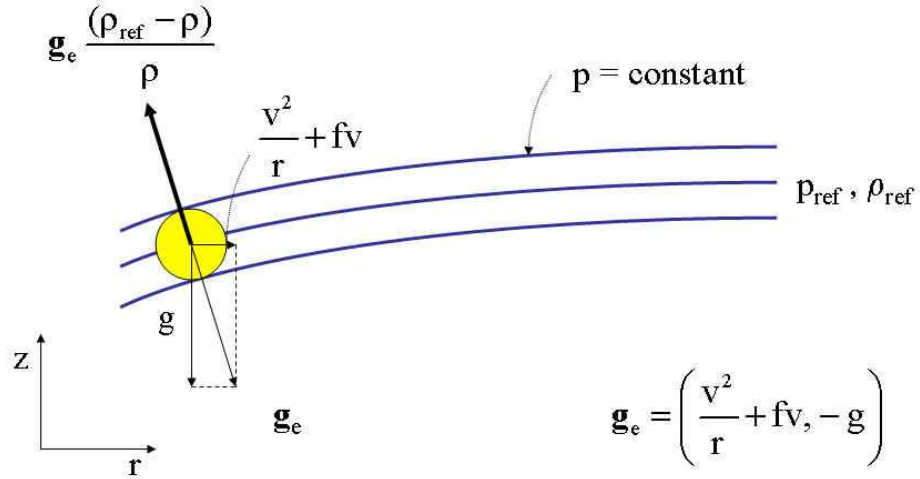
Figure 2.4: Schematic radial-height cross-section of isobaric surfaces in a rapidly-rotating vortex showing the forces on an air parcel including the gravitational force g, per unit mass, and the sum of the centrifugal and Coriolis forces $C = v^2/r + fv$ per unit mass. Note that the isobaric surfaces are normal to the local "generalized gravitational force" $\mathbf{g_e} = (C, 0, -g)$. The Archimedes force $-\mathbf{g_e}\rho_{ref}$ slopes upwards and inwards while the weight $\mathbf{g_e}\rho$ slopes downwards and outwards. Thus the net buoyancy force acting on the parcel per unit mass is $|\mathbf{g_e}|(\rho_{ref} - \rho)/\rho$ in the direction shown.

In a rapidly-rotating, axisymmetric vortex, an air parcel experiences not only the gravitational force, but also the radial force $C = v^2/r + fv$, where v is the tangential wind component at radius r. If the vortex is in hydrostatic and gradient wind balance, the isobaric surfaces slope in the vertical and are normal to the effective gravity, $\mathbf{g_e} = (C, 0, -g)$, expressed in cylindrical coordinates (r, λ, z) (see Fig. 2.4). The Archimedes force acting on the parcel is then $-\mathbf{g_e}\rho_{ref}$ and the effective weight of the parcel is $\mathbf{g_e}\rho$, where ρ_{ref} is now the far-field (reference-) density *along the same isobaric surface as the parcel*. Accordingly, we may define a *generalized buoyancy force per unit mass*:

$$\mathbf{b} = \mathbf{g_e}\frac{\rho - \rho_{\mathbf{ref}}}{\rho}, \tag{2.21}$$

analogous to the derivation of (2.18). Note that unless $v(v + rf) < 0^1$, fluid parcels

---

[1]**I need to refer to a section on vortex stability, still to be written.**

that are lighter than their environment have an inward-directed component of generalized buoyancy force as well as an upward component, while heavier parcels have an outward component as well as a downward component. This result provides the theoretical background for a *centrifuge.*

2.7 The tropical cyclone eye

Observations show that the eye is a cloud free region surrounding the storm axis where the air temperatures are warmest. Therefore, it would be reasonable to surmise that the air within it has undergone descent during the formative stages of the cyclone, and that possibly it continues to descend. The question then is: why doesn't the inflowing air spiral in as far as the axis of rotation. We address this question later, but note here that eye formation is consistent with other observed features of the tropical cyclone circulation. The following discussion is based on that of Smith (1980). Assuming that the primary circulation is in gradient wind balance, we may integrate Eq. (2.10) with radius to obtain a relationship between the pressure perturbation at a given height z on the axis to the tangential wind field distribution, i.e:

$$p(0, z) = p_a(z) - \int_0^\infty \rho \left(\frac{v^2}{r} + fv \right) dr, \qquad (2.22)$$

where $p_a(z) = p(\infty, z)$ is the environmental pressure at the same height. Differentiating Eq. (2.22) with respect to height and dividing by the density gives the perturbation pressure gradient per unit mass along the vortex axis:

$$-\frac{1}{\rho}\frac{\partial(p - p_a)}{\partial z} = -\frac{1}{\rho}\frac{\partial}{\partial z}\int_0^\infty \rho \left(\frac{v^2}{r} + fv \right))dr. \qquad (2.23)$$

Observations in tropical cyclones show that the tangential wind speed decreases with height above the boundary layer and that the vortex broadens with height in the sense that the radius of the maximum tangential wind speed increases with altitude (see Fig. 1.11). This behaviour, which is consistent with outward-slanting absolute angular momentum surfaces as discussed above, implies that the integral on the right-hand-side of Eq. (2.23) decreases with height. Then Eq. (2.23) shows that there must be a downward-directed perturbation pressure gradient force per unit mass along the vortex axis. This perturbation pressure gradient tends to drive subsidence along and near to the axis to form the eye. However, as this air subsides, it is compressed and warms relative to air at the same level outside the eye and thereby becomes locally buoyant (i.e. relative to the air outside the eye). This upward buoyancy approximately balances the downward directed (perturbation) pressure gradient so that the actual subsidence results from a small residual force. In essence the flow remains close to hydrostatic balance.

As the vortex strengthens, the downward pressure gradient must increase and the residual force must be downwards to drive further subsidence. On the other hand, if

the vortex weakens, the residual force must be upwards, allowing the air to re-ascend. In the steady state, the residual force must be zero and there is no longer a need for up- or down motion in the eye, although, in reality there may be motion in the eye associated with turbulent mixing across the eyewall or with asymmetric instabilities within the eye.

It is not possible to measure the vertical velocity that occur in the eye, but one can make certain inferences about the origin of air parcels in the eye from their thermodynamic characteristics, which can be measured (see e.g. Willoughby, 1995).

2.8 Radiative cooling

The tropical atmosphere is stably stratified so that large vertical displacements of air parcels may only occur in the presence of diabatic processes: parcel ascent can occur over significant depths only if there is latent heat release to counter adiabatic cooling (i.e. if the ascent occurs in cloud); and parcel subsidence can occur over a substantial depth only if there is radiative cooling to counter adiabatic warming. Thus radiative effects in tropical cyclones cannot be ignored if we wish to understand the subsiding branch of the secondary circulation. The following discussion of radiative effects is based on that of Anthes (1979, p218-9).

Diabatic heating rates associated with the absorption of shortwave radiation energy and the emission of longwave radiation are quite small compared with the heating rates associated with condensation in deep precipitating clouds. In the cloud-free regions of the tropical atmosphere the mean radiative cooling rate is 1 to 2°C/day from the surface to 10 km ($\approx$ 250 mb) and decreases to about zero at the tropopause. In a region of multi-layer clouds, however, there is practically no radiative cooling in the clouds, but there is strong cooling at their top.

The result of differential radiative heating between the cloud-free environment and a cloudy tropical depression or tropical cyclone is to generate a direct circulation, with sinking motion in the clear air and rising motion in the cloudy air (Fig. 2.5). In the tropical cyclone, radiation acts to maintain the baroclinicity associated with the warm core. However, it is a smaller effect than differential heating by condensation, except possibly in lightly precipitating systems. This may be seen by relating the mean diabatic rate of temperature in a column of air of unit cross-section extending from 1000 mb to 100 mb to the rainfall rate R_f (cm/day):

$$\frac{\partial T}{\partial t} = -2.67 R_f \quad (^o\text{C/day}). \tag{2.24}$$

For typical cloud cluster rainfall rates of 2.5 cm/day (Ruprecht and Gray, 1976), the average tropospheric rate of temperature change would be 6.7 cm/day, which is about five times larger than the effect of radiation. For hurricanes, a typical rainfall rate in the inner 222 km region is 9.5 cm/day, which gives $\partial T/\partial t = -25°$C/day, more than an order of magnitude larger than the radiative cooling rate. Thus, without latent heat release, only a slow meridional circulation could be maintained
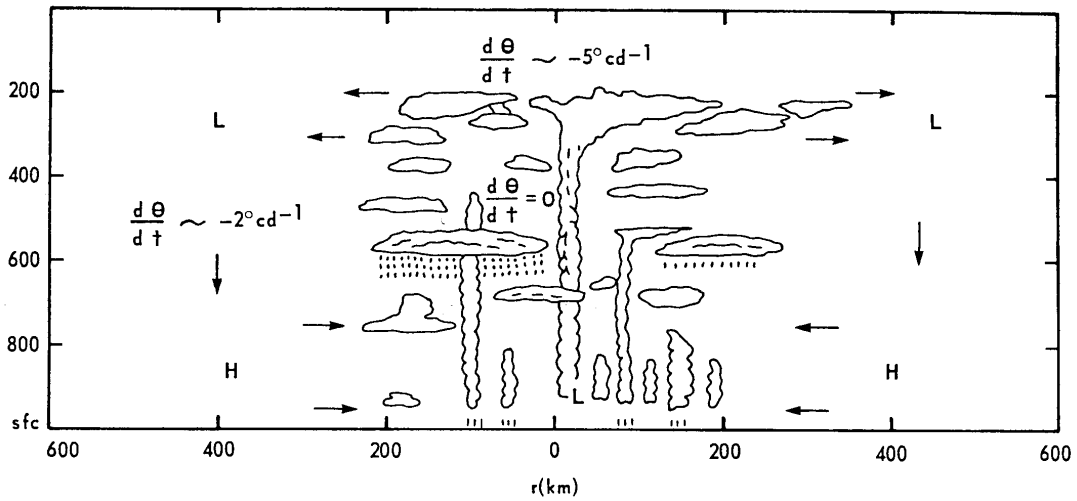
Figure 2.5: Schematic diagram of radiatively-induced circulation in a tropical disturbance. In clear air surrounding the cloudy centre, diabatic cooling is about 2°C/day. In the cloudy interior, radiative cooling is nearly zero. The differential cooling induces sinking motion in the environment, where pressures rise at the surface and fall aloft. Flow in low levels is toward the centre of the disturbance, aloft it is outward. (From Anthes, 1979)

by radiation because the lifting of statically-stable air leads to cooling and a negative buoyancy force that opposes the circulation induced by radiative cooling. With latent heating, however, the mean adiabatic cooling in the ascending branch of the secondary circulation is opposed and much larger upward velocities may be attained.

When direct absorption of shortwave solar radiation is considered, a diurnal variation of the radial differential cooling rate is introduced. The differential cooling during the day is reduced from a nocturnal value of 2°C/day to a value of about 1°C/day in the middle troposphere. For $\partial T/\partial p \approx 8°C/(100 \text{ mb})$, $\partial T/\partial t \approx 1°C/day$ corresponds to a vertical velocity ω of about 12.5 mb/day, which is supported by a mean divergence of 5×10^{-7} s^{-1} between the surface and 500 mb. This is much smaller than the observed diurnal variation in low-level divergence, which is about 5×10^{-6} s^{-1} (Gray and Jacobson, 1977). What probably happens is that the small diurnal variation in radiation-induced divergence triggers a much larger response by modulating deep cumulus convection. During the night, when differential cooling is at a maximum, upper-level divergence over the disturbance and low-level convergence into the disturbance results in a dramatic increase in convection. After sunrise, absorption of solar radiation in the cloud-free environment and increased subsidence from the enhanced secondary circulation during the night reduces the mean temperature difference between the disturbance and its environment. The mean circulation then diminishes and the deep cumulus clouds weaken.

2.9   Tropical cyclone intensity change

We have seen in section 2.3 that if there is no friction and no diabatic forcing ($\dot{\theta} = 0$), Eqs. (2.1) - (2.6) admit steady axisymmetric solutions of the form $(0, v(r, z), 0)$ in cylindrical coordinates. Axisymmetric vortices intensify as a result of radial inflow above the boundary layer on account of the conservation of angular momentum. We have seen in section 2.4 that the presence of surface friction induces radial inflow in the boundary layer and ascent or descent at the top of the boundary layer. If there is no diabatic forcing there must be radial outflow above the boundary layer otherwise friction alone would lead to intensification of the primary vortex. Because the air above the boundary layer is stably-stratified, the outflow tends to occur in a layer of limited depth above the boundary layer. It is clear that intensification requires a mechanism to produce inflow that is strong enough to oppose the outflow induced by surface friction. The only conceivable mechanism able to do this is diabatic heating arising from the latent heat release in deep clouds, which produces *buoyancy* in the clouds. We consider here a balanced axisymmetric theory for intensity change, i.e. one in which the flow remains close to hydrostatic and gradient wind balance. In a later chapter we consider idealized numerical modelling studies of tropical-cyclone intensification. As a preliminary step we examine the definition of buoyancy and its generalization for a rapidly-rotating fluid. Later we will examine other aspects of the buoyancy force.

2.10   The secondary circulation

If the vortex is axisymmetric and in approximate geostrophic and hydrostatic balance, we can derive an equation for the streamfunction, ψ, of the circulation in a vertical plane, the so-called secondary circulation. This streamfunction is such that

$$u = -\frac{1}{r\rho}\frac{\partial\psi}{\partial z} \qquad w = \frac{1}{r\rho}\frac{\partial\psi}{\partial r}.$$
(2.25)

which ensures that the continuity equation (2.4), is satisfied. The equation for ψ follows by differentiating the thermal wind equation in the form (2.16) with respect to time t and using the azimuthal momentum equation and thermodynamic equation to eliminate the time derivatives. It is convenient to write the last two equations in the form

$$\frac{\partial v}{\partial t} + u(\zeta + f) + wS = \dot{V}$$
(2.26)

and

$$\frac{\partial\chi}{\partial t} + u\frac{\partial\chi}{\partial r} + w\frac{\partial\chi}{\partial z} = -\chi^2\dot{\theta}$$
(2.27)

where $\zeta = (1/r)(\partial(rv)/\partial r)$ is the relative vorticity and we have added a momentum source term $\dot{V}$ in the former equation for reasons that will emerge later. The time

derivative of (2.11) is

$$g\frac{\partial}{\partial r}\frac{\partial \chi}{\partial t} + \frac{\partial}{\partial z}\left(C\frac{\partial \chi}{\partial t} + \chi\frac{\partial C}{\partial t}\right) = 0$$

and substitution of the time derivatives from (2.26) and (2.27) gives

$$g\frac{\partial}{\partial r}\left(u\frac{\partial \chi}{\partial r} + w\frac{\partial \chi}{\partial z} - Q\right) + \frac{\partial}{\partial z}\left[C\left(u\frac{\partial \chi}{\partial r} + w\frac{\partial \chi}{\partial z} - Q\right) + \chi\xi\left(u(\zeta + f) + wS - \dot{V}\right)\right] = 0$$

where $\chi = 1/\theta$ and $Q = -\chi^2\dot{\theta}$. Then

$$\frac{\partial}{\partial r}\left[g\frac{\partial \chi}{\partial z}w + g\frac{\partial \chi}{\partial r}u\right] +$$

$$\frac{\partial}{\partial z}\left[(\chi\xi(\zeta + f) + C\frac{\partial \chi}{\partial r})u + \frac{\partial}{\partial z}(\chi C)w\right] = g\frac{\partial Q}{\partial r} + \frac{\partial}{\partial z}(CQ) + \frac{\partial}{\partial z}(\chi\xi\dot{V})$$

or

$$\frac{\partial}{\partial r}\left[g\frac{\partial \chi}{\partial z}w - \frac{\partial}{\partial z}(\chi C)u\right] +$$

$$\frac{\partial}{\partial z}\left[(\chi\xi(\zeta + f) + C\frac{\partial \chi}{\partial r})u + \frac{\partial}{\partial z}(\chi C)w\right] = g\frac{\partial Q}{\partial r} + \frac{\partial}{\partial z}(CQ) + \frac{\partial}{\partial z}(\chi\xi\dot{V}) \qquad (2.28)$$

using (2.16). Then substitution for u and w from Eqs. (2.25) into Eq. (2.28) gives

$$\frac{\partial}{\partial r}\left[g\frac{\partial \chi}{\partial z}\frac{1}{\rho r}\frac{\partial \psi}{\partial r} + \frac{\partial}{\partial z}(\chi C)\frac{1}{\rho r}\frac{\partial \psi}{\partial z}\right] -$$

$$\frac{\partial}{\partial z}\left[\left(\xi\chi(\zeta + f) + C\frac{\partial \chi}{\partial r}\right)\frac{1}{\rho r}\frac{\partial \psi}{\partial z} - \frac{\partial}{\partial z}(\chi C)\frac{1}{\rho r}\frac{\partial \psi}{\partial r}\right] = g\frac{\partial Q}{\partial r} + \frac{\partial}{\partial z}(CQ) + \frac{\partial}{\partial z}(\chi\xi\dot{V})$$
$$(2.29)$$

This is called the *Sawyer-Eliassen equation* following the work of Eliassen (1951) and Sawyer (1956) (Sawyer derived a similar equation for frontal circulations in rectangular geometry). The equation was investigated in context of the tropical cyclones by Willoughby (1979) and Shapiro and Willoughby (1982). The discriminant of the Sawyer-Eliassen equation is

$$D = -g\frac{\partial \chi}{\partial z}\left(\xi\chi(\zeta + f) + C\frac{\partial \chi}{\partial r}\right) - \left[\frac{\partial}{\partial z}(\chi C)\right]^2 \qquad (2.30)$$

Comparison with Eq. (5) of Shapiro and Willoughby (1982) shows that Eq. (2.29) is elliptic if $D > 0$.

The Sawyer-Eliassen equation contains three spatially-varying parameters characterizing:

- the *static stability*

$$N^2 = -g\frac{\partial ln\chi}{\partial z};$$

- the *inertial stability*

$$I^2 = \frac{1}{r^3}\frac{\partial M^2}{\partial r} = \xi(\zeta + f);$$

- the *baroclinicity*

$$B^2 = \frac{1}{r^3}\frac{\partial M^2}{\partial z} = \xi S.$$

Shapiro and Willoughby showed solutions of the Sawyer-Eliassen equation for point sources (i.e. azimuthal rings) of heat and azimuthal momentum, based on the earlier work of Eliassen (1951). These solutions are reproduced in Fig. 2.6. The flow through the heat source follows a nearly vertical surface of constant absolute angular momentum, while that for a momentum source follows a nearly horizontal isentropic surface. For sources of heat and absolute angular momentum, the sense of the flow is upward and outward, respectively. For sinks the flow is reversed. The vortex axis lies to the left of the figure. In the warm-core system of panels (c) and (f), the warm anomaly that supports the slope of the constant absolute angular momentum and isentropic surfaces increases towards the upper left.

Shapiro and Willoughby used the Sawyer-Eliassen equation also to calculate the secondary circulation induced by point sources of heat and absolute angular momentum in balanced, tropical-cyclone-like vortices in a partially bounded domain using the so-called method of images. Again they found that the secondary circulation through a heat source is primarily vertical, and that through a momentum source is primarily horizontal as shown in Fig. 2.7. The streamlines form two counter-rotating cells of circulation (or gyres) that extend outside the source. There is a strong flow between these gyres and a weaker return flow on the outside. The flow emerges from the source, spreads outward through a large volume surrounding it, and converges back into it from below. Thus, compensating subsidence surrounds heat-induced updraughts and compensating inflow lies above and below momentum-induced outflow. The horizontal scale of the gyres is just the local Rossby radius of deformation, so that the ratio of horizontal to vertical scale is N/I.

Radial gradients of absolute angular momentum of the primary circulation affect the radial scale of the dipoles just as the static stability affects their vertical scale. For a fixed static stability, the gyres tend to be elongated vertically when the inertial-stability parameter I^2 is large and elongated horizontally when I^2 is small. Vertical gradients of absolute angular momentum associated with the vertical shear of the primary circulation tilt the updraught through a heat source because the path of least resistance for the rising air lies along surfaces of constant absolute angular momentum. Likewise, horizontal temperature gradients associated with the vertical shear deflect the flow through momentum sources from the horizontal because the path of least resistance in this case lies along isentropic surfaces. Although the flow
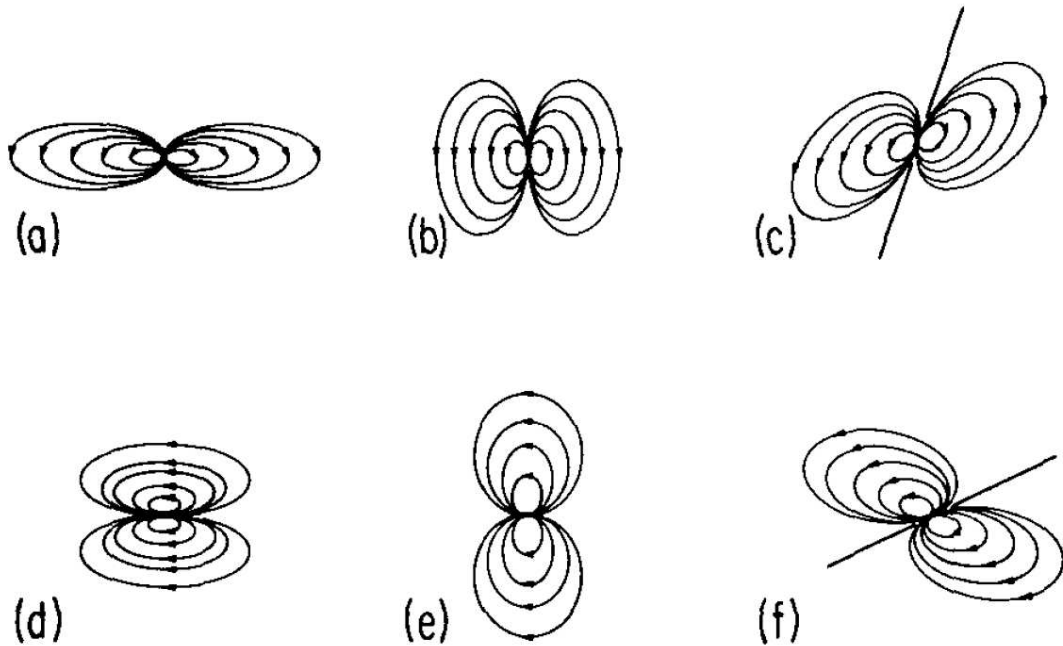
Figure 2.6: Streamfunction responses to point sources of: (a) Heat in a barotropic vortex with weak inertial stability, (b) heat in a barotropic vortex with strong inertial stability, (c) heat in a baroclinic vortex, (d) momentum in a barotropic vortex with weak inertial stability, (e) momentum in a barotropic vortex with strong inertial stability, and (f) momentum in a baroclinic vortex. (Based on Figs. 8, 9, 11, and 12 of Eliassen, (1951).)

associated with a heat (momentum) source lies generally along the M-surface (θ-surface), it does have a small component across this surface. It is the advection by this component that causes evolution of the primary circulation. It can be shown that the swirling flow remains in approximate gradient-wind balance provided the time scale of the forcing is longer than the orbital period of the primary circulation about the vortex centre.

It turns out that the induced secondary circulation in balanced flows tend to cancel the direct effect of forcing. For example, the work done by expansion in the updraught induced by a heat source nearly balances the actual heating so that the increase in temperature is relatively small. Similarly, a momentum source produces outflow that advects compensating low values of absolute angular momentum from the central region of the vortex.

In section 2.15 we show how the Sawyer-Eliassen equation can be used as one of a set of equations to calculate the evolution of a balanced vortex.
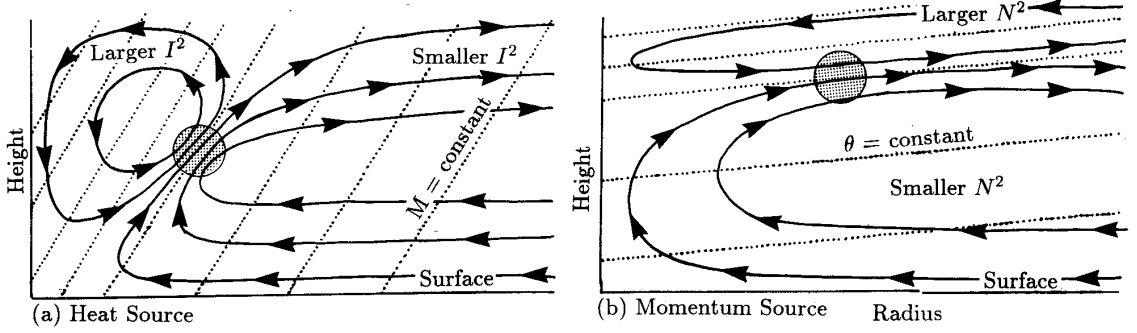
Figure 2.7: Secondary circulation induced in a balanced vortex by (a) a heat source and (b) a cyclonic momentum source showing the distortion induced by variation in inertial stability, I^2 and thermodynamic stability. N^2, and baroclinicity S^2. The strong motions through the source follow lines of constant angular momentum for a heat source and of constant potential temperature for a momentum source. From Willoughby (1995).

2.10.1 Ertel PV and the discriminant

I show now that D is proportional to the Ertel potential vorticity defined as

$$P = \frac{(\omega + \mathbf{f}) \cdot \nabla\theta}{\rho}.$$

For a symmetric vortex with tangential wind speed distribution $v(r,z)$, $\omega + \mathbf{f} = -(\partial v/\partial z)\hat{\mathbf{r}} + (\zeta + f)\hat{\mathbf{z}}$ and $\nabla\theta = -(1/\chi^2)\nabla\chi = -(1/\chi^2)[(\partial\chi/\partial r)\hat{\mathbf{r}} + (\partial\chi/\partial z)\hat{\mathbf{z}}]$ so that

$$P = \frac{1}{\rho\chi^2}\left[\frac{\partial v}{\partial z}\frac{\partial\chi}{\partial r} - (\zeta + f)\frac{\partial\chi}{\partial z}\right]$$

Then

$$g\rho\chi^3\xi P = -g\frac{\partial\chi}{\partial z}\xi\chi(\zeta + f) + \xi S\chi g\frac{\partial\chi}{\partial r}$$

or

$$g\rho\chi^3\xi P = -g\frac{\partial\chi}{\partial z}\left[\chi\xi(\zeta + f) + C\frac{\partial\chi}{\partial r}\right] + g\frac{\partial\chi}{\partial z}C\frac{\partial\chi}{\partial r} + \chi\frac{\partial C}{\partial z}g\frac{\partial\chi}{\partial r}$$

or

$$g\rho\chi^3\xi P = -g\frac{\partial\chi}{\partial z}\left[\chi\xi(\zeta + f) + C\frac{\partial\chi}{\partial r}\right] + g\frac{\partial\chi}{\partial r}\frac{\partial}{\partial z}(C\chi)$$

Finally

$$g\rho\chi^3\xi P = -g\frac{\partial\chi}{\partial z}\left[\chi\xi(\zeta + f) + C\frac{\partial\chi}{\partial r}\right] - \left(\frac{\partial}{\partial z}(C\chi)\right)^2$$

i.e.

$$g\rho\chi^3\xi P = D \tag{2.31}$$

2.10.2 The forcing term for ψ in terms of generalized buoyancy

Consider the forcing term for Eq. (2.30). The term can be written:

$$F = -g\frac{\partial}{\partial r}\left(\frac{1}{\theta^2}\frac{d\theta}{dt}\right) - \frac{\partial}{\partial z}\left(C\frac{1}{\theta^2}\frac{d\theta}{dt}\right)$$

The generalized buoyancy (Eq. 2.78) is $\mathbf{b_e} = \mathbf{g_e}(\theta - \theta_e)/\theta_e$, where $\mathbf{g_e} = (C, 0, -g)$. With the anelastic approximation that $1/\theta \approx 1/\theta_e \approx 1/\Theta$, where Θ is some vertically averaged value of θ_e we have that

$$\frac{d\mathbf{b_e}}{dt} \approx \frac{1}{\Theta}\frac{d\theta}{dt}\mathbf{g_e}$$

Now

$$\hat{\theta}\cdot\nabla\wedge\frac{d\mathbf{b_e}}{dt} = \frac{\partial}{\partial r}\left(\frac{db_{ez}}{dt}\right) - \frac{\partial}{\partial z}\left(\frac{db_{er}}{dt}\right) \approx \frac{\partial}{\partial r}\left(\frac{g}{\Theta}\frac{d\theta}{dt}\right) - \frac{\partial}{\partial z}\left(\frac{C}{\Theta}\frac{d\theta}{dt}\right)$$

so that

$$F \approx \frac{1}{\Theta}\hat{\theta}.\nabla\wedge\frac{d\mathbf{b_e}}{dt} \tag{2.32}$$

2.10.3 The Sawyer-Eliassen equation and toroidal vorticity equation

The Sawyer-Eliassen equation is an approximate form of the local time derivative of equation for the toroidal vorticity $\eta = \partial u/\partial z - \partial w/\partial r$. Assuming the most general form of the continuity equation

$$\frac{\partial\rho}{\partial t} + \frac{1}{r}\frac{\partial}{\partial r}(r\rho u) + \frac{\partial}{\partial z}(\rho w) = 0$$

the toroidal vorticity equation may be written as

$$r\frac{D}{Dt}\left(\frac{\eta}{r\rho}\right) = \frac{1}{\rho}\frac{\partial C}{\partial z} + \frac{1}{\rho^2\chi}\left(\frac{\partial\chi}{\partial z}\frac{\partial p}{\partial r} - \frac{\partial\chi}{\partial r}\frac{\partial p}{\partial z}\right) \tag{2.33}$$

where $D/Dt \equiv \partial/\partial t + \mathbf{u}\cdot\nabla$ and $\eta/(r\rho)$ is a 'potential toroidal vorticity', where the analogous 'depth' is 'r', the radius of a toroidal vortex ring (see appendix). If thermal wind balance exists, the right-hand-side of (2.36) may be written as

$$\frac{1}{\rho\chi}\left(g\frac{\partial\chi}{\partial r} + \frac{\partial}{\partial z}(C\chi)\right).$$

Then the time derivative of (4.41) is

$$\frac{\partial}{\partial t}\left[r\frac{D}{Dt}\left(\frac{\eta}{r\rho}\right)\right] = \frac{\partial}{\partial t}\left[\frac{1}{\rho\chi}\left(g\frac{\partial\chi}{\partial r} + \frac{\partial}{\partial z}(C\chi)\right)\right] \tag{2.34}$$

The right-hand-side of (2.34) gives the Sawyer-Eliassen equation when the thermal wind equation (2.11) is satisfied for all time. Then consistency requires that the left-hand-side is identically zero.

2.10.4 Buoyancy relative to a balanced vortex

Tropical cyclones are rapidly-rotating warm-cored vortices and the warm core is therefore positively buoyant relative to the environment. However, we have seen that on the cyclone scale, hydrostatic and gradient-wind balance exist to a good approximation and the radial density (or buoyancy) gradient is related by the thermal-wind equation to the decay in the mean tangential circulation and density with height. Clearly much of the radial gradient of buoyancy force cannot be thought of as being "available" for "driving" a secondary (or toroidal) circulation of the vortex that is necessary for vortex amplification. Nevertheless, hydrostatic balance may be a poor approximation in individual convective clouds and a pertinent question is whether these clouds have significant local (unbalanced) buoyancy, which in turn might play an important role in the dynamics of storm intensification. This important question was addressed by Braun (2002), who answered it in the affirmative on the basis of his simulations of Hurricane Bob (1991). To address this question it is necessary to define the perturbation pressure and perturbation density relative to some vortex-scale pressure and density distributions. The simplest case is when the primary vortex is approximately steady and axisymmetric. Then we may take reference distributions $p_{ref}(r, z)$ and $\rho_{ref}(r, z)$, respectively, that are in thermal wind balance with the tangential flow field $v(r, z)$. We saw how to do this in section 2.3 using the method of characteristics. We may use $\rho_{ref}(r, z)$ and $p_{ref}(r, z)$ as alternative reference quantities to define the buoyancy force in Eq. (2.18) (similar to Braun 2002), without affecting the derivation of this equation. We denote the generalized buoyancy force so calculated by $\mathbf{b_B}$. It follows that $\mathbf{b_B} \equiv \mathbf{0}$ in the axisymmetric balanced state, whereas, if the reference pressure and density at $r = R$ are used, $\mathbf{b}$ equals some nonzero function $\mathbf{b_0}(r, z)$. Clearly, the partition of force between perturbation pressure gradient and buoyancy will be different for the reference state characterized by $\rho_0(r, z)$ and $p_0(r, z)$ and interpretations of the dynamics will be different also, albeit equivalent to those using the more conventional reference quantities that depend on height only.

In the more general case, when the vortex structure has marked asymmetries and/or is evolving in time, it is necessary to allow for the azimuthal and/or time variations of the reference state as was done by Zhang *et al.* (2000) and Braun (2002).

2.10.5 Buoyancy in axisymmetric balanced vortices

Axisymmetric balanced models of tropical cyclone intensification (e.g. Ooyama, 1969) appear to capture many important observed features of tropical cyclone behaviour. However, in an axisymmetric model that assumes exact thermal wind balance, $\mathbf{b_B}(r, z, t) \equiv \mathbf{0}$ and the corresponding $\partial p'/\partial z \equiv 0$, even though there may be heat sources or sinks present that generate buoyancy $\mathbf{b}$. It is clear from the foregoing discussion that any diabatic heating or cooling in such models is incorporated directly into the balanced state, changing $\mathbf{b}(r, z, t)$, while $\mathbf{b_B}(r, z, t)$ remains identically zero

by definition. Obviously, nonzero values of $\mathbf{b_B}$ relate to *unbalanced motions* provided that the appropriate reference state as defined above has been selected for the definition of buoyancy at any given time. It may be helpful to think of $\mathbf{b}$ as characterizing the *system buoyancy* and $\mathbf{b_B}$ as characterizing the *local buoyancy*.

2.11 Origins of buoyancy in tropical cyclones

Tropical cyclones intensify when, as a direct or indirect result of latent heat release, the buoyancy b in the core increases. To a first approximation, the direct effect of latent heat release in saturated ascending air, such as in the eyewall clouds, or in the cores of individual convective clouds, is to maintain the air close to the moist adiabat from which the updraught originates. The indirect effect of latent heat release is to produce subsidence (or at least reduce the rate-of-ascent) in clear-air regions adjacent to (i.e. within a local Rossby radius of deformation of) deep convection. There is observational evidence (e.g. Betts, 1986; Xu and Emanuel, 1992) and evidence from model studies (Bretherton and Smolarkewicz, 1989) that, again to a first approximation, the clear air properties are adjusted towards the same saturation moist adiabat as in the neighbouring convective cores, albeit in this case to one calculated reversibly. In either case, the thermal structure of the troposphere in a mature tropical cyclone, and thereby the radial distribution of buoyancy, would be determined largely by the radial distribution of moist entropy at the top of the subcloud layer, at least in regions of ascent (see e.g. Emanuel, 1991). This view relates essentially to the generation of system buoyancy.

The extent to which local (unbalanced) buoyancy is produced will depend amongst other things on the rate at which the buoyancy is generated and the scale on which it is generated. For example, the simulations by Braun (2002) indicate that much of the eyewall updraft mass flux occurs within small-scale updrafts that are locally buoyant relative to the broad-scale thermal field of the vortex. A recent examination of the high resolution cloud resolving numerical simulation of the formation of Hurricane Diana (1984) has shown how buoyant cores growing in the rotation-rich environment of an incipient storm produce intense cyclonic vorticity anomalies in the lower troposphere by vortex-tube stretching (Hendricks, *et al.* 2003). These intense vorticity anomalies subsequently merge and axisymmetrize to intensify the balanced circulation of the incipient mesoscale vortex (Montgomery and Enagonio 1998; Möller and Montgomery 2000; Montgomery and Brunet 2002). In this case, subsidence warming is not the primary means for generating the cyclone's warm core. Rather, the warm core temperature that materializes within the developing mesoscale vortex results from the tendency of the high vorticity cores of the buoyant plumes to 'trap' the heat releases by the condensation process, as one might anticipate from local Rossby adjustment considerations (Schubert *et al.* 1980, Sec. 9) and quasi-balanced dynamics within enhanced vortical regions (Schubert and Hack 1982, Montgomery *et al.* 2003).

2.12 A balanced theory of vortex evolution

The establishment of the Sawyer-Eliassen equation is an important step in formulating a balanced theory for the evolution of an axisymmetric vortex. In such a theory we need prognostic equations for the evolution of the primary circulation, i.e. for the azimuthal wind and potential temperature. These are just the axisymmetric forms of Eqs. (2.2) and (2.5), i.e. Eqs. (2.26) and (2.27). Given expressions for $\dot{V}$ and $\dot{\theta}$ and initial conditions for v and θ, we can solve the Sawyer-Eliassen equation for the streamfunction of the secondary circulation, ψ, given suitable boundary conditions on this quantity. This streamfunction gives the secondary circulation that keeps v and θ in thermal-wind balance for short time interval, Δt. The corresponding radial and vertical wind components may be obtained from the expressions (2.25) and the density therein can be obtained, in principle, from (2.14). A balanced set of equations of this type was solved by Sundqvist (1970).

2.13 Appendix to Chapter 2

2.13.1 The toroidal vorticity equation

The λ-component of vorticity, or toroidal vorticity is

$$\eta = \frac{\partial u}{\partial z} - \frac{\partial w}{\partial r} \tag{2.35}$$

The equation for η is derived as follows. Consider

$$\frac{\partial \eta}{\partial t} = \frac{\partial}{\partial t}\left(\frac{\partial u}{\partial z} - \frac{\partial w}{\partial r}\right) = \frac{\partial}{\partial z}\left(\frac{\partial u}{\partial t}\right) - \frac{\partial}{\partial r}\left(\frac{\partial w}{\partial t}\right)$$

This expression may be written

$$\frac{\partial \eta}{\partial t} = \frac{\partial}{\partial z}\left(-\mathbf{u}\cdot\nabla u + C - \frac{1}{\rho}\frac{\partial p}{\partial r} + F_u\right) - \frac{\partial}{\partial r}\left(-\mathbf{u}\cdot\nabla w - \frac{1}{\rho}\frac{\partial p}{\partial z} + F_w\right),$$

where, for completeness frictional stresses F_u, F_w, are included in the momentum equations. This equation reduces to

$$\frac{\partial \eta}{\partial t} = \frac{\partial C}{\partial z} + \frac{\partial}{\partial r}\left(\frac{1}{\rho}\right)\frac{\partial p}{\partial z} - \frac{\partial}{\partial z}\left(\frac{1}{\rho}\right)\frac{\partial p}{\partial r} + \frac{\partial}{\partial r}\left(\mathbf{u}\cdot\nabla w\right) - \frac{\partial}{\partial z}\left(\mathbf{u}\cdot\nabla u\right) + \frac{\partial F_u}{\partial z} - \frac{\partial F_w}{\partial r},$$

or

$$\frac{\partial \eta}{\partial t} + \mathbf{u}\cdot\nabla\eta = \frac{\partial C}{\partial z} + \frac{1}{\rho^2}\left(\frac{\partial \rho}{\partial z}\frac{\partial p}{\partial r} - \frac{\partial \rho}{\partial r}\frac{\partial p}{\partial z}\right) + \frac{\partial \mathbf{u}}{\partial r}\cdot\nabla w - \frac{\partial \mathbf{u}}{\partial z}\cdot\nabla u + \frac{\partial F_u}{\partial z} - \frac{\partial F_w}{\partial r}.$$

Now

$$\ln\theta = \kappa\ln p^* - (1-\kappa)\ln p - \ln\rho = -\ln\chi$$

so that

$$(1 - \kappa)\frac{dp}{p} + \frac{d\rho}{\rho} = \frac{d\chi}{\chi}$$

Then

$$\frac{1}{\rho^2}\left(\frac{\partial\rho}{\partial z}\frac{\partial p}{\partial r} - \frac{\partial\rho}{\partial r}\frac{\partial p}{\partial z}\right) = \frac{1}{\rho\chi}\left(\frac{\partial\chi}{\partial z}\frac{\partial p}{\partial r} - \frac{\partial\chi}{\partial r}\frac{\partial p}{\partial z}\right)$$

Again

$$\frac{\partial\mathbf{u}}{\partial x}\cdot\nabla w - \frac{\partial\mathbf{u}}{\partial z}\cdot\nabla u = \left(\frac{\partial u}{\partial r} + \frac{\partial w}{\partial z}\right)\left(\frac{\partial w}{\partial r} - \frac{\partial u}{\partial z}\right),$$

but the continuity equation now gives

$$\frac{\partial u}{\partial r} + \frac{\partial w}{\partial z} = -\frac{u}{r} - \frac{1}{\rho}\left(\frac{\partial\rho}{\partial t} + u\frac{\partial\rho}{\partial r} + w\frac{\partial\rho}{\partial z}\right) = -\frac{u}{r} + \rho\frac{D}{Dt}\left(\frac{1}{\rho}\right),$$

where $D/Dt \equiv \partial/\partial t + \mathbf{u}\cdot\nabla$. Thus the toroidal vorticity equation is

$$\frac{\partial\eta}{\partial t} + \mathbf{u}\cdot\nabla\eta = \frac{\partial C}{\partial z} + \frac{1}{\rho\chi}\left(\frac{\partial\chi}{\partial z}\frac{\partial p}{\partial r} - \frac{\partial\chi}{\partial r}\frac{\partial p}{\partial z}\right) + \left[\frac{u}{r} + \rho\frac{D}{Dt}\left(\frac{1}{\rho}\right)\right]\eta + \frac{\partial F_u}{\partial z} - \frac{\partial F_w}{\partial r},$$

or

$$r\frac{D}{Dt}\left(\frac{\eta}{r\rho}\right) = \frac{1}{\rho}\frac{\partial C}{\partial z} + \frac{1}{\rho^2\chi}\left(\frac{\partial\chi}{\partial z}\frac{\partial p}{\partial r} - \frac{\partial\chi}{\partial r}\frac{\partial p}{\partial z}\right) + \frac{1}{\rho}\left(\frac{\partial F_u}{\partial z} - \frac{\partial F_w}{\partial r}\right), \qquad (2.36)$$

Chapter 3

A SIMPLE BOUNDARY LAYER MODEL

3.1 The boundary layer equations

We consider now a simple model for the tropical cyclone boundary layer as described by Smith (2003). The boundary layer equations for a steady axisymmetric vortex in a homogeneous fluid on an f-plane are:

$$\frac{1}{r}\frac{\partial}{\partial r}(ru^2) + \frac{\partial}{\partial z}(uw) + \frac{v_{gr}^2 - v^2}{r} + f(v_{gr} - v) = \frac{\partial}{\partial z}\left(K\frac{\partial u}{\partial z}\right), \qquad (3.1)$$

$$\frac{1}{r^2}\frac{\partial}{\partial r}(r^2 uv) + \frac{\partial}{\partial z}(vw) + fu = \frac{\partial}{\partial z}\left(K\frac{\partial v}{\partial z}\right), \qquad (3.2)$$

$$\frac{1}{r}\frac{\partial}{\partial r}(ru\varphi) + \frac{\partial}{\partial z}(w\varphi) = \frac{\partial}{\partial z}\left(K\frac{\partial \varphi}{\partial z}\right), \qquad (3.3)$$

$$\frac{\partial}{\partial r}(ru) + \frac{\partial}{\partial z}(rw) = 0, \qquad (3.4)$$

where (u, v, w) is again the velocity vector in a stationary cylindrical coordinate system (r, ϕ, z), $v_{gr}(r)$ is the tangential wind speed at the top of the boundary layer, φ is a scalar quantity, taken here to be the dry static energy or the specific humidity, and K is an eddy diffusivity, which we assume here to be the same for momentum, heat and moisture. Let us assume that condensation does not occur in the boundary layer: we can check that saturation does not arise in the calculations. Taking the integral of Eqs. (3.1) - (3.4) with respect to z from $z = 0$ to the top of the boundary layer, $z = \delta$, and assuming that δ is a constant, we obtain:

$$\frac{d}{dr}(r\int_0^\delta u^2 dz) + [ruw]|_{z=\delta} + \int_0^\delta (v_{gr}^2 - v^2)dz + rf\int_0^\delta (v_{gr} - v)dz = -Kr\left.\frac{\partial u}{\partial z}\right|_{z=0}, \quad (3.5)$$

$$\frac{d}{dr}\left(r^2 \int_0^\delta uv\,dz\right) + [r^2 vw]\big|_{z=\delta} + fr^2 \int_0^\delta u\,dz = -Kr^2 \left.\frac{\partial v}{\partial z}\right|_{z=0}, \qquad (3.6)$$

$$\frac{d}{dr}\left(r \int_0^\delta u\varphi\,dz\right) + [rw\varphi]\big|_{z=\delta} = -Kr \left.\frac{\partial \varphi}{\partial z}\right|_{z=0}, \qquad (3.7)$$

$$\frac{d}{dr}\int_0^\delta ru\,dz + [rw]\big|_{z=\delta} = 0. \qquad (3.8)$$

Now

$$[ruw]_{z=\delta} = ru_b w_{\delta_+} + ru_{gr} w_{\delta_-},$$

where u_{gr} is the radial component of flow above the boundary layer, taken here to be zero, $w_{\delta_+} = \frac{1}{2}(w_\delta + |w_\delta|)$, and $w_{\delta_-} = \frac{1}{2}(w_\delta - |w_\delta|)$. Note that w_{δ_+} is equal to w_δ if the latter is positive and zero otherwise, while w_{δ_-} is equal to w_δ if the latter is negative and zero otherwise. The assumption that δ is a constant may have to be reassessed later, but allowing it to vary with radius precludes the relatively simple approach that follows. A bulk drag law is assumed to apply at the surface:

$$K \left.\frac{\partial \mathbf{u}}{\partial z}\right|_{z=0} = C_D |\mathbf{u_b}| \mathbf{u_b},$$

where C_D is a drag coefficient and $\mathbf{u_b} = (u_b, v_b)$. Here u_b and v_b denote the values of u and v in the boundary layer, which are assumed to be independent of depth. A similar law is taken for φ:

$$K \left.\frac{\partial \varphi}{\partial z}\right|_{z=0} = C_\varphi |\mathbf{u_b}|(\varphi_b - \varphi_s),$$

where φ_b and φ_s are the values of φ in the boundary layer and at the sea surface, respectively. In the case of temperature φ_s is the sea surface temperature and in the case of moisture it is the saturation specific humidity at this temperature. Following Shapiro (1983, p1987) we use the formula $C_D = C_{D0} + C_{D1}|\mathbf{u_b}|$, where $C_{D0} = 1.1 \times 10^{-3}$ and $C_{D1} = 4 \times 10^{-5}$. Further, we assume here that $C_\varphi = C_D$, although there is mounting evidence that they are not the same and that neither continue to increase linearly with wind speed at speeds in excess of, perhaps, 25 m s^{-1} (Emanuel, 1995b).

Carrying out the integrals in Eqs. (3.5) - (3.8) and dividing by δ gives

$$\frac{d}{dr}(ru_b^2) = -\frac{w_{\delta+}}{\delta}ru_b - (v_{gr}^2 - v_b^2) - rf(v_{gr} - v_b) - \frac{C_D}{\delta}r(u_b^2 + v_b^2)^{1/2}u_b, \qquad (3.9)$$

$$\frac{d}{dr}(ru_b rv_b) = -r\frac{w_{\delta+}}{\delta}rv_b - r\frac{w_{\delta-}}{\delta}rv_{gr} - r^2 fu_b - \frac{C_D}{\delta}r^2(u_b^2 + v_b^2)^{1/2}v_b, \qquad (3.10)$$

$$\frac{d}{dr}(ru_b\varphi_b) = -\frac{w_{\delta+}}{\delta}r\varphi_b - r\frac{w_{\delta-}}{\delta}\varphi_{\delta+} + \frac{C_\varphi}{\delta}r(u_b^2 + v_b^2)^{1/2}(\varphi_s - \varphi_b), \qquad (3.11)$$

and

$$\frac{d}{dr}(ru_b) = -r\frac{w_\delta}{\delta}, \qquad (3.12)$$

which may be written

$$\frac{du_b}{dr} = -\frac{w_\delta}{\delta} - \frac{u_b}{r}. \qquad (3.13)$$

Moreover, for any dependent variable η

$$\frac{d}{dr}(ru_b\eta) = ru_b\frac{d\eta}{dr} + \eta\frac{d}{dr}(ru_b) = ru_b\frac{d\eta}{dr} - \frac{w_\delta}{\delta}r\eta,$$

where η is either u_b, v_b or φ_b. Then Eqs. (3.9) and (3.10) become

$$u_b\frac{du_b}{dr} = u_b\frac{w_{\delta-}}{\delta} - \frac{(v_{gr}^2 - v_b^2)}{r} - f(v_{gr} - v_b) - \frac{C_D}{\delta}(u_b^2 + v_b^2)^{1/2}u_b, \qquad (3.14)$$

$$u_b\frac{dv_b}{dr} = \frac{w_{\delta-}}{\delta}(v_b - v_{gr}) - (\frac{v_b}{r} + f)u_b - \frac{C_D}{\delta}(u_b^2 + v_b^2)^{1/2}v_b. \qquad (3.15)$$

Equation (3.11) becomes

$$u_b\frac{d\varphi_b}{dr} = \frac{w_{\delta-}}{\delta}(\varphi_b - \varphi_{\delta+}) + \frac{C_\varphi}{\delta}(u_b^2 + v_b^2)^{1/2}(\varphi_s - \varphi_b) - R_b, \qquad (3.16)$$

where $\varphi_{\delta+}$ is the value of φ just above the boundary layer. The term $-R_b$ is added to the equation when φ is the dry static energy and represents the effects of radiative cooling, respectively.

Equations (3.14) - (3.16) form a system that may be integrated radially inward from some large radius R to find u_b, v_b, φ_b and w_δ as functions of r, given values of these quantities at $r = R$. First Eq. (3.14) must be modified using (3.13) to give an expression for w_δ. Combining[1] these two equations gives

$$w_\delta = \frac{\delta}{1+\alpha}\left[\frac{1}{u_b}\left\{\frac{(v_{gr}^2 - v_b^2)}{r} + f(v_{gr} - v_b) + \frac{C_D}{\delta}(u_b^2 + v_b^2)^{1/2}u_b\right\} - \frac{u_b}{r}\right], \qquad (3.17)$$

where α is zero if the expression in square brackets is negative and unity if it is positive.

―――――――――――――――――――――――――

[1]Eq. (3.14) is written in the form

$$u_b\frac{w_{\delta-}}{\delta} = u_b\frac{du_b}{dr} + \{...\} \quad \text{and} \quad \frac{du_b}{dr}$$

is eliminated from this expression using (3.13). Note that if $w_\delta < 0$, $w_\delta = w_{\delta-}$, in which case $\alpha = 1$. If $w_\delta > 0$, $w_{\delta-} = 0$, in which case $\alpha = 0$.

3.2 Shallow convection

An important feature of the convective boundary layer (CBL) over the tropical oceans in regions of large-scale subsidence is the near ubiquity of shallow convection. Such regions include the outer region of hurricanes. Shallow convection plays an important role in the exchange of heat and moisture between the subcloud layer, the layer modelled in this paper, and the cloudy layer above. Excellent reviews of the CBL structure are given by Emanuel (1994, Chapter 13) and Betts (1997). Over much of the tropical Pacific Ocean, for example, in regions of subsidence, the subcloud layer is typically 500 m deep and is well-mixed, with relatively uniform vertical profiles of potential temperature, specific humidity and dry or moist static energy. The cloudy layer is capped by an inversion at an altitude of about 800 mb. A similar structure was found in the outer region of Hurricane Eloise (1975) by Moss and Merceret (1976), the mixed layer depth being about 650 m in this case. The clouds, known as tradewind cumuli, are widely spaced and have their roots in the subcloud layer. They generally don't precipitate, but evaporate into the dry subsiding air that penetrates the inversion, thereby moistening and cooling the subcloud layer. In turn, the compensating subsidence in the environment of clouds transports potentially warm and dry air into the subcloud layer. This drying opposes the moistening of the subcloud layer by surface fluxes, keeping its relative humidity at values around 80 %. The equilibrium state of the CBL, including its depth and that of the subcloud layer, is governed primarily by radiative cooling, subsidence, convective transports, and surface latent and sensible heat fluxes (Emanuel, *op. cit.*, Betts, *op. cit.*). Modelling the subcloud layer requires a knowledge of the cloud-base mass flux, which together with the large-scale subsidence, determines the rate at which cloud layer air enters the subcloud layer. Emanuel (1989) used a simple cloud model to determine the mass flux of shallow convection, while Zhu and Smith (2002) use the closure scheme of Arakawa (1969), in which the mass flux is assumed to be proportional to the degree of convective instability between the subcloud layer and that above. As we do not predict the thermodynamic variables represented by $\varphi_{\delta+}$ above the boundary layer in this simple model, we simply choose a constant value for the mass flux of shallow convection, w_{sc}, and add this to $w_{\delta-}$ in Eqs. (3.14) - (3.16) (even if $w_{\delta-} = 0$). However, w_δ in Eq. (3.9) is left unchanged as shallow convection does not cause a *net* exchange of mass between the cloud and subcloud layers. The value for w_{sc} is chosen to ensure that the thermodynamic profile at large radius is close to radiative-convective equilibrium (see section 5).

3.3 Starting conditions at large radius

We assume that the flow above the boundary layer is in approximate geostrophic balance at large radii where the boundary layer is essentially governed by Ekman-like dynamics. Specifically we assume that at $r = R$, far from the axis of rotation, the flow above the boundary layer is steady and in *geostrophic* balance with tangential

wind $v_{gr}(R)$. In addition we take C_D to be a constant equal to $C_{D0} + C_{D1}v_{gr}(R)^2$. Then u_b and v_b satisfy the equations:

$$f(v_{gr} - v_b) = -\frac{C_D}{\delta}(u_b^2 + v_b^2)^{1/2}u_b, \qquad (3.18)$$

$$fu_b = -\frac{C_D}{\delta}(u_b^2 + v_b^2)^{1/2}v_b. \qquad (3.19)$$

Let $(u_b, v_b) = v_{gr}(u', v')$ and $\Lambda = f\delta/(C_D v_{gr})$. Then equations (3.18) and (3.19) become

$$\Lambda(1 - v') = -(u'^2 + v'^2)^{1/2}u', \qquad (3.20)$$

and

$$\Lambda u' = -(u'^2 + v'^2)^{1/2}y. \qquad (3.21)$$

The last two equations have the solution

$$v' = -\frac{1}{2}\Lambda^2 + (\frac{1}{4}\Lambda^4 + \Lambda^2)^{1/2}. \qquad (3.22)$$

and

$$u' = -[(1 - v')v']^{1/2}, \qquad (3.23)$$

whereupon u_b and v_b follow immediately on multiplication by v_{gr}. The vertical velocity at $r = R$ can be diagnosed in terms of v_{gr} and its radial derivative using the continuity equation (10.33).

   The starting values for the temperature T_b and specific humidity q_b in the boundary layer are 25°C and 15 g kg^{-1}, respectively, giving a relative humidity of 72%. The value for q_b is the same as the mixed layer value observed by Moss and Merceret (1976, Fig 4), but T_b cannot be compared with their observations as they showed only potential temperature.

   With the starting values for u_b and v_b determined by Eqs. (3.22) and (3.23), Eqs. (3.14) - (3.16) may be solved numerically, given the radial profile v_{gr}. We choose $R = 500$ km. Radial profiles of selected dynamical quantities in the boundary layer and at the top of it are shown in Fig. 3.1 for this calculation. At large radii ($r > 350$ km), the mean vertical motion at the top of the boundary layer, $\overline{w}_\delta$, is downward and the total wind speed $|\mathbf{v_b}| = \sqrt{u_b^2 + v_b^2}$ is less than that at the top of the boundary layer, v_{gr}. As r decreases, both u_b and v_b increase in magnitude, as does v_{gr}, the maximum value of v_b occurring just inside the radius of maximum tangential wind speed (RMW) above the boundary layer. As a result, the frictional force, $\mathbf{F} = C_d|\mathbf{v_b}|\mathbf{v_b}/\delta$ increases, and in particular its radial component, F_r, denoted by fri in the top right panel of Fig 3.1. The net radially-inward pressure gradient force per unit mass, $(v_{gr}^2 - v_b^2)/r + f(v_{gr} - v_b)$, denoted by pgf, increases also with decreasing

---

[2]It is possible to take $C_{D0} + C_{D1}|\mathbf{u_b}(R)|$ and solve the equations for u_b and v_b numerically, but the result is essentially no difference from basing C_D on v_{gr}
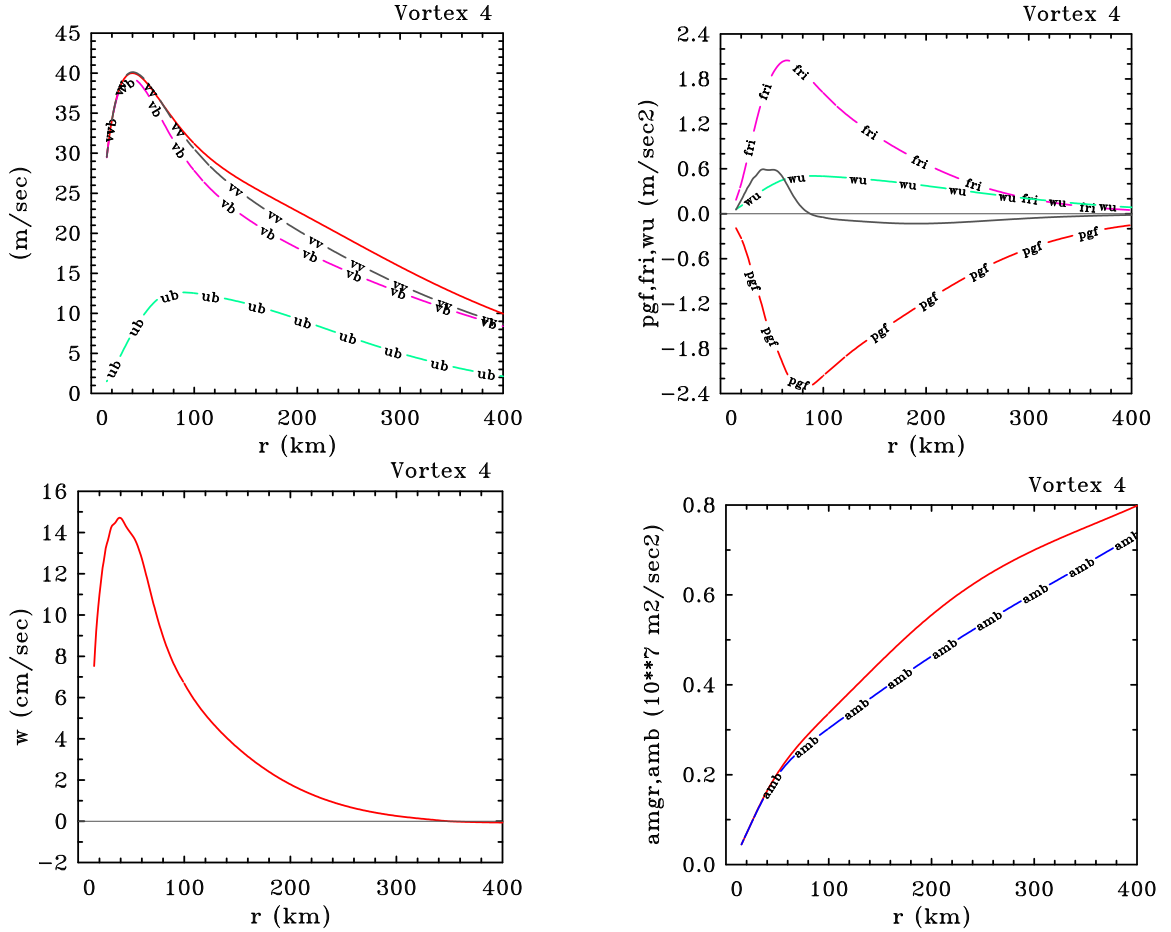
Figure 3.1: Radial profiles of selected dynamical quantities in the boundary layer calculation: (top left) tangential and radial components of wind speed in the boundary layer (u_b, v_b), total wind speed in the boundary layer, vv, and tangential wind speed above the boundary layer (v_{gr} - the unmarked solid line) [Units m s^{-1}]; (top, right) radial pressure gradient force (pgf) and frictional force (fri) per unit mass in the boundary layer, together with the force associated with the downward flux of radial momentum through the top of the boundary layer (wu) [Units 1.0×10^{-3} m s^{-2}] and the sum of these three forces (solid line); (bottom left) vertical velocity at the top of the boundary layer, w_δ [Units cm s^{-1}]; (bottom right) absolute angular momentum above the boundary layer (solid line) and in the boundary layer (amb) [Units 1.0×10^7 m^2 s^{-2}].

r, at least for large r, but more rapidly than the frictional force. The reason is that columns of fluid partially conserve their absolute angular momentum as they converge in the boundary layer and despite some frictional loss to the surface, their rotation rate increases. The increase in v_b is assisted by the downward transfer of tangential momentum from above, represented by the term $(w_{\delta-} + w_{sc})(v_b - v_{gr})/\delta$ in Eq. (3.15), although this effect turns out to be very small. The downward transfer of (zero) radial momentum, represented by the term $(w_{\delta-} + w_{sc})u_b/\delta$ in Eq. (3.14), is denoted by wu in Fig. 3.1, but this also makes a negligible contribution to the force balance in the boundary layer. For the typical tangential wind profile used, v_b increases faster than v_{gr} as r decreases inside a radius of about 200 km. In this region, pgf decreases faster than $wu + fri$ so that eventually the *net* radial force $pgf - wu - fri$ changes sign. This change occurs well before the RMW is reached. When $pgf - wu - fri$ becomes positive, the radial inflow decelerates, but v_b continues to increase as columns of air continue to move inwards. Eventually, v_b asymptotes to v_{gr} and pgf tends to zero, but at no point does the tangential wind speed become supergradient. Nevertheless, as pgf tends to zero, the net outward force, primarily due to friction, becomes relatively large and the inflow decelerates very rapidly. The mean vertical velocity at the top of the boundary layer increases steadily with decreasing r and reaches a maximum very close to the RMW: thereafter it decreases rapidly.

The lower right panel of Fig. 3.1 shows how the absolute angular momentum in the boundary layer decreases with decreasing radius as a result of the surface frictional torque. However, the rate of decrease is less rapid than that above the boundary layer and value in the boundary layer asymptotes to the value above the layer at inner radii.

It turns out that, except for a short adjustment length, which decreases in radial extent with increasing R, the calculations are relatively insensitive to the choice of R (see Smith, 2003). This insensitivity to R is not true of the thermodynamic fields as discussed below.

3.4   Thermodynamic aspects

The left panel of Fig. 3.2 shows the radial profiles of boundary layer temperature, specific humidity and saturation specific humidity, together with the saturation specific humidity at the sea surface temperature (q_{ss}), while the right panel shows the fluxes of sensible and latent heat at the surface and through the top of the boundary layer. At large radii, the wind speed is comparatively light and the boundary layer is in approximate[3] radiative-convective equilibrium. In particular, the air temperature just above the sea surface is only slightly lower than the sea surface temperature;

---

[3]The radiative-convective state is very sensitive to the choice of parameters including the mass flux of shallow convection and the boundary layer depth. We choose rounded numbers for these quantities so that the boundary layer is close to, but not exactly in equilibrium.
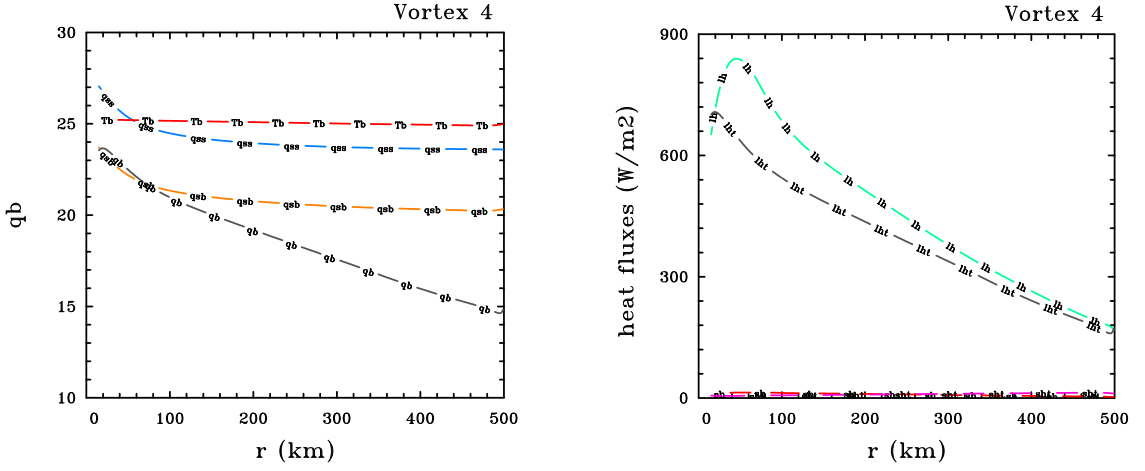
Figure 3.2: Radial profiles of selected thermodynamic quantities in the control calculation: (left panel) boundary layer temperature (Tb, unit deg. C), specific humidity (qb), saturation specific humidity (qsb), and the saturation specific humidity at the sea surface (qss) [Units gm kg^{-1}]; (right panel) latent heat fluxes from the sea surface (lh) and through the top of the boundary layer (lht)), and corresponding sensible heat fluxes (the two curves just above the abscissa labelled "sh" and "sht") [Units W m^{-2}].

the net sensible heat fluxes from the sea and through the top of the boundary layer approximately balance the radiative cooling; and the moistening of the boundary layer by the surface flux approximately balances the drying brought about by subsidence associated with shallow convection. The mass flux of shallow convection and the boundary layer depth are chosen to ensure this balance.

As r decreases and the surface wind speed increases, the surface moisture flux increases and the boundary layer progressively moistens. The increase in moisture contrast between the boundary layer and the air aloft leads to an increase in the flux of dry air through the top of the subcloud layer, which reduces the rate of moistening. This effect would be reduced in a more complete model in which the moisture content above the boundary layer is predicted. If shallow convection and radiative cooling are omitted, the rate of moistening is relatively rapid and the boundary layer saturates (i.e. $q_b = q_s$ at a relatively large radius (453 km), although, of course, then the boundary layer is not in radiative-convective equilibrium at $r = R$. In the present case, saturation occurs at a radius of about 80 km, but the air just above the sea surface does not (i.e. $q_b < q_{ss}$), which in terms of the simple model could be interpreted to mean that the boundary layer becomes topped by low cloud. A further consequence is that the surface moisture fluxes do not shut off. We have not allowed for the latent heat release in the inner core in these calculations as the degree of supersaturation is only about 1% (see Smith, 2003, Fig. 11). The degree of moisture disequilibrium at the sea surface is maintained by the fact that the saturation specific humidity increases as the surface pressure decreases. The latent heat fluxes

are much larger than the sensible heat fluxes.

Chapter 4

THE EMANUEL STEADY STATE HURRICANE MODEL

The basis of Emanuel's steady-state model for a tropical cyclone, described by Emanuel (1986), is Fig. 2.3. It is convenient to divide the domain into three regions as shown in Fig. 4.1. Regions I and II encompass the eye and eyewall regions, respectively, while Region III refers to that beyond the eyewall clouds. Region II is where the upward mass flux at the top of the boundary layer is large compared with the mass fluxes associated with shallow convection and precipitation-driven downdrafts. Smith (2003, p1013) estimated a value for w_{sc} for shallow convection (defined in section 2.9.1) of about 2 cm s^{-1}, based on the radiative equilibrium of the boundary layer at some large radius. In the boundary layer calculation shown in Fig. 3.1, $w > 5w_{sc}$ for $r < 2r_m$, where r_m is the radius of maximum tangential wind speed above the boundary layer. By comparison, Emanuel *op. cit.* takes the outer radius of Region II to be r_m on the basis that precipitation-driven downdrafts may be important up to this radius.

In pressure coordinates, the *gradient wind equation* and *hydrostatic equation* may be written as:

$$g\left(\frac{\partial z}{\partial r}\right)_p = \frac{M^2}{r^3} - \tfrac{1}{4}rf^2 \tag{4.1}$$

and

$$g\left(\frac{\partial z}{\partial p}\right)_r = -\alpha, \tag{4.2}$$

where $\alpha = 1/\rho$ is the specific volume. Eliminating the geopotential height of the pressure surface, gz, gives an alternative form of the thermal wind equation:

$$\frac{1}{r^3}\left(\frac{\partial M^2}{\partial p}\right)_r = -\left(\frac{\partial \alpha}{\partial r}\right)_p. \tag{4.3}$$

At this point it is convenient to introduce the saturation moist entropy, s^*, defined by:

$$s^* = c_p \ln \theta_e^*, \tag{4.4}$$
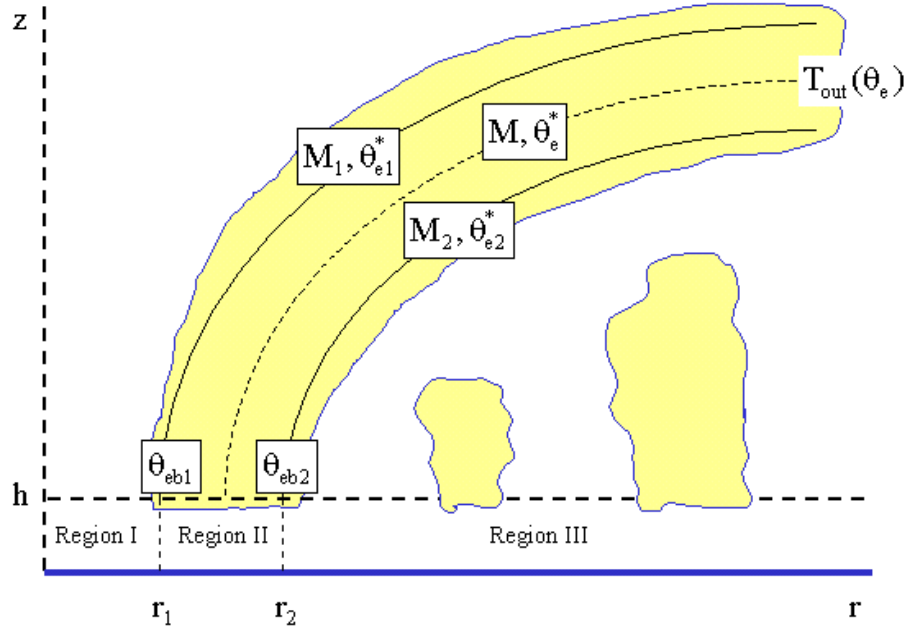
Figure 4.1: Schematic diagram of the secondary circulation of a mature tropical cyclone showing the eye and the eyewall clouds. The absolute angular momentum per unit mass, M, and equivalent potential temperature, θ_e of an air parcel are conserved after the parcel leaves the boundary layer and ascends in the eyewall clouds. The precise values of these quantities depend on the radius at which the parcel exits the boundary layer. At radii beyond the eyewall cloud, shallow convection plays an important role in moistening and cooling the lower troposphere above the boundary layer and warming and drying the boundary layer as indicated.

which is a state variable. Therefore we can regard α as a function of p and s^* and with a little manipulation we can express the thermal wind equation as:

$$\frac{1}{r^3}\left(\frac{\partial M^2}{\partial p}\right)_r = -\left(\frac{\partial \alpha}{\partial s*}\right)_p\left(\frac{\partial s^*}{\partial r}\right)_p. \tag{4.5}$$

I will show in an Appendix to this chapter that

$$\left(\frac{\partial \alpha}{\partial s^*}\right)_p = \left(\frac{\partial T}{\partial p}\right)_{s*}, \tag{4.6}$$

whereupon Eq. (4.5) becomes

$$\frac{1}{r^3}\left(\frac{\partial M^2}{\partial p}\right)_r = -\left(\frac{\partial T}{\partial p}\right)_{s*}\left(\frac{\partial s^*}{\partial r}\right)_p. \tag{4.7}$$

With the assumption that M and s^* surfaces coincide, i.e. $M = M(s^*)$, Eq. (4.7)

becomes

$$\frac{2M}{r^3}\left(\frac{\partial M}{\partial p}\right)_r = -\left(\frac{\partial T}{\partial p}\right)_{s*}\frac{ds^*}{dM}\left(\frac{\partial M}{\partial r}\right)_p. \tag{4.8}$$

Note that $(\partial T/\partial p)_{s*}$ is just the temperature lapse rate as a function of pressure along a moist adiabat. Now along an M surface,

$$\left(\frac{\partial M}{\partial r}\right)_p\delta r + \left(\frac{\partial M}{\partial p}\right)_r\delta p = 0, \tag{4.9}$$

so that the slope of an M surface in (r,p) space is

$$\left(\frac{dr}{dp}\right) = -\left(\frac{\partial M}{\partial p}\right)_r\Big/\left(\frac{\partial M}{\partial r}\right)_p. \tag{4.10}$$

Using Eq. (4.10), *the thermal wind equation* (Eq. 4.8) gives

$$\frac{1}{2}\left(\frac{dr^{-2}}{dp}\right)_M = -\frac{1}{2M}\left(\frac{\partial T}{\partial p}\right)_{s*}\frac{ds^*}{dM}, \tag{4.11}$$

which may be integrated upwards along the M (or s^*) surface to give

$$\frac{1}{r^2}|_M - \frac{1}{r_{out}^2}|_M = -\frac{1}{M}\frac{ds^*}{dM}[T - T_{out}(s^*, p_{out})], \tag{4.12}$$

where T_{out} is the outflow temperature along the M (or s^*) surface at some large radius r_{out}. If we assume that the air in the boundary layer and, in particular at the top of this layer $z = h$, is a constant[1], T_B, and that $r << r_{out}$, then

$$-r^2\frac{ds^*}{dM}[T_B - T_{out}(s^*, p_{out})] = M, \text{ at } z = h, \tag{4.13}$$

or, alternatively,

$$-[T_B - T_{out}(s^*, p_{out})]\frac{\partial s^*}{\partial r} = \frac{1}{2r^2}\frac{\partial M^2}{\partial r}, \text{ at } z = h. \tag{4.14}$$

This equation is a *vertically-integrated* (along an M-, or s^*-surface) *form of the thermal wind equation.*

Using the Exner function, π, instead of pressure, the *gradient wind equation* (Eq. 4.1) takes the form

$$M^2 = r^3\left[c_p T_B\frac{\partial \ln \pi}{\partial r} + \frac{1}{4}rf^2\right], \tag{4.15}$$

whereupon Eq. (4.14) can be written

$$-\frac{T_B - T_{out}(s^*, p_{out})}{T_B}\frac{\partial \ln \theta_e}{\partial r} = \frac{\partial \ln \pi}{\partial r} + \frac{1}{2}\frac{\partial}{\partial r}\left(r\frac{\partial \ln \pi}{\partial r}\right) + \frac{1}{2}\frac{rf^2}{c_p T_B}, \text{ at } z = h, \tag{4.16}$$

---

[1]According to the boundary layer model described in section 2.9, this is not a bad assumption if the sea surface temperature is uniform.

where it is assumed that $\theta_e^* = \theta_e$ at the top of the boundary layer.

Equation (4.16) may be integrated with respect to radius from r to some value r_o giving

$$-\ln\theta_{eo} + \ln\theta_e + \frac{1}{T_B}\int_r^{r_o} T_{out}(s^*, p_{out})\frac{\partial\ln\theta_e}{\partial r}dr$$

$$= \ln\pi_o - \ln\pi + \frac{1}{2}\left(r\frac{\partial\ln\pi}{\partial r}\right)_o - \frac{1}{2}\left(r\frac{\partial\ln\pi}{\partial r}\right) + \frac{1}{4}\frac{f^2}{c_p T_B}(r_o^2 - r^2), \text{ at } z = h. \quad (4.17)$$

We define

$$\bar{T}_{out} = \frac{1}{\ln(\theta_e^*/\theta_{eo})}\int_{\ln\theta_{eo}}^{\ln\theta_e^*} T_{out}d\ln\theta_e^*, \quad (4.18)$$

which is average outflow temperature weighted with the saturation moist entropy of the outflow angular momentum surfaces. Remember that θ_e^* along angular momentum surfaces is taken equal to θ_e where the surfaces meet the top of the boundary layer. Then (4.14) gives

$$\frac{T_B - \bar{T}_{out}}{T_B}\ln\left(\frac{\theta_e}{\theta_{eo}}\right) = \ln\left(\frac{\pi_o}{\pi}\right) + \frac{1}{2}\left(r\frac{\partial\ln\pi}{\partial r}\right)_{r_o} - \frac{1}{2}\left(r\frac{\partial\ln\pi}{\partial r}\right)$$

$$+ \frac{1}{4}\frac{f^2}{c_p T_B}(r_o^2 - r^2) \text{ at } z = h. \quad (4.19)$$

This relationship between the radial pressure distributions $p(r)$ and θ_e, which is valid at all radii where M- and s^*-surfaces coincide, exerts a powerful constraint on the structure of the mature steady axisymmetric tropical cyclone and is at the heart of the steady-state hurricane model developed by Emanuel (1986).

To complete the model we derive a second relationship between $p(r)$ and θ_e. Different expressions will be obtained for Regions II and III.

4.1 Region II

In Region II we consider the dynamics and thermodynamics of the boundary layer, which imposes a further constraint on the steady solution as it determines the radial distribution of both M and θ_e exiting the top of the layer. Referring to Section 3, it is possible to define a streamfunction ψ for the flow in the boundary layer, given by:

$$\rho r u_b = -\frac{\partial\psi}{\partial z}, \quad \rho r w_b = \frac{\partial\psi}{\partial r} \quad (4.20)$$

Then

$$u_b = -\frac{\psi(r, h)}{\rho r h}, \quad w_b = \frac{1}{\rho r}\frac{\partial\psi}{\partial r} \quad (4.21)$$

Let φ_b be the absolute angular momentum M or the moist entropy, s. Then φ_b satisfies

$$\psi(r, h)\frac{d\varphi_b}{dr} - rw_h[\varphi_h - \varphi_b] = -\frac{r}{\rho}\tau_\varphi(r, 0) \quad (4.22)$$

where τ_φ is the surface flux of φ. If the flow is out of the boundary layer, $(w > 0)$, then $\varphi_h = \varphi_b$ and neglecting shallow convection (see subsection 2.8.1), φ_b satisfies

$$\psi(r,h)\frac{d\varphi_b}{dr} = -\frac{r}{\rho}\tau_\varphi(r,0) \tag{4.23}$$

whereas if it is into the boundary layer $(w < 0)$,

$$\psi(r,h)\frac{d\varphi_b}{dr} = -\frac{r}{\rho}\tau_\varphi(r,0) + rw_h[\varphi_h - \varphi_b] \tag{4.24}$$

Then in Region II in Fig. 4.1, where the flow is out of the boundary layer and where convective downdrafts may be neglected,

$$\left.\frac{\partial s}{\partial M}\right|_{z=h} = \left.\frac{\tau_s}{\tau_M}\right|_{z=0} \tag{4.25}$$

The standard aerodynamic formulae are used for surface fluxes:

$$\begin{aligned}\tau_s &= -c_p C_k |\mathbf{V_s}|(\ln\theta_e - \ln\theta_{es}^*) \\ \tau_M &= -C_D |\mathbf{V_s}| rV_s,\end{aligned} \tag{4.26}$$

where $|\mathbf{V_s}|$ is the magnitude of the surface horizontal velocity, V_s is the tangential component of the surface wind, C_k and C_D are exchange coefficients for enthalpy and momentum and θ_{es}^* is the saturation equivalent potential temperature at the sea surface temperature. Then Eq. (4.13) gives

$$\ln\theta_e = \ln\theta_{es}^* - \mu\frac{C_D}{C_k}\frac{1}{c_p(T_B - T_{out})}\left(V^2 + \frac{1}{2}rfV\right), \text{ at } z = h, \tag{4.27}$$

where Eq. (2.9) has been used to express M in terms of V and μ is the ratio of V_s to V. Note that C_D and C_k do not enter separately, but only as a ratio. Since $V(r)$ is related to $p(r)$, Eq. (4.27) provides an additional constraint relating θ_e and $p(r)$. The other constraint is Eq. (4.19). In Region II, $rf << V$ so that the second term in parentheses on the right of Eq. (4.27) can be neglected compared with V^2 and the equation may be written as

$$\mu V^2 = \frac{C_k}{C_D}c_p(T_B - T_{out})(\ln\theta_{es}^* - \ln\theta_e), \text{ at } z = h. \tag{4.28}$$

Moreover, the *gradient wind equation* may be approximated as

$$V^2 \approx c_p T_B r\frac{\partial}{\partial r}\ln\pi. \tag{4.29}$$

Then θ_e may be eliminated between Eqs. (4.27) and (4.19) to yield an equation for pressure alone, which, in turn, through the gradient wind equation, determines the velocity profile at the top of the boundary layer. An alternative derivation of Eq. (4.28) will be in Section 4.5.

4.2 Region III

In Region III we would have to use Eq. (4.24) rather than Eq. (4.23), but we do not have an expression for w_h. Emanuel (1986) circumvented this problem and assumed that the combined effect of boundary-layer-induced subsidence and turbulent fluxes at the top of the boundary layer is to keep the relative humidity of the boundary layer at a relatively uniform level (typically about 80%). This allows one to obtain a second relationship between θ_e and $p(r)$ in Region III also. The derivation starts from the approximate formula for θ_e:

$$\ln \theta_e = \ln T - \ln \pi + \frac{Lq}{c_p T}. \tag{4.30}$$

With the assumption that T does not vary with radius ($= T_B$), and that θ_e is uniform through the depth of the boundary layer we obtain:

$$\ln \theta_e - \ln \theta_{ea} = -\ln \pi + \ln \pi_a + \frac{L}{c_p T_B}(q - q_a) \text{ at } z = h, \tag{4.31}$$

where a suffix "a" refers to ambient values. Now the hydrostatic equation may be written as $d\ln \pi/dz = g/(c_p T)$, whereupon

$$\ln \pi_{(z=h)} = \ln \pi_{(z=0)} + \int_0^h \frac{gdz}{c_p T},$$

and if T does not vary with radius, $\ln(\pi_s/\pi_h) = \ln(\pi_{sa}/\pi_{ha})$, where the suffix "s" refers to surface values. Then Eq. (4.31) becomes

$$\ln \frac{\theta_e}{\theta_{ea}} = -\ln \frac{\pi_s}{\pi_{sa}} + \frac{L}{c_p T_B}(q_s^* RH - q_{sa}^* RH_a). \tag{4.32}$$

Now $q \approx \epsilon e^*(T_B)/p$, whereupon $q^* = q_a^*(p_{sa}/p_s) = q_a^*(\pi_{sa}/\pi_s)^{1/\kappa} = \exp[(1/\kappa)(\pi_{sa}/\pi_s)]$. Then if $RH = RH_a$,

$$\ln \frac{\theta_e}{\theta_{ea}} = -\ln \frac{\pi_s}{\pi_{sa}} \left[1 + \frac{Lq_{as}^* RH_a}{RT_B} \right]. \tag{4.33}$$

This is the desired second relationship between θ_e and $p(r)$ in Region III, but note that it is obtained from thermodynamic considerations alone.

4.3 Region I and the complete solution

Emanuel *op. cit.* presents an analysis in an appendix to show that with the assumption that the eye is in solid body rotation, the M-surfaces and s^* surfaces approximately coincide and he uses this result to apply the relation (4.19) in Region I also. Moreover he assumes that (4.27) applies also in the boundary layer within

the eye. Then the radial variation of surface pressure can be obtained by solving the last two relationships in Regions I and II and Eqs. (4.19) and (4.33) in Region III and matching these solutions at the boundary between Regions II and III, which, as noted earlier, Emanuel takes to be at radius r_m. Then the gradient wind equation may be used to find the tangential wind speed at the top of the boundary layer. Finally the solution for the flow above the boundary layer may be obtained by evaluating quantities along angular momentum surfaces, whose shape is given by (4.12), which may be written as

$$\frac{1}{r^2}|_M = \frac{1}{M}\frac{ds^*}{dM}[T - T_{out}(s^*, p_{out})],$$

on the assumption that $r << r_{out}$. The reader is referred to Emanuel's paper for details of the calculations. Emanuel shows an example of a calculation for the following parameter values: $T_s = 27^oC$, $T_B = 22^oC$, $T_{out} = -67^oC$, f evaluated at 28° latitude, $p_o = 1015$ mb, $r_o = 400$ km, $C_\theta = C_D$, $RH_a = 80\%$, and $\gamma = 2$, corresponding to a Brunt-Väsälä frequency of 1.5×10^{-2}. Under these conditions the central pressure is 941 mb, the maximum tangential wind speed is 58 m s^{-1}, the radius of maximum winds is 36 km, and the ambient boundary layer θ_e is 349 K. The distributions of M, θ_e^*, V, and the temperature perturbation from the far environment at the same altitude are shown in Fig. 4.2. The solution captures the main observed features of a mature hurricane including the warm core at high altitude, the outward-sloping velocity maximum, and the strong radial gradient of θ_e^* near and inside the radius of maximum tangential wind speed.

Emanuel *op. cit.* estimated the streamfunction at the top of the boundary layer assuming that Eq. (4.23) gives the correct momentum balance in the boundary layer without considering turbulent fluxes at the top of the layer, even if the neglect of such fluxes yields an incorrect heat budget. Setting $\varphi_b = M$ in (4.23) and using (4.23) we can solve for the boundary-layer streamfunction, from which we can obtain the vertical velocity using $\rho r w_h = \partial\psi/\partial r$. The mean radial velocity in the boundary layer is given by $r\bar{u} = -\psi/(\bar{\rho}h)$, where h is the nominal depth of the layer and $\bar{\rho}$ is the mean density. The radial distributions of w_h and $\bar{u}$ for the vortex described above are shown in Fig. 4.3. These calculations are based on the assumptions that $\bar{\rho}$ and h are constants, with $h = 1$ km, and $C_D = 2 \times 10^{-3}$.

The vertical velocity profile in Fig. 4.3 shows a sharp peak at the radius of maximum tangential wind, but radial velocity reaches its maximum at a much larger radius. This is similar to the behaviour in the boundary-layer calculation shown in Fig. 3.1. Here, however, the streamfunction has a discontinuity at r_{max} as a consequence of matching two separate boundary layers there, since the radial gradient of angular momentum is discontinuous. This results in a jump in u and a delta function spike of vertical velocity at r_{max}. According to Emanuel, these unrealistic features would not be present had a single boundary layer representation been applied throughout the vortex. Note that w_h becomes negative beyond a radius of about 220 km, which is not consistent with the choice of r_o as 400 km.
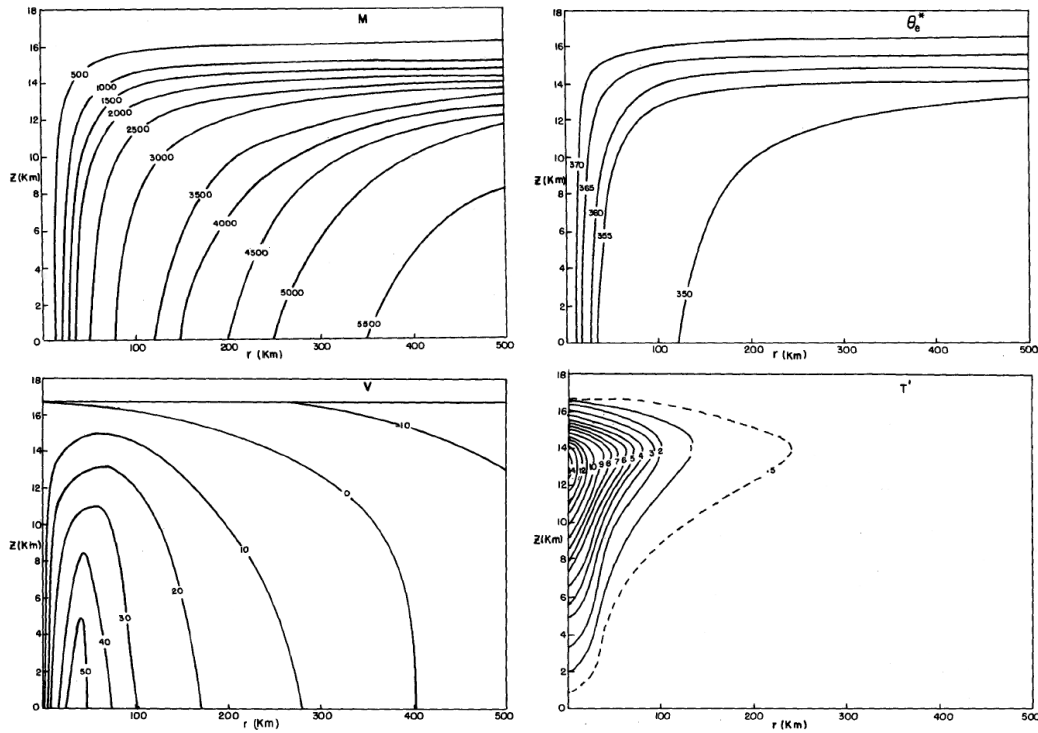
Figure 4.2: Distributions of: (a) absolute angular momentum (10^3 m^2 s^{-1}), (b) saturation equivalent potential temperature, (c) gradient wind (m s^{-1}), and (d) temperature departure (^{o}C) from the far environment at the same altitude, for the vortex discussed above. (From Emanuel 1986)

4.4 The tropical cyclone as a Carnot heat engine

Emanuel suggests that the steady tropical cyclone may be regarded as a simple Carnot heat engine in which air flowing inwards in the boundary layer acquires heat energy (mostly in latent form[2]) from the sea surface, ascends, and ultimately gives off heat at the much lower temperature of the upper troposphere or lower stratosphere. A schematic of this heat engine is shown in Fig. 4.4. Air begins to flow inwards at constant temperature along the lower boundary at radius r_o and acquires an incremental amount of heat

$$\Delta Q_1 = \int_{\theta_{ea}}^{\theta_e} c_p T_B d\ln\theta_e = c_p T_B \ln\left(\frac{\theta_e}{\theta_{ea}}\right), \qquad (4.34)$$

[2]When water evaporates from the ocean, it takes heat out of the ocean and this energy then resides in the water vapor content of the air. Because it does not immediately increase the temperature of the air, it is called latent heat. Ultimately, when the water vapor condenses inside clouds, the latent heat is converted to sensible heat and the temperature then actually increases somewhere in the system.
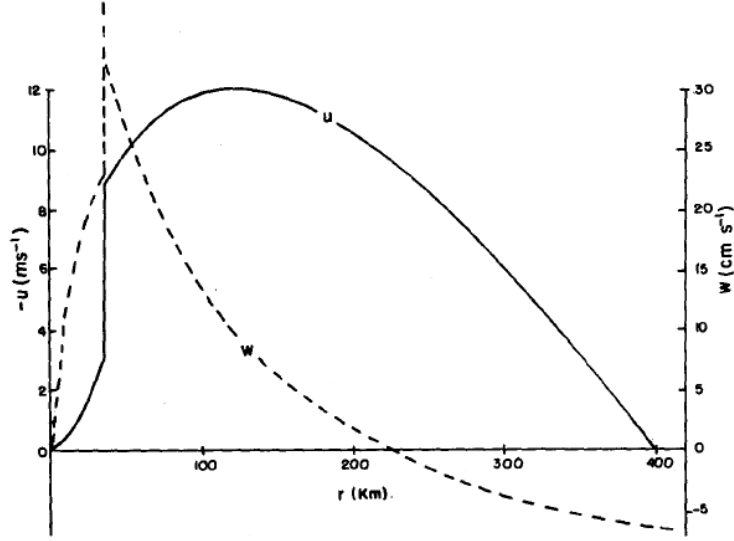
Figure 4.3: Radial distributions of vertical velocity (cm s^{-1}), and mean radial velocity (m s^{-1}) within the boundary layer for the vortex discussed above. (From Emanuel 1986)

where θ_{ea} is the equivalent potential temperature at r_o. The air ascends at constant entropy along an M surface and flows out to large radius. To complete the circuit, the air eventually loses enough total heat through radiative cooling to return to its ambient θ_e so that

$$\Delta Q_2 = \int_{\theta_e}^{\theta_{ea}} c_p \bar{T}_{out} d \ln \theta_e = -c_p T_{out} \ln \left(\frac{\theta_e}{\theta_{ea}} \right), \qquad (4.35)$$

where $\bar{T}_{out}$ is given by (4.18). The total heating, from (4.34) and (4.35), is therefore

$$\Delta Q = \Delta Q_1 + \Delta Q_2 = c_p T_B \epsilon \ln \left(\frac{\theta_e}{\theta_{ea}} \right), \qquad (4.36)$$

where $\varepsilon = (T_B - \bar{T}_{out})/T_B$ is the thermodynamic efficiency. This net heating is used to do work against frictional dissipation in the steady tropical cyclone. Referring to Fig. 4.4, it is seen that work is done against friction in the inflowing boundary-layer air and also to change the angular momentum back to its ambient value at large radii in the outflow. Kinetic energy is also dissipated by turbulence within cumulus clouds; however, Emanuel argues that this sink primarily balances kinetic energy generated by release of the ambient convective available potential energy as is probably the case in the unperturbed tropical atmosphere. This is simply a statement that convective clouds in tropical cyclones are locally similar to those away from such disturbances. The balance between total heating and frictional dissipation in the inflow and outflow may be written symbolically as

$$\Delta Q = W_{PBL} + W_o, \qquad (4.37)$$

where W_{PBL}, and W_o are the work done in the boundary layer and outflow, respectively. The latter is simply proportional to the change in kinetic energy needed to bring the angular momentum of the outflow, M, back to its ambient value M_o:
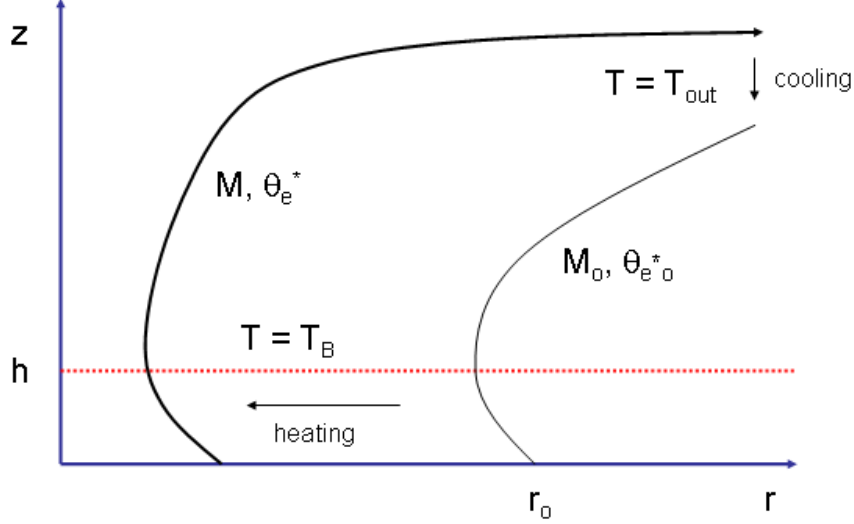
Figure 4.4: The tropical cyclone as a Carnot heat engine.

$$
\begin{aligned}
W_0 &= \frac{1}{2}\Delta V^2 = \frac{1}{2}\left[\left(\frac{M}{r_1} - \frac{1}{2}fr_1\right)^2 - \left(\frac{M_0}{r_1} - \frac{1}{2}fr_1\right)^2\right] \\
&= \frac{1}{2}\left[\frac{M^2 - M_0^2}{r_1^2} + f\left(M_0 - M\right)\right],
\end{aligned} \tag{4.38}
$$

where we have related azimuthal velocity to angular momentum using (1) and r_1 is some large radius at which the exchange takes place. In the limit of large r_1,

$$
\lim_{r_1 \to 0} W_0 = \frac{1}{2}f(M_0 - M) = \frac{1}{4}f^2(r_0^2 - r^2) - \frac{1}{2}frV. \tag{4.39}
$$

Using the above (4.36) and (4.37) we infer the work done in the boundary layer:

$$
W_{PBL} = C_P T_B \varepsilon \ln \frac{\theta_e}{\theta_{ea}} + \frac{1}{2}frV - \frac{1}{4}f^2\left(r_0^2 - r^2\right). \tag{4.40}
$$

Finally, knowledge of the work done against dissipation in the boundary layer allows an evaluation of the pressure distribution in the boundary layer through the use of Bernoulli's equation. The latter, when integrated inward from r_0 at constant temperature, may be written

$$
\frac{1}{2}V^2 + C_P T_B \varepsilon \ln \pi + W_{PBL} = 0 \quad \text{at} \quad z = 0. \tag{4.41}
$$

When (4.40) is substituted into this and the gradient wind equation is used for the sum $V^2 + frV$, the result is

$$\ln \pi + \frac{1}{2} r \frac{\partial \ln \pi}{\partial r} + \varepsilon \ln \frac{\theta_e}{\theta_{ea}} - \frac{1}{4} \frac{f^2}{C_p T_B}(r_0^2 - r^2) = 0 \quad \text{at} \quad z = 0, \qquad (4.42)$$

which is identical to (4.19). This confirms the interpretation of the results of the previous section in terms of a Carnot engine.

4.5 The potential intensity of tropical cyclones

As we have seen, tropical cyclones derive their energy from the thermodynamic disequilibrium that exists between the tropical oceans and the overlying atmosphere. By taking into account both the rate and the efficiency with which this reservoir of heat energy can be converted into wind energy it is possible to derive a speed limit for hurricanes, which depends mostly on ocean and atmospheric temperatures. In nature, interaction of tropical cyclones with their atmospheric and oceanic environment limits the intensity of most (but not all) storms to values well below the theoretical limit. Nevertheless, limit theory is useful for estimating the most intense storm likely to strike a given area over a reasonably long period of time.

Emanuel (1986, 1995) described a method of estimating upper bounds on tropical cyclone intensity that uses the energy cycle of the storm to estimate the maximum possible surface wind speed. The central pressure can be estimated also by assuming a particular radial profile of azimuthal wind inside the eye.
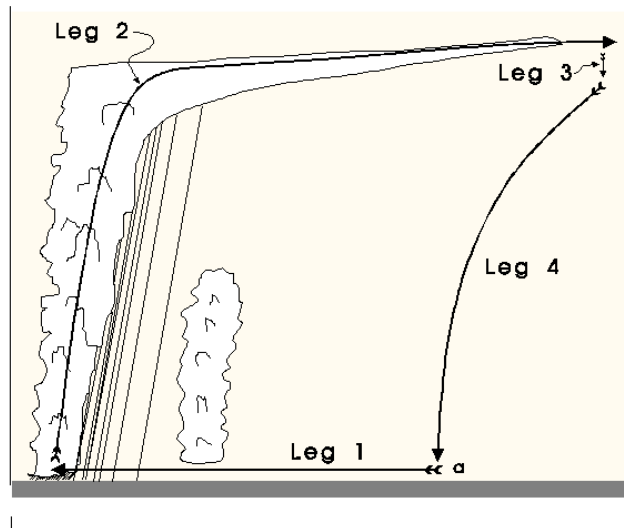

Figure 4.5: For discussion see text. (From Emanuel

The energy cycle is illustrated in Fig. 4.5. Air spirals in toward the storm center and, owing to the large surface wind speeds, rapidly acquires heat from the underlying

ocean. This additional heat shows up mostly as an increase in the humidity, rather than the temperature, of the air. The total increase in heat content on this leg is proportional to the increase in water vapor content and the decrease in pressure; this latter effect is called "heat input by isothermal expansion."

Once the air reaches the eyewall, it turns upward and quickly rises through the eyewall to around 15-18 km altitude, where it then flows outward. The ascent is nearly adiabatic; that is, no net heat is added in this leg, though there are large conversions of latent to sensible heat. The heat is exported to the storm's environment and ultimately lost by radiation to space.

Only a fraction of the heat put into the heat engine is available for generation of wind energy. This fraction is called the thermodynamic efficiency, ϵ, and is defined by

$$\epsilon = \frac{T_s - T_{out}}{T_{out}}, \tag{4.43}$$

where T_s is the temperature of the heat source (in this case, the ocean surface) and T_{out} is the average temperature at which heat is exported from the system, both measured in Kelvin). The taller a hurricane is, the lower the temperature at its top and thus, from (4.43), the greater the thermodynamic efficiency. Moreover, if we know how much heat air has in the eyewall and we know the vertical temperature structure of the air in the environment of the storm, then we can calculate how high air will rise in the eyewall and thus we can calculate T_{out}. Note that T_{out} is just the temperature of the environment corresponding with the level of neutral buoyancy of air with equivalent potential temperature θ_{eb} when lifted from height $z = h$. This temperature, together with sea surface temperature, gives us ϵ, from (4.43). In a typical hurricane, ϵ is about $1/3$.

The rate of input of available energy, into the hurricane from the sea surface, for each square metre of sea surface covered by the storm, is given by

$$G = \epsilon C_k \rho V_s (k_s^* - k_b), \tag{4.44}$$

where G stands for "generation", C_k is a dimensionless coefficient called the enthalpy transfer coefficient and k_s^* and k_b are the enthalpies of the ocean surface and the atmosphere near the surface, respectively (compare with Eq. (4.26)). To obtain the entire energy input, it is necessary to sum the contributions given by (4.44) over the area of the ocean surface affected by the storm. Emanuel assumes that this sum is dominated by the contribution near the radius of maximum wind, where V_s is large.

What happens to all this energy that is generated by heat transfer from the sea surface? When the storm has reached a nearly steady condition (on which its intensity is no longer changing), almost all of the energy generated is used up by friction acting between the powerful winds and the sea surface. The rate of mechanical dissipation in the system, for each square meter of ocean surface, is given by

$$D = C_D \rho V_s^3, \tag{4.45}$$

where D stands for "dissipation" and the other symbols are the same as in (4.44), but C_D is a different coefficient, called the drag coefficient. Once again, it is necessary to sum (4.45) over each square metre of ocean surface affected by the storm, but we will assume again that it is dominated by the contributions near the radius of maximum wind.

Equating generation, given by (4.44), to dissipation, given by (4.45), gives an expression for the wind speed:

$$V_m^2 = \frac{C_k}{C_D}\epsilon T_s(k_s^* - k_b)_m, \tag{4.46}$$

where the subscript "m" reminds us that we should evaluate the quantities near the radius of maximum wind.

It is important to note here that (4.46) can be derived much more rigorously than has been done here and that when this is done, it turns out that given by (4.46) is indeed an expression for the maximum surface wind speed (see Bister and Emanuel, 1998). It is also important to recognize that the derivation of (4.46) depends in no way on what happens inside the eye of the storm.

To actually evaluate (4.46), it is necessary to know several things. First, we have to know the ratio of heat to momentum exchange coefficients, C_k/C_D. Unfortunately, no measurements of either of these coefficients have been made at hurricane wind speeds. For now, it is assumed that this ratio is 1. Another thing we have to know is the saturation enthalpy of the ocean surface, k_s^*. This depends mostly on sea surface temperature, but also on sea level pressure at the radius of maximum winds. To get this, it is necessary to assume something about the distribution of wind outside the radius of maximum winds. The calculation of k_s^* is not terribly sensitive to what one assumes about this distribution, as long as it is reasonable. One also has to estimate the enthalpy of the air just above the sea surface, k_b, at the radius of maximum winds. This must be at least as large as the entropy of unperturbed boundary layer air, and it depends on temperature, pressure, and relative humidity. Emanuel (1995) assumes that the air temperature is closely linked to the sea surface temperature, a fact that is supported by the boundary-layer calculation in Section 3. He assumes also that the relative humidity is the same as that of the unperturbed environment (usually around 75-80%). Finally, one has to estimate ϵ. To do this, one has to first estimate T_{out}, the temperature at which air flows out of the top of the storm; this is also equivalent to estimating the altitude of the storm top. This accomplished by finding out how high up in the eyewall the air remains warmer than the distant environment, and is straightforward to assess given the vertical profile of temperature in the storm environment.

Storm intensity is also often measured by its central pressure. One method of getting the central pressure is to first assume that the eye is in "solid body rotation," i.e., that the swirling wind increases linearly with radius out to the radius of maximum wind. Taking the wind field to be balanced by the radial pressure gradient is an excellent approximation in the hurricane eye, and so one can easily calculate

the central pressure given the pressure at the radius of maximum winds and the maximum wind speed, both of which we know from the aforementioned reasoning. This gives

$$p_c = p_m exp(-V_m^2/2R_d T_s), \tag{4.47}$$

where R_d is the gas constant for air.
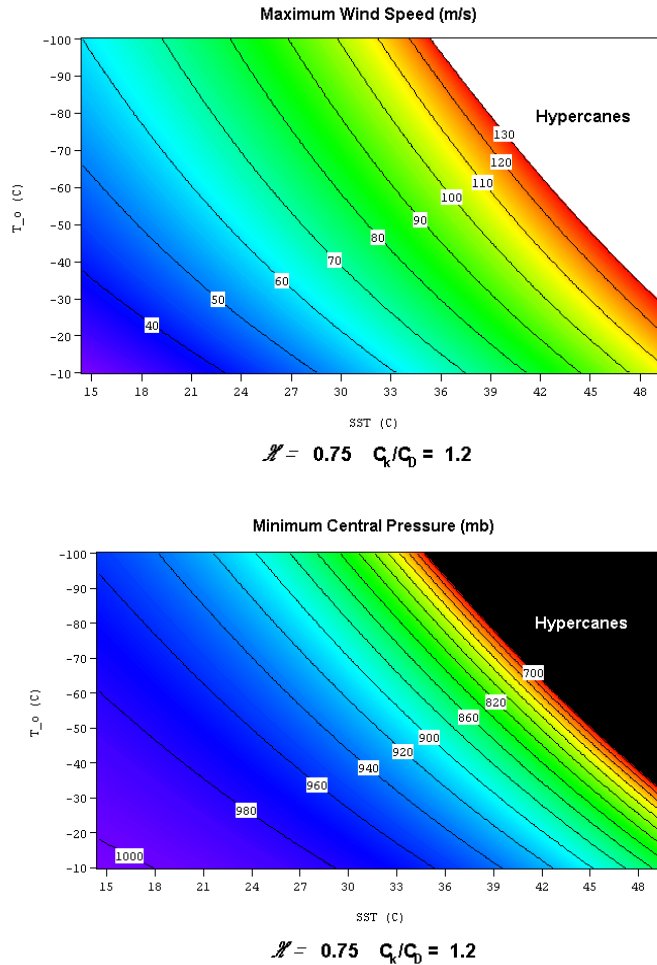
Figure 4.6: For discussion see text. (From Emanuel)

To gain an idea of how the storm intensity depends on sea surface and storm outflow temperature, examine Fig. 4.6a and Fig. 4.6b, which use (4.46) and (4.47) to calculate p_c and V_m given ocean temperature and T_0, and assuming that the relative humidity under the eyewall is 75%. Both measures show intensity increasing with sea surface temperature, and the rate of increase also gets steeper at higher sea surface temperature. Note also that at very high sea surface temperature and low outflow temperature, there are no solutions to the equations. This is the "hypercane"

regime. Numerical simulations in this regime produce very intense storms (with wind speeds near the speed of sound), and it has been speculated that such storms may have formed over pools of very hot water created by large asteroid impacts with the ocean. But we do not have to worry about hypercanes otherwise!
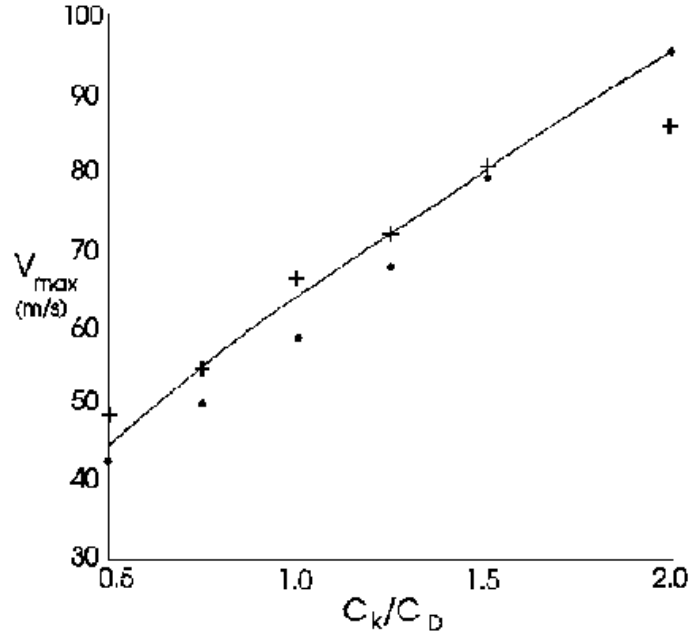
Figure 4.7: For discussion see text. (From Emanuel)

One prediction of the form of limiting theory presented here is that the intensity of tropical cyclones should depend on the ratio of surface exchange coefficients, C_k/C_D (see Eq. 4.46). As mentioned above, we do not know very well what this is in nature, but we are free to specify it in computer models of hurricanes. Figure 4.7 shows the results of running two quite different computer models and comparing the results with the theory (see Emanuel, 1995, for details). As predicted, the storm intensity does increase with C_k/C_D.

To solve the foregoing equations, one can write (4.46) in the form

$$V_m^2 = \frac{C_k}{C_D}\frac{T_s}{T_{out}}T_s - T_{out}(s_{ps}^* - s_{pb})_m, \tag{4.48}$$

where s_{ps}^* and s_{pb} are the pseudo-saturation entropies. Since both these quantities are constant, Eq. (4.48) may be written as

$$V_m^2 = \frac{C_k}{C_D}\frac{T_s}{T_{out}}\int_{T_{out}}^{T_s}(s_{ps}^* - s_{pb})_m dT. \tag{4.49}$$

or

$$V_m^2 = \frac{C_k}{C_D}\frac{T_s}{T_{out}}\int_{T_{out}}^{T_s}[(s_{ps}^* - s_{pa}^*) - (s_{pb} - s_{pa}^*)]dT\,. \tag{4.50}$$

which, from Eq. (10.12) is approximately

$$V_m^2 = \frac{C_k}{C_D}\frac{T_s}{T_{out}}(CAPE^* - CAPE)_m\,, \tag{4.51}$$

where $CAPE^*$ is the convective available potential energy of air lifted from saturation at sea level in reference to the environmental sounding, and $CAPE$ is that of boundary layer air (see section 4.6). Both quantities are evaluated near the radius of maximum wind. To evaluate (4.50) it is necessary to determine the surface pressure at the radius of maximum winds, needed to calculate the saturation mixing ratio necessary for $CAPE^*$. To do so, we use Eq. (4.16), which represents a combination of gradient wind balance and thermal wind balance in the outer region of the hurricane. Since $s^* = c_p \ln \theta_e^*$, this equation may be written as

$$-[T_B - T_{out}(s^*, p_{out})]\frac{\partial s^*}{\partial r} = c_p T_s\left[\frac{\partial \ln \pi}{\partial r} + \frac{1}{2}\frac{\partial}{\partial r}\left(r\frac{\partial \ln \pi}{\partial r}\right)\right] + \frac{1}{2}rf^2,\ \text{at}\ z = h. \tag{4.52}$$

Integrating with respect to radius then gives

$$-\int_{r_0}^{r_m}[T_B - T_{out}(s^*, p_{out})]\frac{\partial s^*}{\partial r}dr = c_p T_s\left[\ln\frac{\pi_m}{\pi_0} + \frac{1}{2}\left(r\frac{\partial \ln \pi}{\partial r}\right)_m - \frac{1}{2}\left(r\frac{\partial \ln \pi}{\partial r}\right)_0\right]$$

$$+\frac{1}{4}f^2(r_m^2 - r_0^2),\ \text{at}\ z = h. \tag{4.53}$$

The left-hand-side of this equation is

$$\int_{s_*^m}^{s_0^*}[T_B - T_{out}(s^*, p_{out})]ds^* \tag{4.54}$$

and we show in an appendix (section 4.6) that this is equal to $CAPE_m$. The first term in brackets on the right-hand-side is equal to $RT_s \ln(p_0/p_m)$, where p_0 is the ambient surface pressure and p_m is the surface pressure at the radius of maximum winds. Using the gradient-wind equation in the form

$$\frac{V^2}{r} + fV = c_p T_s\frac{\partial}{\partial r}\ln \pi\,,$$

the second and third terms in brackets on the right-hand-side are approximately equal to $\frac{1}{2}(V_m^2 - fV_0 r_0)$, assuming that the flow is cyclostrophic at $r = r_m$ and geostrophic at $r = r_0$. The term $\frac{1}{4}f^2 r_m^2$ is also $<< \frac{1}{2}V_m^2$. Furthermore, the term $\frac{1}{2}fV_0 r_0$ is smaller in magnitude than $\frac{1}{4}f^2 r_m^2$. Thus Eq. (4.53) becomes

$$RT_s \ln\frac{p_0}{p_m} = \tfrac{1}{2}V_m^2 - CAPE_m - \tfrac{1}{4}f^2 r_o^2. \tag{4.55}$$

This is the desired relationship for p_m.

To calculate $CAPE_m$, the mixing ratio and temperature of the boundary layer under the eyewall is needed. Following Emanuel (1995a), we assume that the surface temperature is T_s and that the relative humidity is constant from the outer region to the outer edge of the eyewall. Since the pressure under the eyewall is lower than ambient, this entails a small inward increase in mixing ratio. For this reason, $CAPE_m$ is a little larger than the $CAPE$ of ambient boundary layer air. Emanuel claims that the assumption of constant relative humidity in the outer region boundary layer is well supported by numerical simulations. Given a value of C_k/C_D, the sea surface temperature, and an ambient profile of virtual temperature, (4.51) and (4.52) constitute closed relations for V_m and p_m. $CAPE$ is calculated by a reversible adiabatic parcel lifting algorithm. Owing to the pressure dependence of $CAPE_m^*$ and $CAPE_m$, (4.51) and (4.52) must be solved iteratively. This always converges unless one is in the "hypercane" regime.

4.6 Appendix to Chapter 4

4.6.1 Evaluation of the integral in Eq. (4.49)
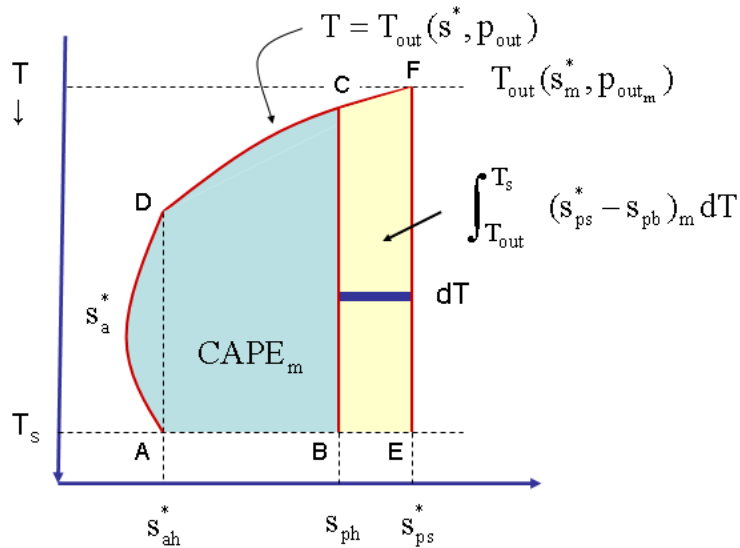
Figure 4.8: The integral in Eq. (4.49) represents the area BCFE in the figure - see text.

The integral in Eq. (4.49) represents the area BCFE in the Fig. 4.8. This area is equal to the area AEFD - ABCD. The area AEFD is approximately equal to the $CAPE$ of an air parcel lifted from saturation at the sea surface temperature, while the area ABCD is the $CAPE$ of a parcel lifted from the top of the boundary layer

(see section 10.1.2). The integral in Eq. (4.54) represents the shaded area shown in the Fig. 4.9. The area AEFD is approximately equal to the $CAPE$ of an air parcel lifted from the top of the boundary layer.
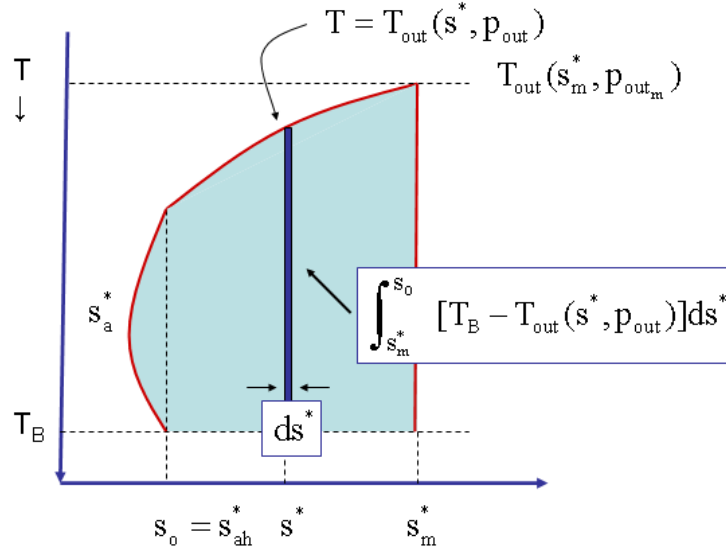
Figure 4.9: The integral in Eq. (4.54) represents the shaded area shown in the figure - see text.

Chapter 5

TROPICAL CYCLONE MOTION

The prediction of tropical cyclone motion has improved dramatically during the last decade as has our understanding of the mechanisms involved. Some of the basic aspects of tropical cyclone motion can be illustrated in terms of barotropic theory, which assumes that the vortex structure is independent of height. We begin first by examining this theory and go on in a following section to examine baroclinic aspects of motion.

5.1   Vorticity-streamfunction method

The vorticity-streamfunction method is a powerful way of solving two-dimensional flow problems for a homogeneous, incompressible fluid. It is conventional to choose a rectangular coordinate system (x, y), with x pointing eastwards and y pointing northwards. For two-dimensional motion in the x-y-plane, the relative vorticity, ζ, is defined as $\partial v/\partial x - \partial u/\partial y$ and satisfies the equation

$$\frac{\partial}{\partial t}(\zeta + f) + u\frac{\partial}{\partial x}(\zeta + f) + v\frac{\partial}{\partial y}(\zeta + f) = 0, \tag{5.1}$$

where u and v are the velocity components in the x and y directions, respectively.

For an incompressible fluid, the continuity equation is

$$\frac{\partial u}{\partial x} + \frac{\partial v}{\partial x} = 0, \tag{5.2}$$

and accordingly there exists a streamfunction ψ such that

$$u = -\frac{\partial \psi}{\partial y}, \quad v = \frac{\partial \psi}{\partial x}, \tag{5.3}$$

and

$$\zeta = \frac{\partial^2 \psi}{\partial x^2} + \frac{\partial^2 \psi}{\partial y^2}, \tag{5.4}$$

Equation (5.1) is a prediction equation for the *absolute vorticity*, $\zeta + f$, and states that this quantity is conserved following columns[1] of fluid. Equation (5.4) can be used as an expression for calculating ζ if ψ is known, or, alternatively, as an elliptic second-order partial differential equation for ψ if ζ is known. When ψ is known, u and v can be calculated from the expressions (5.3).

In a few simple cases it may be possible to obtain an analytic solution of Eqs. (5.1), (5.3) and (5.4), but in general we must resort to numerical methods. The system of equations can be solved numerically using the following steps:

- From a given initial distribution of ψ at, say $t = 0$, we can calculate the initial velocity distribution from Eq. (5.3) and the initial vorticity distribution from Eq, (5.4). Alternatively, given the initial vorticity distribution, we can solve Eq. (5.4) for the initial streamfunction distribution ψ and then calculate the initial velocity distribution from Eq. (5.3).

- We are now in a position to predict the vorticity distribution at a later time, say $t = \Delta t$, using Eq. (5.1).

- Then we can solve Eq. (5.4) for the streamfunction distribution ψ at time Δt and the new velocity distribution from Eq. (5.3).

- We now repeat this procedure to extend the solution forward to the time $t = 2\Delta t$, and so on.

5.2 The partitioning problem

An important issue that arises in the study of tropical cyclone motion is the so-called partitioning problem, i.e. the problem of deciding what is the cyclone and what is its environment. Of course, Nature makes no distinction so that any partitioning that we make to enable us to discuss the interaction between the tropical cyclone and its environment is necessarily non-unique.

Various methods have been proposed to isolate the cyclone from its environment and each may have their merits in different applications. One obvious possibility is to define the cyclone as the azimuthally-averaged flow about the vortex centre, and the residual flow (i.e. the asymmetric component) as "the environment". But then the question arises: which centre? We show below that, in general, the location of the minimum surface pressure and the centre of the vortex circulation at any level are not coincident. The pros and cons of various methods are discussed by Kasahara and Platzman (1963) and Smith *et al.* (1990). Many theoretical studies consider the motion of an initially symmetric vortex in some analytically-prescribed environmental flow. If the flow is assumed to be barotropic, there is no mechanism

---

[1]In a two-dimensional flow, there is no dependence of u, v, or ζ on the z-coordinate and we can think of the motion of thin columns of fluid of uniform finite depth, or infinite depth, analogous to fluid parcels in a three-dimensional flow.

to change the vorticity of air columns. In this case it is advantageous to define the vortex to be the *initial* relative vorticity distribution, appropriately relocated, in which case all the flow change accompanying the vortex motion resides in the residual flow that is considered to be the vortex environment. We choose also the position of the relative vorticity maximum as the 'appropriate location' for the vortex. An advantage of this method (essentially Kasahara and Platzman's method III) is that all the subsequent flow changes are contained in one component of the partition and the vortex remains "well-behaved" at large radial distances. Further, one does not have to be concerned with vorticity transfer between the symmetric vortex and the environment as this is zero, by definition. The method has advantages also for understanding the motion of initially asymmetric vortices as discussed by Smith *et al.* (1990) and in Section 4.1.

The partitioning method can be illustrated mathematically as follows. Let the total wind be expressed as $\mathbf{u} = \mathbf{u_s} + \mathbf{U}$, where $\mathbf{u_s}$ denotes the symmetric velocity field and $\mathbf{U}$ is the vortex environment vorticity, and define $\zeta_s = \mathbf{k} \cdot \nabla \wedge \mathbf{u_s}$ and $\Gamma = \mathbf{k} \cdot \nabla \wedge \mathbf{U}$, where $\mathbf{k}$ is the unit vector in the vertical. Then Eq. (5.1) can be partitioned into two equations:

$$\frac{\partial \zeta_s}{\partial t} + \mathbf{c}(t) \cdot \nabla \zeta_s = 0, \tag{5.5}$$

and

$$\frac{\partial \Gamma}{\partial t} = -\mathbf{u_s} \cdot \nabla(\Gamma + f) - (\mathbf{U} - \mathbf{c}) \cdot \nabla \zeta_s - \mathbf{U} \cdot \nabla(\Gamma + f), \tag{5.6}$$

noting that $\mathbf{u_s} \cdot \nabla \zeta_s = 0$, because for a symmetric vortex $\mathbf{u_s}$ is normal to $\nabla \zeta_s$. Equation (5.5) states that the symmetric vortex translates with speed $\mathbf{c}$ and Eq. (5.6) is an equation for the evolution of the asymmetric vorticity. Having solved the latter equation for $\Gamma(\mathbf{x}, t)$, we can obtain the corresponding asymmetric streamfunction by solving Eq. (5.4) in the form $\nabla^2 \psi_a = \Gamma$. The vortex translation velocity $\mathbf{c}$ may be obtained by calculating the speed $\mathbf{U_c} = \mathbf{k} \wedge \nabla \psi_a$ at the vortex centre. In some situations it is advantageous to transform the equations of motion into a frame of reference moving with the vortex[2]. Then Eq. (5.5) becomes $\partial \zeta_s / \partial t \equiv 0$ and the vorticity equation (5.6) becomes

$$\frac{\partial \Gamma}{\partial t} = -\mathbf{u_s} \cdot \nabla(\Gamma + f) - (\mathbf{U} - \mathbf{c}) \cdot \nabla \zeta_s - (\mathbf{U} - \mathbf{c}) \cdot \nabla(\Gamma + f). \tag{5.7}$$

5.3 Prototype problems

5.3.1 Symmetric vortex in a uniform flow

Consider a barotropic vortex with an axisymmetric vorticity distribution embedded in a uniform zonal air stream on an f-plane. The streamfunction for the flow has the

---

[2]See Appendix 9.1 for details.

form:

$$\psi(x, y) = -Uy + \psi'(r), \tag{5.8}$$

where $r^2 = (x - Ut)^2 + y^2$. The corresponding velocity field is

$$\mathbf{u} = (U, 0) + \left(-\frac{\partial \psi'}{\partial y}, \frac{\partial \psi'}{\partial x} \right), \tag{5.9}$$

The relative vorticity distribution, $\zeta = \nabla^2 \psi$, is symmetric about the point $(x - Ut, 0)$, which translates with speed U in the x-direction. However, neither the streamfunction distribution $\psi(x, y, t)$, nor the pressure distribution $p(x, y, t)$, are symmetric and, in general, the locations of the minimum central pressure, maximum relative vorticity, and minimum streamfunction (where $\mathbf{u} = \mathbf{0}$) do not coincide. In particular, there are three important deductions from (5.9):

- The total velocity field of the translating vortex is not symmetric, and

- The maximum wind speed is simply the arithmetic sum of U and the maximum tangential wind speed of the symmetric vortex, $V_m = (\partial \psi'/\partial r)_{max}$.

- The maximum wind speed occurs on the right-hand-side of the vortex in the direction of motion in the northern hemisphere and on the left-hand-side in the southern hemisphere.

Figure 5.1 shows an example of the vorticity, streamfunction and wind speed distribution for the tropical-cyclone-scale vortex in Fig. 5.6, translating in a uniform westerly current of 10 m s^{-1}. The maximum tangential velocity is 40 m s^{-1} at a radius of 100 km.

Because the vorticity field is Galilean invariant while the pressure field and streamfunction fields are not, it is advantageous to define the vortex centre as the location of maximum relative vorticity and to transform the equations of motion to a coordinate system $(X, Y) = (x - Ut, y)$, whose origin is at this centre[3]. In this frame of reference, the streamfunction centre is at the point $(0, Y_s)$, where

$$U - \Phi(Y_s)Y_s = 0, \tag{5.10}$$

and $\Phi = \psi'(r)/r$. This point is to the left of the vorticity centre in the direction of motion in the northern hemisphere. In the moving coordinate system, the momentum equations may be written in the form

$$\nabla p = \rho \Phi(\Phi + f)(X, Y) + \rho f(0, U). \tag{5.11}$$

The minimum surface pressure occurs where $\nabla p = 0$, which from (5.11) is at the point $(0, Y_p)$ where

$$Y_p \Phi(Y_p)(\Phi(Y_p) + f) = fU. \tag{5.12}$$

---

[3]The transformation of the equations of motion to a moving coordinate system is derived in Appendix 9.1.
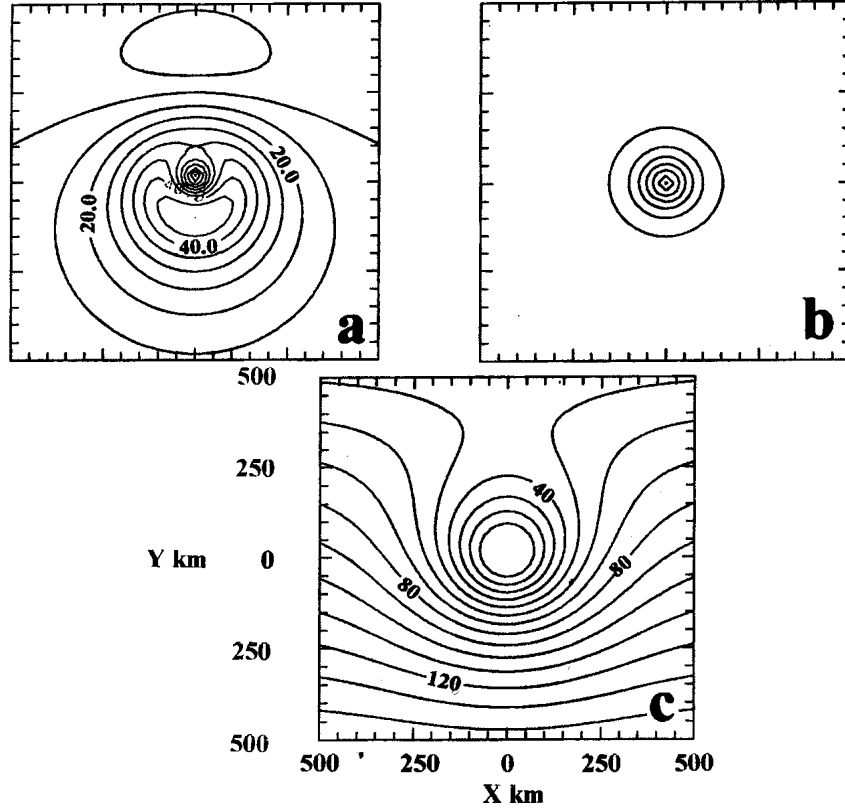
Figure 5.1: Contour plots of (a) total wind speed, (b) relative vorticity, and (c) streamlines, for a vortex with a symmetric relative vorticity distribution and maximum tangential wind speed of 40 m s^{-1} in a uniform zonal flow with speed 10 m s^{-1} on an f-plane. The maximum tangential wind speed occurs at a radius of 100 km (for the purpose of illustration). The contour intervals are: 5 m s^{-1} for wind speed, 2×10^{-4} s^{-1} for relative vorticity and 1×10^4 m^2 s^{-1} for streamfunction.

We show that, although Y_p and Y_s are not zero and not equal, they are for practical purposes relatively small.

Consider the case where the inner core is in solid body rotation out to the radius r_m, of maximum tangential wind speed v_m, with uniform angular velocity $\Omega = v_m/r_m$. Then $\psi'(r) = \Omega r$ and $\Phi = \Omega$. It follows readily that $Y_s/r_m = U/v_m$ and $Y_p/r_m = U/(v_m Ro_m)$, where $Ro_m = v_m/(r_m f)$ is the Rossby number of the vortex core which is large compared with unity in a tropical cyclone. Taking typical values: $f = 5 \times 10^{-5}$ s^{-1}, $U = 10$ m s^{-1}, $v_m = 50$ m s^{-1}, $r_m = 50$ km, $Ro_m = 20$ and $Y_s = 10$ km, $Y_p = 0.5$ km, the latter being much smaller than r_m. Clearly, for weaker vortices (smaller v_m) and/or stronger basic flows (larger U), the values of Y_s/r_m and Y_p/r_m are comparatively larger and the difference between the various centres may be significant.

5.3.2 Vortex motion on a beta-plane

Another prototype problem for tropical-cyclone motion considers the evolution of an initially-symmetric barotropic vortex on a Northern Hemisphere β-plane in a quiescent environment. The problem was investigated by a number of authors in the late 80s using numerical models (Chan and Williams, 1987; Fiorino and Elsberry 1989; Smith *et al.* 1990; Shapiro and Ooyama 1990) and an approximate analytic solution was obtained by Smith and Ulrich (1990). In this problem, the initial absolute vorticity distribution, $\zeta + f$ is not symmetric about the vortex centre: a fluid parcel at a distance y_o poleward of the vortex centre will have a larger absolute vorticity than one at the same distance equatorward of the centre. Now Eq. (5.1) tells us that $\zeta + f$ is conserved following fluid parcels and initially at least these will move in circular trajectories about the centre. Clearly all parcels initially west of the vortex centre will move equatorwards while those initially on the eastward side will move polewards. Since the planetary vorticity decreases for parcels moving equatorwards, their relative vorticity must increase and conversely for parcels moving polewards. Thus we expect to find a cyclonic vorticity anomaly to the west of the vortex and an anticyclonic anomaly to the east.
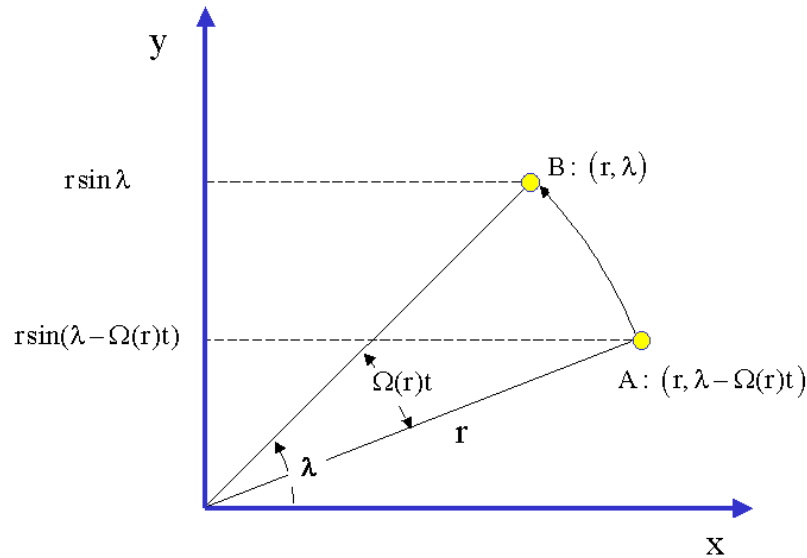
Figure 5.2: An air parcel moving in a circular orbit of radius r with angular velocity $\Omega(r)$ is located at the point B with polar coordinates (r, λ) at time t. At time $t = 0$ the parcel was located at point A with coordinates $(r, \lambda - \Omega(r)t)$. During this time it undergoes a meridional displacement $r[\sin \lambda - \sin(\lambda - \Omega(r)t)]$.

To a first approximation we can determine the evolution of the vorticity asymmetries by assuming that the flow about the vortex motion remains circular relative to the moving vortex (we discuss the reason for the vortex movement below). Consider an air parcel that at time t is at the point with polar coordinate (r, λ) located at

the (moving) vortex centre (Fig. 5.2). This parcel would have been at the position $(r, \lambda - \Omega(r)t)$ at the initial instant, where $\Omega(r) = V(r)/r$ is the angular velocity at radius r and $V(r)$ is the tangential wind speed at that radius. The initial vorticity of the parcel is $\zeta_s(r) + f_0 + \beta r \sin(\lambda - \Omega(r)t)$ while the vorticity of a parcel at its current location is $\zeta(r) + f_0 + \beta r \sin \lambda$. Therefore the vorticity perturbation $\zeta_a(r, \lambda)$ at the point (r, λ) at time t is $\zeta(r) - \zeta_s(r)$, or

$$\zeta_a(r, \lambda) = \beta r [\sin \lambda - \sin(\lambda - \Omega(r)t)]$$

or

$$\zeta_a(r, \lambda) = \zeta_1(r, t) \cos \lambda + \zeta_2(r, t) \sin \lambda, \tag{5.13}$$

where

$$\zeta_1(r, t) = -\beta r \sin(\Omega(r)t), \quad \zeta_2(r, t) = -\beta r [1 - \cos(\Omega(r)t)]. \tag{5.14}$$

We can now calculate the asymmetric streamfunction $\psi_a(r, \lambda, t)$ corresponding to this asymmetry using Eq. (5.4). The solution should satisfy the boundary condition that $\psi \to 0$ as $r \to \infty$. It is reasonable to expect that ψ_a will have the form:

$$\psi_a(r, \lambda) = \Psi_1(r, t) \cos \lambda + \Psi_2(r, t) \sin \lambda, \tag{5.15}$$

and it is shown in Appendix 3.4.1 that

$$\Psi_n(r, t) = -\frac{r}{2} \int_r^\infty \zeta_n(p, t) \, dp - \frac{1}{2r} \int_0^r p^2 \zeta_n(p, t) \, dp \quad (n = 1, 2), \tag{5.16}$$

The Cartesian velocity components $(U_a, V_a) = (-\partial \Psi_a/\partial y, \partial \Psi_a/\partial x)$ are given by

$$U_a = \cos \lambda \sin \lambda \left[\frac{\Psi_1}{r} - \frac{\partial \Psi_1}{\partial r} \right] - \sin^2 \lambda \frac{\partial \Psi_2}{\partial r} - \cos^2 \lambda \frac{\Psi_2}{r}, \tag{5.17}$$

$$V_a = \cos^2 \lambda \frac{\partial \Psi_1}{\partial r} + \sin^2 \lambda \frac{\Psi_1}{r} - \cos \lambda \sin \lambda \left[\frac{\Psi_2}{r} - \frac{\partial \Psi_2}{\partial r} \right]. \tag{5.18}$$

In order that these expressions give a unique velocity at the origin, they must be independent of λ as $r \to 0$, in which case

$$\left. \frac{\partial \Psi_n}{\partial r} \right|_{r=0} = \lim_{r \to 0} \frac{\Psi_n}{r}, \quad (n = 1, 2).$$

Then

$$(U_a, V_a)_{r=0} = \left[-\left. \frac{\partial \Psi_2}{\partial r} \right|_{r=0}, \left. \frac{\partial \Psi_1}{\partial r} \right|_{r=0} \right], \tag{5.19}$$

and using (5.16) it follows that

$$\left. \frac{\partial \Psi_n}{\partial r} \right|_{r=0} = -\frac{1}{2} \int_0^\infty \zeta_n(p, t) \, dp. \tag{5.20}$$

If we make the reasonable assumption that the symmetric vortex moves with the velocity of the asymmetric flow across its centre, the vortex speed is simply

$$\mathbf{c}(t) = \left[-\frac{\partial \Psi_2}{\partial r}\bigg|_{r=0}, \frac{\partial \Psi_1}{\partial r}\bigg|_{r=0} \right],$$ (5.21)

which can be evaluated using (5.14) and (5.20).

The assumption is reasonable because *at the vortex centre* $\zeta \gg f$ and the governing equation (5.1) expresses the fact that $\zeta + f$ is conserved following the motion. Since the symmetric circulation does not contribute to advection across the vortex centre (recall that the vortex centre is defined as the location of the maximum relative vorticity), advection must be by the asymmetric component. With the method of partitioning discussed in section 3.2, this component is simply the environmental flow by definition. The slight error committed in supposing that ζ is conserved rather than $\zeta + f$ is equivalent to neglecting the propagation of the vortex centre. The track error amounts to no more than a few kilometers per day which is negligible compared with the actual vortex displacements (e.g., see Fig. 5.6).

The vortex track, $\mathbf{X}(t) = [X(t), Y(t)]$ may be obtained by integrating the equation $d\mathbf{X}/dt = c(t)$, and using (5.20) and (5.21), we obtain

$$\left[\begin{array}{c} X(t) \\ Y(t) \end{array} \right] = \left[\begin{array}{c} \frac{1}{2} \int_0^\infty \left\{ \int_0^1 \zeta_2(p,t)dt \right\} dp \\ -\frac{1}{2} \int_0^\infty \left\{ \int_0^1 \zeta_1(p,t)dt \right\} dp \end{array} \right].$$ (5.22)

With the expressions for ζ_n in (5.14), this expression reduces to

$$\left[\begin{array}{c} X(t) \\ Y(t) \end{array} \right] = \left[\begin{array}{c} -\frac{1}{2}\beta \int_0^\infty r \left[t - \frac{\sin(\Omega(r)t)}{\Omega(r)} \right] dr \\ \frac{1}{2}\beta \int_0^\infty r \left[\frac{1-\cos(\Omega(r)t)}{\Omega(r)} \right] dr \end{array} \right].$$ (5.23)

This expression determines the vortex track in terms of the initial angular velocity profile of the vortex. To illustrate the solutions we choose the vortex profile used by Smith *et al.* (1990) so that we can compare the model results with their numerical solutions. The velocity profile $V(r)$ and corresponding angular velocity profile $\Omega(r)$ are shown as solid lines in Fig. 5.3. The maximum wind speed of 40 m s^{-1} occurs at a radius of 100 km and the region of approximate gale force winds (> 15 m s^{-1}) extends to 300 km. The angular velocity has a maximum at the vortex center and decreases monotonically with radius. Figure 5.6 shows the asymmetric vorticity field calculated from (5.14) and the corresponding streamfunction field from (5.16) at selected times, while Fig. 5.4 compares the analytical solutions with numerical solutions at 24 h.

The integrals involved are calculated using simple quadrature. After one minute the asymmetric vorticity and streamfunction fields show an east-west oriented dipole pattern. The vorticity maxima and minima occur at the radius of maximum tangential wind and there is a southerly component of the asymmetric flow across
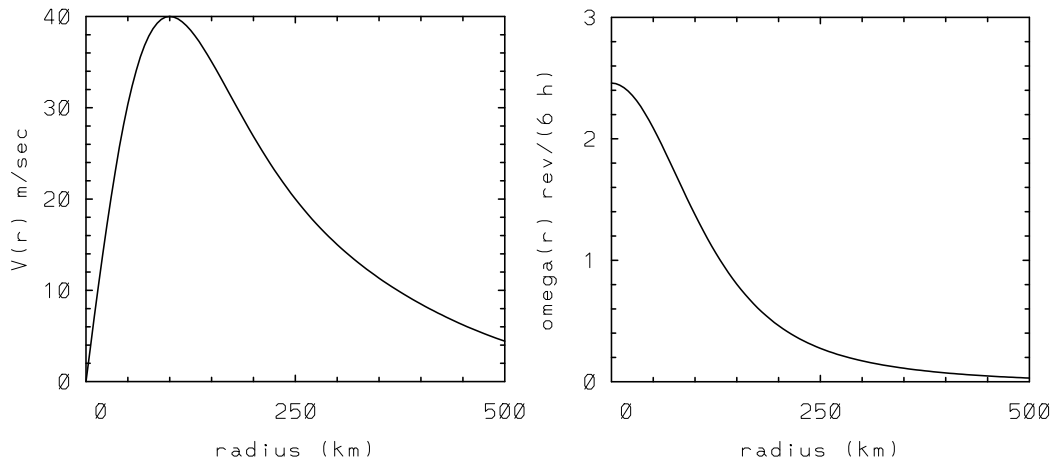
Figure 5.3: (left) Tangential velocity profile $V(r)$ and (right) angular velocity profile $\Omega(r)$ for the symmetric vortex.

the vortex center (Fig. 5.4a). As time proceeds, the vortex asymmetry is rotated by the symmetric vortex circulation and its strength and scale increase. The reasons for this behaviour are discussed below. In the inner core (typically $r < 200$ km), the asymmetry is rapidly sheared by the relatively large radial gradient of Ω (Fig. 5.4b). In response to these vorticity changes, the streamfunction dipole strengthens and rotates also, whereupon the asymmetric flow across the vortex center increases in strength and rotates northwestwards. Even at 24 h, the asymmetric vorticity and streamfunction patterns show remarkable similarity to those diagnosed from the complete numerical solution of Smith *et al.* (1990), which can be regarded as the control calculation (see Fig. 5.5). The numerical calculation was performed on a 2000 km × 2000 km domain with a 20 km grid size. Despite the apparent similarities between the analytically and numerically calculated vorticity patterns in Fig. 5.5, the small differences in detail are manifest in a more westerly oriented stream flow across the vortex center in the analytical solution and these are reflected in differences in the vortex tracks shown in Fig. 5.6. It follows that the analytical solution gives a track that is too far westward, but the average speed of motion is comparable with, but a fraction smaller than in the control case for this entire period. Even so, it is apparent that the simple analytic solution captures much of the dynamics in the full numerical solution.

Exercises

(3.1) Starting from Eq. 5.6 and the assumptions that air parcels move in circular orbits about the vortex centre while conserving their absolute vorticity and that the relative advection of vortex vorticity is small, show that the asymmetric
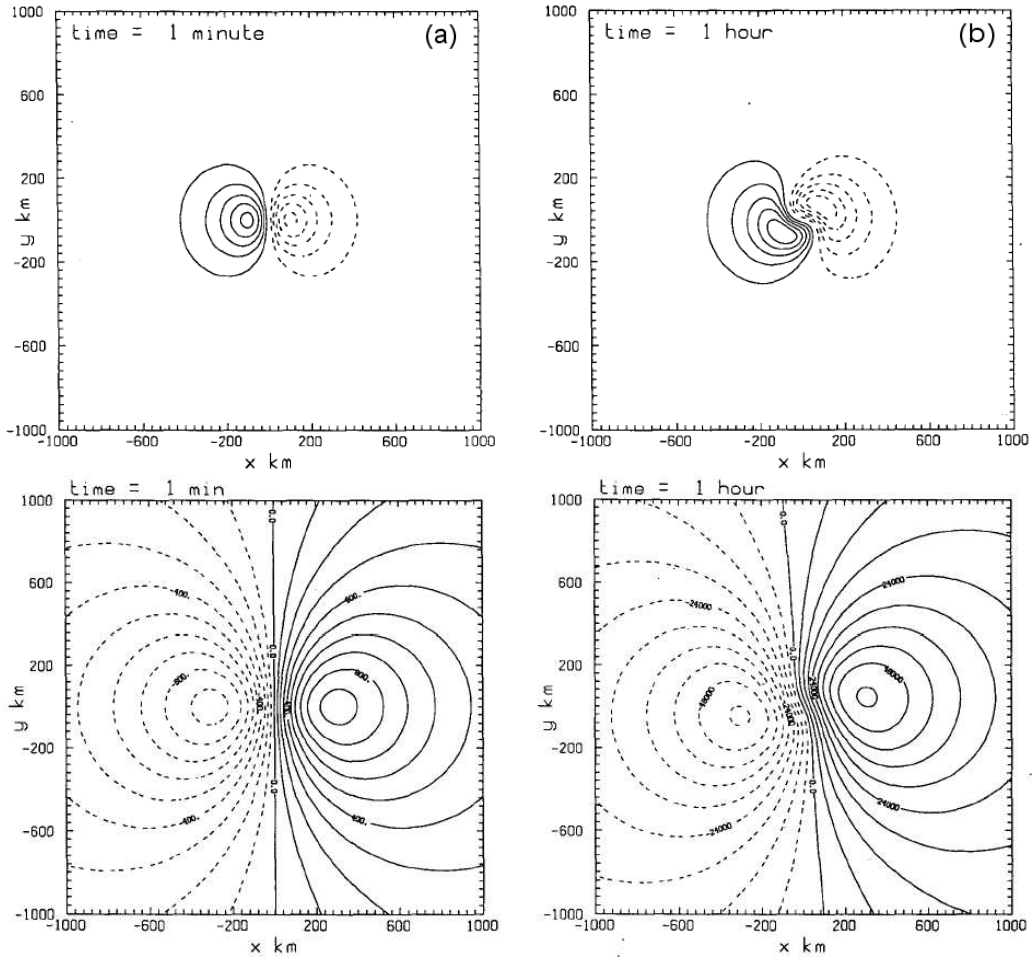
Figure 5.4: Asymmetric vorticity (top panels) and streamfunction fields (bottom panels) at selected times: (a) 1 min, (b) 1 h, (c) 3 h, (d) 12 h. Contour intervals for ζ_a are: 1×10^{-8} s^{-1} in (a), 5×10^{-7} s^{-1} in (b), 1×10^{-6} s^{-1} in (c), and 2×10^{-6} s^{-1} in (d). Contour intervals for ψ_a are: 100 m^2 s^{-1} in (a), 6×10^3 m^2 s^{-1} in (b), 1×10^4 m^2 s^{-1} in (c), and 5×10^4 m^2 s^{-1} in (d). (continued overleaf)

vorticity approximately satisfies the equation:

$$\frac{\partial \zeta_a}{\partial t} + \Omega(r)\frac{\partial \zeta_a}{\partial \lambda} = -\beta r \Omega(r) \sin \lambda. \tag{5.24}$$

(3.2) Show that the equation

$$\frac{\partial X}{\partial t} + \Omega(r,t)\frac{\partial X}{\partial \lambda} = -\beta r \Omega(r,t) \cos \lambda$$

has the solution

$$X = -\beta r(\sin \lambda - \sin(\lambda - \omega)),$$
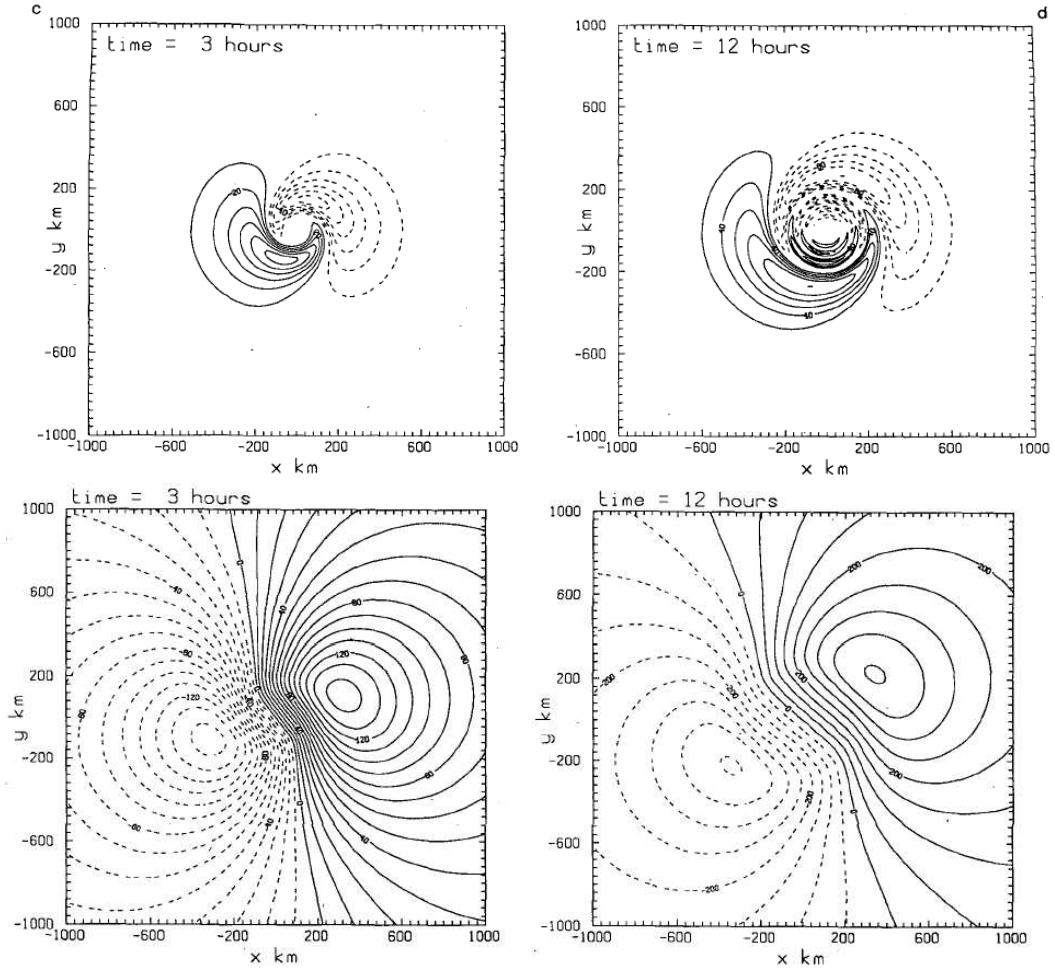
Fig. 5.4 (continued)

where

$$\omega = \int_0^t \Omega(r, t')dt'.$$

The analytic theory can be considerably improved by taking account of the contribution to the vorticity asymmetry, ζ_{a1}, by the relative advection of symmetric vortex vorticity, ζ_s. This contribution is represented by the term $-(\mathbf{U_a} - \mathbf{c}) \cdot \nabla \zeta_s$ in Eq. 5.6 (the second term on the right-hand-side). Again, with the assumption that air parcels move in circular orbits about the vortex centre while conserving their absolute vorticity, ζ_{a1} satisfies the equation:

$$\frac{\partial \zeta_{a1}}{\partial t} + \Omega(r)\frac{\partial \zeta_{a1}}{\partial \lambda} = -(\mathbf{U_a} - \mathbf{c}) \cdot \nabla \zeta_s, \qquad (5.25)$$

where the components of $\mathbf{U_a}$ are given by Eqs. (5.17) and (5.18), and $\mathbf{c}$ is given by Eq. (5.21). Further details of this calculation are given in Appendix 3.4.2. With

this correction there is excellent agreement between the numerically and analytically calculated tracks (compare the tracks AC and N in Fig. 5.6).
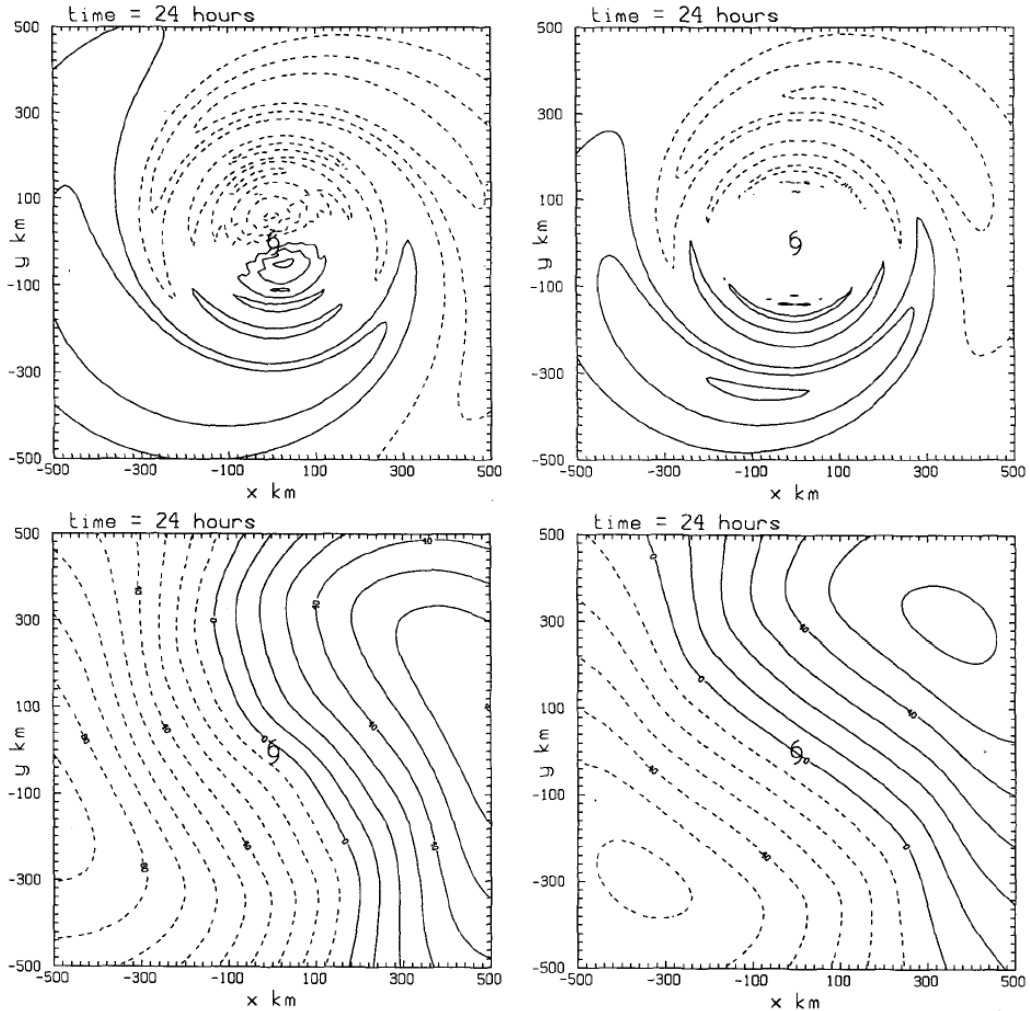
Figure 5.5: Comparison of the analytically-computed asymmetric vorticity and streamfunction fields (upper right and lower right) with those for the corresponding numerical solutions at 24 h. Only the inner part of the numerical domain, centred on the vortex centre, is shown (the calculations were carried out on a 2000 km × 2000 km domain). Contour intervals are 5×10^{-6} s^{-1} for ζ_a and 10^5 m^2 s^{-1} for ψ_a. The tropical cyclone symbol represents the vortex centre.

The foregoing analytical solution shows that the vorticity asymmetry is dominated by a pair of orthogonal dipoles with different radial profiles and strengths and that these profiles evolve with time. These profiles are characterized by the functions $\Psi_n(r,t)$ in Eq. (5.15), which are shown in Fig. 5.7 at 24 h. At this time the maximum amplitude of the vorticity asymmetry is located more than 350 km from the vortex centre, where the tangential wind speed of the vortex is only about one
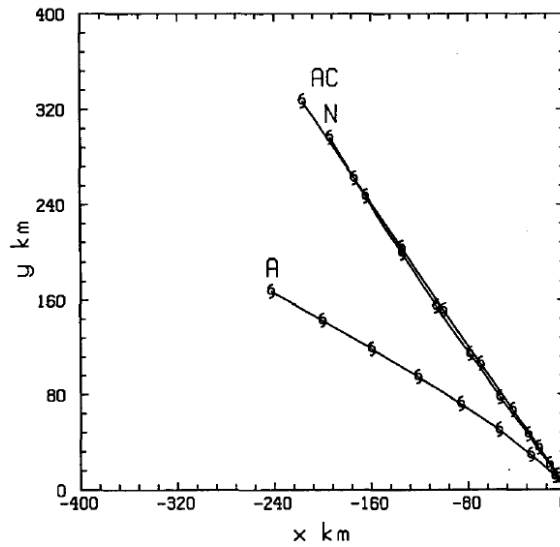
Figure 5.6: Comparison of the analytically calculated vortex track (denoted by A) compared with that for the corresponding numerical solution (denoted by N). The track by AC is the analytically corrected track referred to in the text.

quarter of its maximum value. As time proceeds, the strength of the asymmetry and the radius at which the maximum occurs continue to increase until about 60 h when the radius of the maximum stabilizes (see Smith *et al.* 1990, Fig. 5). This increase in the strength and scale of the gyres in the model is easy to understand if we ignore the motion of the vortex. As shown above, the change in relative vorticity of a fluid parcel circulating around the vortex is equal to its displacement in the direction of the absolute vorticity gradient times the magnitude of the gradient. For a fluid parcel at radius r the maximum possible displacement is $2r$, which limits the size of the maximum asymmetry at this radius. However, the time for this displacement to be achieved is $\pi/\Omega(r)$, where $\Omega(r)$ is the angular velocity of a fluid parcel at radius r. Since Ω is largest at small radii, fluid parcels there attain their maximum displacement relatively quickly, and as expected the maximum displacement of any parcel at early times occurs near the radius of maximum tangential wind (Fig. 5.8a). However, given sufficient time, fluid parcels at larger radii, although rotating more slowly, have the potential to achieve much larger displacements than those at small radii; as time continues, this is exactly what happens (Fig 5.8b). Ultimately, of course, if $\Omega(r)$ decreases monotonically to zero, there is a finite radius beyond which the tangential wind speed is less than the translation speed of the vortex. As the maximum in the asymmetry approaches this radius the vortex motion can no longer be ignored (see Smith and Ulrich 1990, Fig. 12).

Since the absolute vorticity is the conserved quantity in the barotropic flow problem it is instructive to examine the evolution of the isolines of this quantity as the flow evolves. At the initial time the contours are very close to circular near the vortex
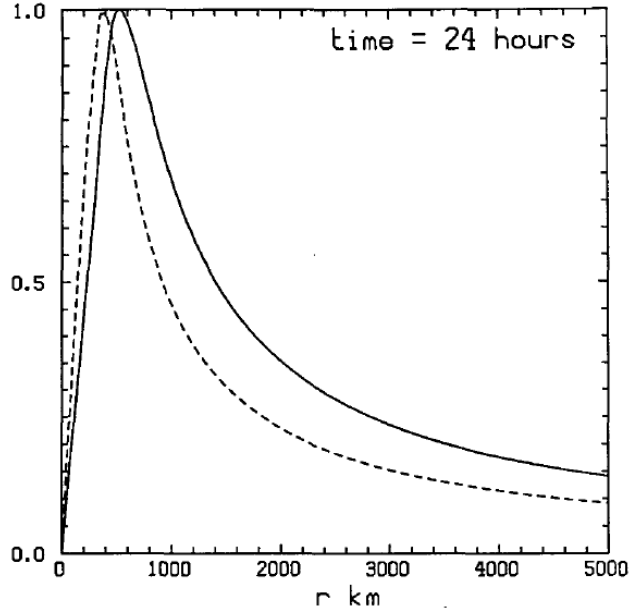
Figure 5.7: Radial profiles of Ψ_n/Ψ_{max} (n = 1, 2) at 24 hh where Ψ_{max} is the maximum absolute value of Ψ_n. Solid line is Ψ_1, dashed line is Ψ_2. Here, $\Psi_{1max} = 4.8 \times 10^5$ m^2 s^{-1}; $\Psi_{1max} = 4.2 \times 10^5$ m^2.

centre and are oriented zonally far from the centre. The pattern after 24 h, shown in Fig. 5.9, illustrates how contours are progressively wound around the vortex with those nearest the centre drawn out into long filaments. This filamentation process is associated with the strong angular shear of the tangential wind profile (see Fig. 5.3b). In reality, the strong gradients of asymmetric relative vorticity would be removed by diffusive processes. The filamentation is comparatively slow at larger radial distances so that coherent vorticity asymmetries occur outside the rapidly-rotating and strongly-sheared core. One consequence of these processes is that it is the larger-scale asymmetries that have the main effect on the vortex motion. On account of the filamentation process, there is a natural tendency for vortices to axisymmetrize disturbances in their cores. The axisymmetrization process in rapidly-rotating vortices is analyzed in more detail in section 4.1.

The analytic theory described above can be extended to account for higher-order corrections to the vorticity asymmetry. These corrections involve higher-order azimuthal wavenumber asymmetries. Mathematically an azimuthal wavenumber-n vorticity asymmetry has the form

$$\zeta_a(r, \lambda, n) = \zeta_1(r, t) \cos(n\lambda) + \zeta_2(r, t) \sin(n\lambda) \quad (n = 1, 2, \ldots),$$

which may be written

$$\zeta_a(r, \lambda, n) = \zeta_n(r, t) \cos(n\lambda + \alpha). \tag{5.26}$$
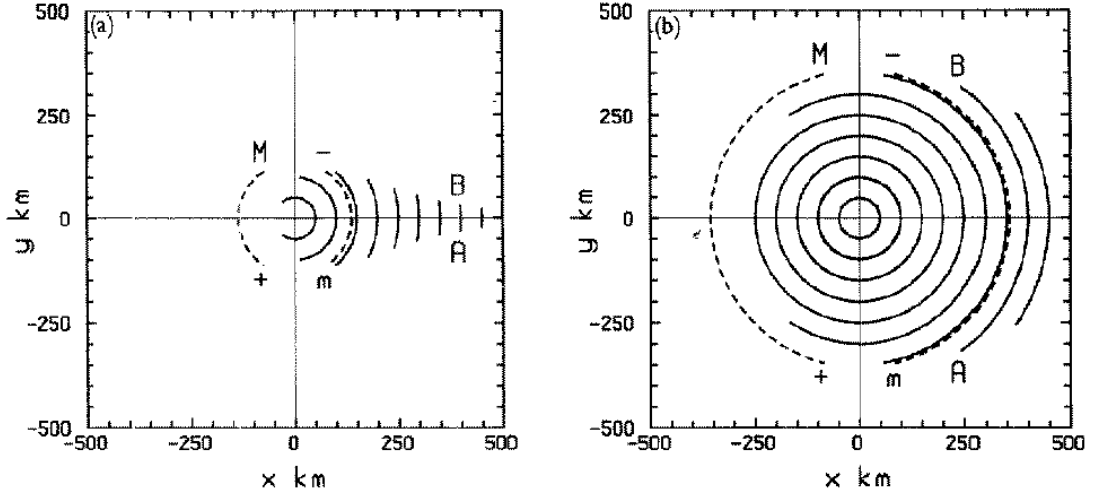
Figure 5.8: Approximate trajectories of fluid parcels which, for a given radius, give the maximum asymmetric vorticity contribution at that radius. The figures refer ro the case of motion of an initially-symmetric vortex on a β-plane with zero basic flow at (a) 1 h, (b) 24 h. The particles arc assumed to follow circular paths about the vortex centre (e.g. AB) with angular velocity $\Omega(r)$, where Ω decreases monotonically with radius r. Solid lines denote trajectories at 50 km radial intervals. Dashed lines marked 'M' and 'm' represent the trajectories giving the overall axisymmetric vorticity maxima and minima, respectively. These maxima and minima occur at the positive and negative ends of the relevant lines.

The associated streamfunction asymmetry has a similar form:

$$\psi_a(r, \lambda, n) = \psi_n(r, t) \cos(n\lambda + \alpha),$$

where(see Appendix 3.4.1)

$$\psi_0 = \int_0^r \frac{dp}{p} \int_0^s s\zeta_0(s, t)ds$$

$$\psi_n = \frac{1}{2n} \left[r^n \int_r^\infty p^{1-n}\zeta_n(p, t)dp - r^{-n} \int_0^r p^{1+n}\zeta_n(p, t)dp \right], \quad (n \neq 0).$$

The tracks obtained from the extended analytic theory agreed with considerable accuracy with those obtained from a numerical solution of the problem to at least 72 h, showing that theory captures the essential features of the dynamics (see Smith and Weber 1993).

5.3.3   The effects of horizontal shear and deformation

The analytic theory can be extended also to zonal basic flows of the form $\mathbf{U} = (U(y, t), 0)$ (Smith, 1991) and to more general flows with horizontal deformation
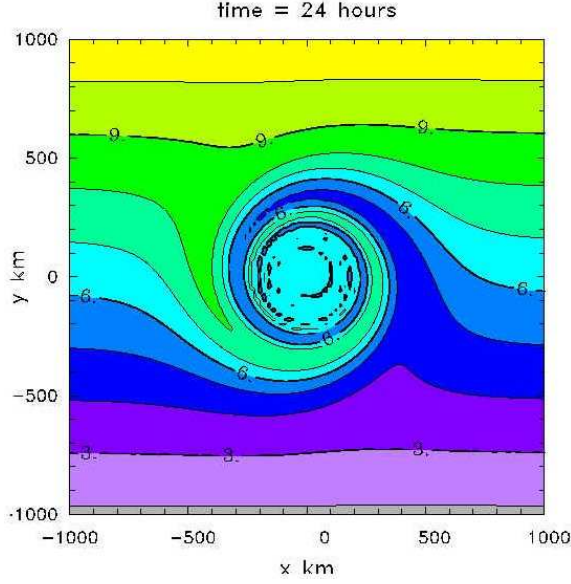
Figure 5.9: Analytically calculated absolute vorticity distribution at 24 h corresponding with the vorticity asymmetry in the upper right panel of Fig. 5.5.

(Krauss *et al.* 1995). For simplicity we consider here the case where U is a quadratic function of y only, i.e. $U = U_o + U'y + \frac{1}{2}U''y^2$. Let us partition the environmental flow at time t into two parts: the initial zonal flow, $\mathbf{U}$, and the part associated with the vortex-induced asymmetries, $\mathbf{U_a}$ and define the corresponding vorticities: $\Gamma = \mathbf{k} \cdot \nabla \wedge \mathbf{U}$ and $\zeta_a = \mathbf{k} \cdot \nabla \wedge \mathbf{U_a}$. Then, noting that $\mathbf{U}$ is normal to $\nabla(\Gamma + f)$, Eq. (5.6) may be written:

$$\frac{\partial \zeta_a}{\partial t} = -\mathbf{u_s} \cdot \nabla(\Gamma + f) - (\mathbf{U} + \mathbf{U_a} - \mathbf{c}) \cdot \nabla \zeta_s - \mathbf{U_a} \cdot \nabla(\Gamma + f). \quad (5.27)$$

Let us define $\mathbf{c} = \mathbf{U_c} + \mathbf{c'}$, and $\mathbf{U} = \mathbf{U_c}(t) + \mathbf{U_o}$, where $\mathbf{U_c}(t)$ is the speed of the zonal flow at the meridional position of the vortex and $\mathbf{U_o}$ contains the meridional variation of $\mathbf{U}$, then Eq. (5.27) becomes

$$\frac{\partial \zeta_a}{\partial t} = -\mathbf{u_s} \cdot \nabla(\Gamma + f) - \mathbf{U_o} \cdot \nabla \zeta_s + (\mathbf{U_a} - \mathbf{c'}) \cdot \nabla \zeta_s - \mathbf{U_a} \cdot \nabla(\Gamma + f). \quad (5.28)$$

The first term on the right-hand-side of this equation represents the asymmetric vorticity tendency, $\partial \zeta_{a1}/\partial t$, associated with the advection of the absolute vorticity gradient of the basic flow by the symmetric vortex circulation. The second term, $\partial \zeta_{a2}/\partial t$, is the asymmetric vorticity tendency associated with the basic shear acting on the symmetric vortex. The third term, $\partial \zeta_{a3}/\partial t$, is the asymmetric vorticity tendency associated with the advection of symmetric vorticity by the relative asymmetric flow; and the last term, $\partial \zeta_{a4}/\partial t$, is the asymmetric vorticity tendency associated with the advection of the absolute vorticity gradient of the basic flow by the asymmetric flow. Let $\zeta_{an}(n = 1 \ldots 4)$ be the contribution to ζ_a from $\partial \zeta_{an}/\partial t$. Then ζ_{a1}

has an azimuthal wavenumber-1 structure like ζ_a in Eq. (5.13) and the solution has the same form as (5.14), but with β replaced with the absolute vorticity gradient of the background flow, $\beta - U''$.

Case I: Uniform shear

For a linear velocity profile (i.e. for uniform shear, $U' = $ constant), $\mathbf{k}\cdot\nabla\Gamma = -U'' = 0$, so that the main difference compared to the calculation in the previous section is the emergence of an azimuthal wavenumber-2 vorticity asymmetry from the term ζ_{a2}, which satisfies the equation

$$\frac{\partial \zeta_{a2}}{\partial t} = -\mathbf{U_o} \cdot \nabla \zeta_s = -U'y \frac{\partial \zeta_s}{\partial x}.$$

This result is easy to understand by reference to Figs. 5.10 and 5.11. The vorticity gradient of the symmetric vortex is negative inside a radius of 255 km (say r_o) and positive outside this radius (Fig. 5.10). Therefore $\partial\zeta_s/\partial x$ is positive for $x > 0$ and $r > r_o$ and negative for $x < 0$ and $r < r_o$. If $U = U'y$, $U\partial\zeta_s/\partial x$ is negative in the first and third quadrants for $r > r_o$ and positive in the second and fourth quadrants (Figs. 5.11). For $r < r_o$, the signs are reversed.
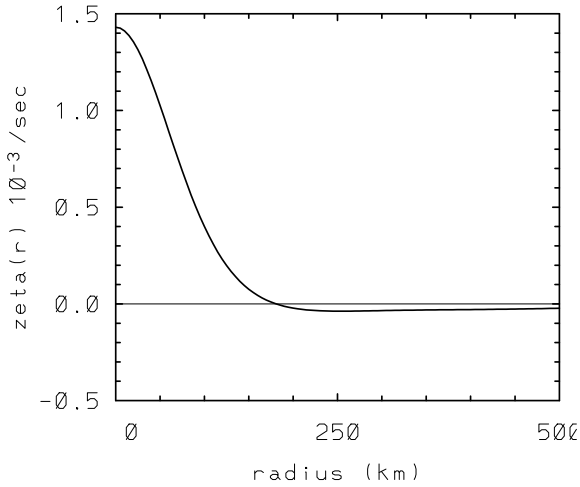
Figure 5.10: (left) Radial profile of vortex vorticity, $\zeta(r)$, corresponding with the tangential wind profile in Fig. 5.3.

Figure 5.12 shows the calculation of ζ_{a2} at 24 h when $U' = 5$ m s^{-1} per 1000 km. Since the vorticity tendency is relative to the motion of a rotating air parcel (Eq. (4.1)), the pattern of ζ_{a2} at inner radii is strongly influenced by the large radial shear of the azimuthal wind and consists of interleaving spiral regions of positive and negative vorticity. The maximum amplitude of ζ_{a2} (1.1×10^{-5} s^{-1} at 24 h) occurs at a radius greater than r_o. Note that azimuthal wavenumber asymmetries other than wavenumber-1 have zero flow at the origin and therefore have no effect on the vortex

Figure 5.11: Schematic depiction of the azimuthal wavenumber-2 vorticity tendency arising from the term $-\mathbf{U} \cdot \nabla \zeta_s = -U'y \partial \zeta_s / \partial x$ in the case of a uniform zonal shear $U = U'y$. (a) shows the sign of the vorticity gradient $\partial \zeta_s / \partial x$ in each quadrant for $0 < r < r_o$ and $r_o < r$ where r_o is the radius at which the vorticity gradient $d\zeta_s/dr$ changes sign (see Fig. 5.11) and (b) shows the vorticity tendency $-U \partial \zeta_s / \partial x$ in the eight regions.

motion. In the case of uniform shear, there is a small wavenumber-1 contribution to the asymmetry from the term ζ_{a4}, which satisfies the equation

$$\frac{\partial \zeta_{a4}}{\partial t} = -\mathbf{U_a} \cdot \nabla (\Gamma + f).$$

Case II: Linear shear

We consider now the case of a quadratic velocity profile (i.e. linear shear) in which U' is taken to be zero $\partial \Gamma / \partial y = -U''$ is nonzero. Linear shear has two particularly important effects that lead to a wavenumber-1 asymmetry, thereby affecting the vortex track. The first is characterized by the contribution to the absolute-vorticity gradient of the basic flow (the first term on the right-hand-side of Eq. (5.28), which directly affects the zero-order vorticity asymmetry, ζ_{a1}. The second is associated with the distortion of the vortex vorticity as depicted in Fig. 5.13 and represented mathematically by ζ_{a2}, which originates from the second term on the right-hand-side of Eq. (5.28).

Vortex tracks

Figure 5.14 shows the vortex tracks calculated from the analytic theory of Smith (1991) with the corresponding numerical calculations of Smith and Ulrich (1991). The broad agreement between the analytical and numerical calculations indicates
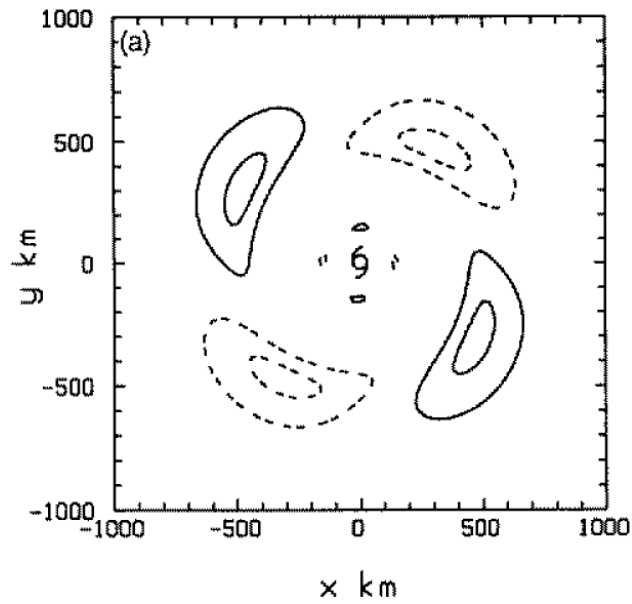
Figure 5.12: Asymmetric vorticity contribution for the case of a uniform zonal shear with $U' = 5$ m s^{-1} per 1000 km. Contour interval is 5×10^{-6} s^{-1}. Dashed lines indicate negative values. The vortex centre is marked by a cyclone symbol.

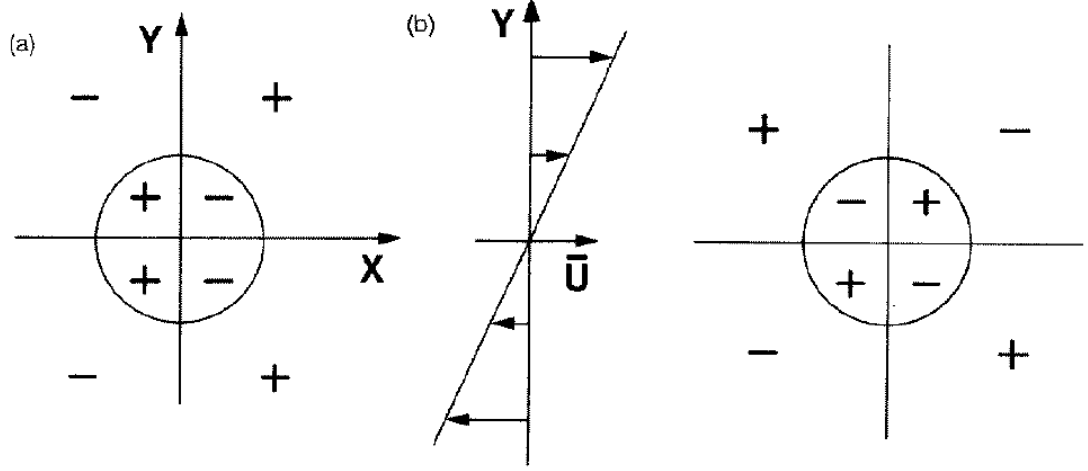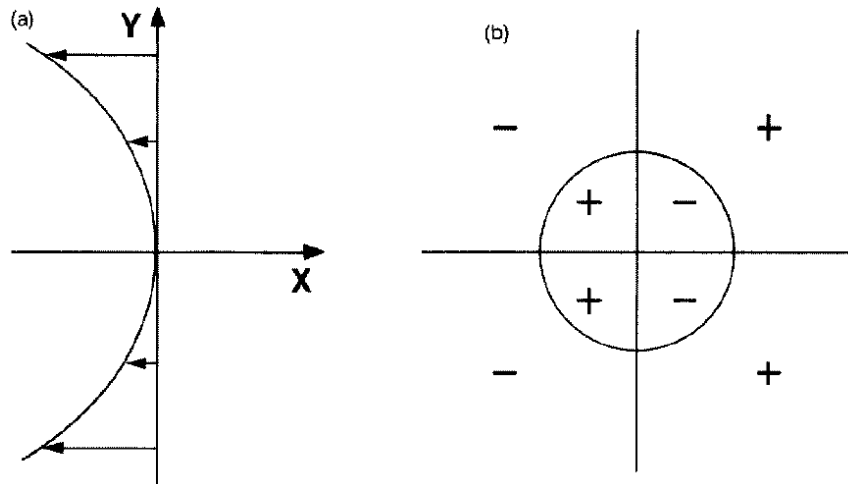

Figure 5.13: Schematic depiction of the wavenumber-1 vorticity tendency arising from the term $-\mathbf{U} \cdot \nabla \zeta_s = -U \partial \zeta_s / \partial x$ in the case of linear basic shear $U = -\frac{1}{2} U'' y^2$. (a) shows the profile $U(y)$ and (b) shows the vorticity tendency $-U \partial \zeta_s / \partial x$, in the eight regions defined in Fig. 5.10. The sign of $\partial \zeta_s / \partial x$ in these regions is shown in Fig. 5.10a.

that the analytic theory captures the essence of the dynamics involved, even though

the analytically-calculated motion is a little too fast. The eastward or westward displacement in the cases with zonal shear are in accordance with expectations that the vortex is advected by the basic flow and the different meridional displacements are attributed to the wavenumber-1 asymmetry, ζ_{a4} discussed above.

Panel (b) of Fig. 5.14 shows a similar comparison for two cases of a linear shear: SNB with $U'' = \beta_o$ and $\beta = 0$; SHB $U'' = \frac{1}{2}\beta_o$ and $\beta = \frac{1}{2}\beta_o$; and the case of zero basic flow (ZBF) with $\beta = \beta_o$. Here β_o is the standard value of β. These three calculations have the same absolute vorticity gradient, β_o, but the relative contribution to it from U'' and β is different. Note that the poleward displacement is reduced as U'' increases in magnitude. Again this effect can be attributed to the wavenumber-one asymmetry ζ_{a2} discussed above.
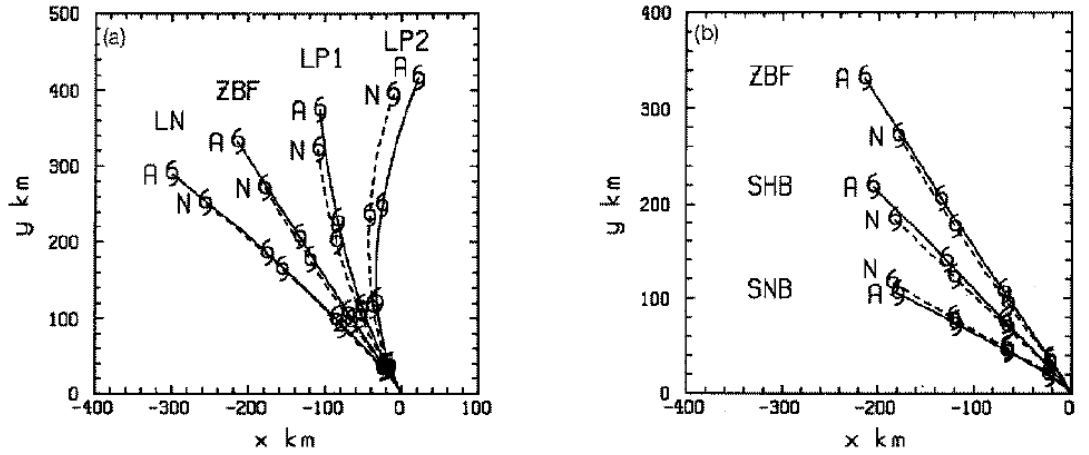
Figure 5.14: Analytically calculated vortex track (denoted by A) compared with the corresponding numerical solution (denoted by N): (a) uniform shear flow cases and [b) linear shear flow cases. Each panel includes the analytically and numerically calculated track for the case of zero basic; flow (denoted ZBF). Cyclone symbols mark the vortex position at 12-h intervals. (See text for explanation of other letters.)

5.4 The motion of baroclinic vortices

As a start to examining the motion of baroclinic vortices it is instructive to consider first the vorticity tendency for a baroclinic vortex $v(r, z)$ in a zonal shear flow $U(z)$.

5.4.1 Vorticity tendency for a baroclinic vortex $v(r, z)$ in a zonal shear flow $U(z)$.

Consider the velocity vector:

$$\mathbf{u} = U(z)\hat{\mathbf{i}} + v(r, z)\hat{\boldsymbol{\theta}} = U\cos\theta\hat{\mathbf{r}} + (v - U\sin\theta)\hat{\boldsymbol{\theta}} \tag{5.29}$$

The vorticity in cylindrical coordinates is

$$\boldsymbol{\omega} = \frac{1}{r}\left(\frac{\partial u_z}{\partial \theta} - \frac{\partial r u_\theta}{\partial z}\right)\hat{\mathbf{r}} + \left(\frac{\partial u_r}{\partial z} - \frac{\partial u_z}{\partial r}\right)\hat{\boldsymbol{\theta}} + \frac{1}{r}\left(\frac{\partial r u_\theta}{\partial r} - \frac{\partial u_r}{\partial \theta}\right)\hat{\mathbf{k}},$$

so that for the velocity vector (5.29),

$$\boldsymbol{\omega} = \left(-\frac{\partial}{\partial z}(v - U\sin\theta)\right)\hat{\mathbf{r}} + \left(\frac{\partial}{\partial z}U\cos\theta\right)\hat{\boldsymbol{\theta}} + \left(\frac{1}{r}\frac{\partial}{\partial r}r(v - U\sin\theta) - \frac{1}{r}\frac{\partial}{\partial \theta}U\cos\theta\right)\hat{\mathbf{k}}$$

or

$$\boldsymbol{\omega} = \left(\frac{dU}{dz}\sin\theta - \frac{\partial v}{\partial z}\right)\hat{\mathbf{r}} + \frac{dU}{dz}\cos\theta\hat{\boldsymbol{\theta}} + \frac{1}{r}\frac{\partial rv}{\partial r}\hat{\mathbf{k}}$$

Let us write

$$\boldsymbol{\omega} = \left(\xi + \frac{dU}{dz}\sin\theta\right)\hat{\mathbf{r}} + \frac{dU}{dz}\cos\theta\hat{\boldsymbol{\theta}} + \zeta\hat{\mathbf{k}} \tag{5.30}$$

Now, in cylindrical coordinates (see Batchelor, 1970, p602)

$$\mathbf{u}.\nabla\boldsymbol{\omega} = \left(\mathbf{u}.\nabla\omega_r - \frac{u_\theta\omega_\theta}{r}\right)\hat{\mathbf{r}} + \left(\mathbf{u}.\nabla\omega_\theta + \frac{u_\theta\omega_r}{r}\right)\hat{\boldsymbol{\theta}} + \left(\mathbf{u}.\nabla\omega_z\right)\hat{\mathbf{k}}$$

Then for the velocity vector (5.29),

$$\mathbf{u}.\nabla\boldsymbol{\omega} = \left(\mathbf{u}.\nabla\left(\xi + \frac{dU}{dz}\sin\theta\right) - \frac{u_\theta}{r}\frac{dU}{dz}\sin\theta\right)\hat{\mathbf{r}} +$$

$$\left(\mathbf{u}.\nabla\omega_\theta + \frac{u_\theta}{r}\left(\xi + \frac{dU}{dz}\sin\theta\right)\right)\hat{\boldsymbol{\theta}} + (\mathbf{u}.\nabla\zeta)\hat{\mathbf{k}}$$

The three components of this equation are:

$$\begin{aligned}
\left(\mathbf{u}.\nabla\xi - \frac{u_\theta\omega_\theta}{r}\right) &= U\cos\theta\frac{\partial}{\partial r}\left(\xi + \frac{dU}{dz}\sin\theta\right) \\
&+ (v - U\sin\theta)\frac{1}{r}\frac{\partial}{\partial\theta}\left(\xi + \frac{dU}{dz}\sin\theta\right) - \frac{(v - U\sin\theta)}{r}\frac{dU}{dz}\cos\theta \\
&= U\cos\theta\frac{\partial\xi}{\partial r}
\end{aligned}$$

$$\begin{aligned}
\left(\mathbf{u}.\nabla\omega_\theta + \frac{u_\theta\omega_r}{r}\right) &= U\cos\theta\frac{\partial}{\partial r}\left(\frac{dU}{dz}\cos\theta\right) \\
&+ (v - U\sin\theta)\frac{1}{r}\frac{\partial}{\partial\theta}\left(\frac{dU}{dz}\cos\theta\right) + \frac{(v - U\sin\theta)}{r}\left(\xi + \frac{dU}{dz}\sin\theta\right) \\
&= \frac{(v - U\sin\theta)}{r}\xi
\end{aligned}$$

$$\mathbf{u}.\nabla\omega_z = U\cos\theta\frac{\partial\zeta}{\partial r} + \frac{(v - U\sin\theta)}{r}\frac{\partial\zeta}{\partial\theta} = U\cos\theta\frac{\partial\zeta}{\partial r}$$

Therefore

$$\mathbf{u}.\nabla\boldsymbol{\omega} = U\cos\theta\frac{\partial\xi}{\partial r}\hat{\mathbf{r}} + \frac{(v - U\sin\theta)}{r}\xi\hat{\boldsymbol{\theta}} + U\cos\theta\frac{\partial\zeta}{\partial r}\hat{\mathbf{k}} \qquad (5.31)$$

Now

$$\boldsymbol{\omega}.\nabla\mathbf{u} = \left(\boldsymbol{\omega}.\nabla u_r - \frac{\omega_\theta u_\theta}{r}\right)\hat{\mathbf{r}} + \left(\boldsymbol{\omega}.\nabla u_\theta + \frac{\omega_\theta u_r}{r}\right)\hat{\boldsymbol{\theta}} + (\boldsymbol{\omega}.\nabla u_z)\hat{\mathbf{k}}. \qquad (5.32)$$

The first component of this equation is

$$\boldsymbol{\omega}.\nabla u_r - \frac{\omega_\theta u_\theta}{r} = \left[\left(\xi + \frac{dU}{dz}\sin\theta\right)\hat{\mathbf{r}} + \frac{dU}{dz}\cos\theta\hat{\boldsymbol{\theta}} + \zeta\hat{\mathbf{k}}\right] \quad \times$$

$$\left(\frac{\partial}{\partial r}(U\cos\theta)\hat{\mathbf{r}} + \frac{1}{r}\frac{\partial}{\partial\theta}(U\cos\theta)\hat{\boldsymbol{\theta}} + \frac{\partial}{\partial z}(U\cos\theta)\hat{\mathbf{k}}\right) - \frac{v - U\sin\theta}{r}\frac{dU}{dz}\cos\theta$$

$$= -\frac{U}{r}\frac{dU}{dz}\cos\theta\sin\theta + \zeta\frac{dU}{dz}\cos\theta - \frac{v - U\sin\theta}{r}\frac{dU}{dz}\cos\theta$$

or, finally

$$\boldsymbol{\omega}.\nabla u_r - \frac{\omega_\theta u_\theta}{r} = \zeta \frac{dU}{dz}\cos\theta - \frac{v}{r}\frac{dU}{dz}\cos\theta = \frac{dv}{dr}\frac{dU}{dz}\cos\theta \qquad (5.33)$$

The second component of (5.33) is

$$\boldsymbol{\omega}.\nabla u_\theta + \frac{\omega_\theta u_r}{r} = \left[\left(\xi + \frac{dU}{dz}\sin\theta\right)\hat{\mathbf{r}} + \frac{dU}{dz}\cos\theta\hat{\boldsymbol{\theta}} + \zeta\mathbf{k}\right] \quad \times$$

$$\left[\frac{\partial}{\partial r}(v - U\sin\theta)\hat{\mathbf{r}} + \frac{1}{r}\frac{\partial}{\partial\theta}(v - U\sin\theta)\hat{\boldsymbol{\theta}} + \frac{\partial}{\partial z}(v - U\sin\theta)\hat{\mathbf{k}}\right] + \frac{U\cos\theta}{r}\frac{dU}{dz}\cos\theta$$

$$= \left[\left(\xi + \frac{dU}{dz}\sin\theta\right)\hat{\mathbf{r}} + \frac{dU}{dz}\cos\theta\hat{\boldsymbol{\theta}} + \zeta\mathbf{k}\right] \quad \times$$

$$\left[\frac{\partial v}{\partial r}\hat{\mathbf{r}} - \frac{U}{r}\cos\theta\hat{\boldsymbol{\theta}} + \left(\frac{\partial v}{\partial z} - \frac{dU}{dz}\sin\theta\right)\hat{\mathbf{k}}\right] + \frac{U}{r}\frac{dU}{dz}\cos^2\theta$$

$$= \left(\xi + \frac{dU}{dz}\sin\theta\right)\frac{\partial v}{\partial r} - \zeta\left(\xi + \frac{dU}{dz}\sin\theta\right) = \left(\frac{\partial v}{\partial r} - \zeta\right)\left(\xi + \frac{dU}{dz}\sin\theta\right),$$

or, finally,

$$\boldsymbol{\omega}.\nabla u_\theta + \frac{\omega_\theta u_r}{r} = -\frac{v}{r}\left(\xi + \frac{dU}{dz}\sin\theta\right) \qquad (5.34)$$

The third component of (5.33) is simply

$$\boldsymbol{\omega}.\nabla u_z = 0 \qquad (5.35)$$

The (5.32) may be written

$$\boldsymbol{\omega}.\nabla\mathbf{u} = \frac{dv}{dr}\frac{dU}{dz}\cos\theta\hat{\mathbf{r}} - \frac{v}{r}\left(\xi + \frac{dU}{dz}\sin\theta\right)\hat{\boldsymbol{\theta}} \qquad (5.36)$$

$$\frac{\partial\boldsymbol{\omega}}{\partial t} = -\mathbf{u}\cdot\nabla\boldsymbol{\omega} + \boldsymbol{\omega}\cdot\nabla\mathbf{u}$$

$$\mathbf{u}.\nabla\boldsymbol{\omega} = U\cos\theta\frac{\partial\xi}{\partial r}\hat{\mathbf{r}} + \frac{(v - U\sin\theta)}{r}\left(\xi - \frac{dU}{dz}\sin\theta\right)\hat{\boldsymbol{\theta}} + U\cos\theta\frac{\partial\zeta}{\partial r}\hat{\mathbf{k}}$$

$$\frac{\partial\boldsymbol{\omega}}{\partial t} = -\left(U\cos\theta\frac{\partial\xi}{\partial r}\hat{\mathbf{r}} + \frac{(v - U\sin\theta)}{r}\xi\hat{\boldsymbol{\theta}} + U\cos\theta\frac{\partial\zeta}{\partial r}\hat{\mathbf{k}}\right) +$$

$$\frac{dv}{dr}\frac{dU}{dz}\cos\theta\hat{\mathbf{r}} - \frac{v}{r}\left(\xi + \frac{dU}{dz}\sin\theta\right)\hat{\boldsymbol{\theta}}$$

$$= \left(-U\frac{\partial\xi}{\partial r} + \frac{dv}{dr}\frac{dU}{dz}\right)\cos\theta\hat{\mathbf{r}} - \left[\left(\frac{v}{r} + \frac{(v - U\sin\theta)}{r}\right)\xi - \frac{v}{r}\frac{dU}{dz}\sin\theta\right]\hat{\boldsymbol{\theta}} - U\cos\theta\frac{\partial\zeta}{\partial r}\hat{\mathbf{k}},$$

or finally,

$$\frac{\partial\boldsymbol{\omega}}{\partial t} = \left(-U\frac{\partial\xi}{\partial r} + \frac{dv}{dr}\frac{dU}{dz}\right)\cos\theta\hat{\mathbf{r}} - \left[\left(\frac{2v}{r} - \frac{U\sin\theta}{r}\right)\xi + \frac{v}{r}\frac{dU}{dz}\sin\theta\right]\hat{\boldsymbol{\theta}} - U\cos\theta\frac{\partial\zeta}{\partial r}\hat{\mathbf{k}}$$

$$(5.37)$$

Special cases:

1. Uniform flow (U = constant), barotropic vortex, $v = v(r) \Rightarrow \xi = 0$

$$\frac{\partial \boldsymbol{\omega}}{\partial t} = -U \cos \theta \frac{\partial \zeta}{\partial r} \hat{\mathbf{k}} \quad \Rightarrow \quad \frac{\partial \zeta}{\partial t} = -U \frac{\partial \zeta}{\partial x}$$

In this case there is only vertical vorticity and this is simply advected by the basic flow as discussed in Chapter 5.

2. No basic flow ($U = 0$), baroclinic vortex, $v = v(r, z)$

$$\frac{\partial \boldsymbol{\omega}}{\partial t} = -\frac{2v}{r} \xi \hat{\boldsymbol{\theta}}$$

$$\frac{\partial \xi}{\partial t} = 0, \quad \frac{\partial \eta}{\partial t} = -\frac{2v}{r} \xi, \quad \frac{\partial \zeta}{\partial t} = 0$$

In this case there are initially two components of vorticity, a radial component and vertical vertical component, but in general, the vortex does not remain stationary as there is generation of toroidal vorticity. The exception is, of course, when the vortex is in thermal-wind balance in which case there is generation of toroidal vorticity of the opposite sign by the horizontal density gradient so that the net rate-of-generation of toroidal vorticity is everywhere zero.

3. Uniform flow (U = constant), baroclinic vortex, $v = v(r, z)$

$$\frac{\partial \boldsymbol{\omega}}{\partial t} = -U \cos \theta \frac{\partial \xi}{\partial r} \hat{\mathbf{r}} - \left(\frac{2v}{r} - \frac{U \sin \theta}{r} \right) \xi \hat{\boldsymbol{\theta}} - U \cos \theta \frac{\partial \zeta}{\partial r} \hat{\mathbf{k}}$$

$$\frac{\partial \xi}{\partial t} = -U \frac{\partial \xi}{\partial x} \quad \frac{\partial \eta}{\partial t} = -\left(\frac{2v}{r} - \frac{U \sin \theta}{r} \right) \xi \quad \frac{\partial \zeta}{\partial t} = -U \frac{\partial \zeta}{\partial x}$$

Again there are initially two components of vorticity, a radial component and vertical vertical component, and again there is generation of toroidal vorticity unless the vortex is in thermal-wind balance. However, even in the latter case there would appear to be a generation of toroidal vorticity at the rate $(U \sin \theta / r) \xi$. It can be shown that this rate-of-generation is associated with the coordinate system represented by the unit vectors $\hat{\mathbf{r}}, \hat{\theta}, \hat{\mathbf{k}}$, is fixed (see Exercise 5.1). Thus as the vortex moves away from the origin of coordinates, the radial component of vorticity in the moving frame projects onto the $\hat{\theta}$-component in the fixed frame.

4. Uniform shear flow ($dU/dz = \text{constant} = U'$), barotropic vortex, $v = v(r) \Rightarrow$
$\xi = 0$

$$\frac{\partial \boldsymbol{\omega}}{\partial t} = \frac{dv}{dr}\frac{dU}{dz}\cos\theta\hat{\mathbf{r}} + \frac{v}{r}\frac{dU}{dz}\sin\theta\hat{\boldsymbol{\theta}} + U\cos\theta\frac{\partial \zeta}{\partial r}\hat{\mathbf{k}}$$

$$\frac{\partial \xi}{\partial t} = -U\frac{\partial \xi}{\partial x} + \frac{dv}{dr}\frac{dU}{dz}\cos\theta \quad \frac{\partial \eta}{\partial t} = \frac{v}{r}\frac{dU}{dz}\sin\theta \quad \frac{\partial \zeta}{\partial t} = -U\frac{\partial \zeta}{\partial x}$$

Translation of the balanced density field

Let $\rho = p_0(r,z)$ at time $t = 0$.
Then

$$\frac{\partial \rho}{\partial t} = -\nabla \cdot (\rho \mathbf{u}) = -\mathbf{u} \cdot \nabla \rho - \rho(\nabla \cdot \mathbf{u}).$$

Now the velocity field $\mathbf{u} = (U\cos\theta, \, v - U\sin\theta, \, 0)$ is nondivergent ($\nabla \cdot \mathbf{u} = 0$)
and therefore

$$\frac{\partial \rho}{\partial t} = -U\cos\theta\frac{\partial \rho}{\partial r} - \frac{(v - U\sin\theta)}{r}\frac{\partial \rho}{\partial \theta}.$$

The second term on the right-hand-side is zero because ρ is dependent of θ whereupon

$$\frac{\partial \rho}{\partial t} = -U\frac{\partial \rho}{\partial x}$$

and the density field is simply advected at speed U.

Exercise 5.1 Show that the term $(U\sin\theta/r)\xi$ in Eqs. (**??**) is the rate-of-

generation of toroidal vorticity in the fixed coordinate system represented by the
unit vectors $\hat{\mathbf{r}}, \hat{\theta}, \hat{\mathbf{k}}$ due to the subsequent displacement of the vortex centre from the
coordinate origin.

Exercise 5.2 Show that

$$\frac{\partial}{\partial r} = \frac{\partial}{\partial x}\frac{\partial x}{\partial r} + \frac{\partial}{\partial y}\frac{\partial y}{\partial r} = \cos\theta\frac{\partial}{\partial x} + \sin\theta\frac{\partial}{\partial y},$$

and

$$\frac{1}{r}\frac{\partial}{\partial \theta} = \frac{1}{r}\frac{\partial}{\partial x}\frac{\partial x}{\partial \theta} + \frac{1}{r}\frac{\partial}{\partial y}\frac{\partial y}{\partial \theta} = -\sin\theta\frac{\partial}{\partial x} + \cos\theta\frac{\partial}{\partial y},$$

Deduce that

$$\frac{\partial}{\partial x} = \cos\theta\frac{\partial}{\partial r} - \frac{\sin\theta}{r}\frac{\partial}{\partial \theta},$$

and

$$\frac{\partial}{\partial y} = \sin\theta \frac{\partial}{\partial r} + \frac{\cos\theta}{r}\frac{\partial}{\partial\theta}.$$
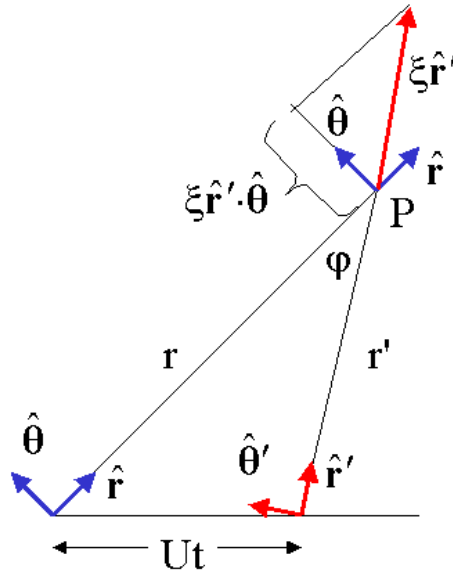
Figure 5.15: See text for discussion.

Solution to Exercise 5.1

Let the vortex be centred at the origin at time $t = 0$ and at a position Ut from the origin at time t (Fig. 5.15). At time t, the radial component of vorticity is $\omega_r' \hat{\mathbf{r}}' = \xi\hat{\mathbf{r}}'$ and we are interested in the projection of this vector in the $\hat{\boldsymbol{\lambda}}'$ direction. In particular we want to calculate its rate of change

$$\Lambda = \frac{d}{dt}(\xi\hat{\mathbf{r}}'\cdot\hat{\boldsymbol{\lambda}}) = \xi\frac{d}{dt}\sin\phi$$

Consider $\mathbf{r}\wedge\mathbf{r}' = |\mathbf{r}||\mathbf{r}'|\sin\phi\hat{\mathbf{k}}$, where $\hat{\mathbf{k}}$ is a vector normal to the plane of $\mathbf{r}$ and $\hat{\mathbf{r}}'$ and note that $\mathbf{r}' = \mathbf{r} - X\mathbf{i}$. Then

$$\hat{k}\sin\phi = \frac{X i \wedge r'}{|\mathbf{r}|\,|\mathbf{r}'|} = \hat{k}\frac{X}{|r|}\sin\lambda$$

so that

$$\frac{d}{dt}\sin\phi = \frac{1}{r}\sin\lambda\frac{dX}{dt} = \frac{U}{r}\sin\lambda$$

and therefore

$$\Lambda = \frac{U}{r}\xi\sin\lambda$$

as required.

5.4.2   The effects of vertical shear

Discuss Jones (1995, 2000a, 2000b, 2004), Smith and Ulrich (2000) and Reasor and Montgomery (2004).

5.5 Appendices to Chapter 5

5.5.1 Derivation of Eq. 5.16

We require the solution of $\quad \nabla^2 \psi_a = \zeta$, when $\zeta_a(r, \theta) = \hat{\zeta}(r)e^{in\theta}$. Now

$$\nabla^2 \psi_a = \frac{\partial^2 \psi_a}{\partial r^2} + \frac{1}{r}\frac{\partial \psi_a}{\partial r} + \frac{1}{r^2}\frac{\partial^2 \psi_a}{\partial \theta^2} = \hat{\zeta}(r)e^{in\theta}$$

Put $\quad \psi = \hat{\psi}(r)e^{in\theta}$, then

$$\frac{d^2 \hat{\psi}}{dr^2} + \frac{1}{r}\frac{d\hat{\psi}}{dr} - \frac{n^2}{r^2}\hat{\psi} = \hat{\zeta}(r). \tag{5.38}$$

When $\hat{\zeta}(r) = 0$, the equation has solutions $\hat{\psi} = r^\alpha$ where

$$[\alpha(\alpha - 1) + \alpha - n^2]r^{\alpha - 2} = 0,$$

which gives

$$\alpha^2 - n^2 = 0 \quad \text{or} \quad \alpha = \pm n.$$

Therefore, for a solution of (5.38), try $\hat{\psi} = r^n \phi(r)$. Then

$$\psi_r = r^n \phi_r + nr^{n-1}\phi, \qquad \psi_{rr} = r^n \phi_{rr} + 2nr^{n-1}\phi_r + n(n-1)r^{n-2}\phi \tag{5.39}$$

whereupon (5.38) gives

$$\begin{aligned} r^n \phi_{rr} \quad &+ \quad 2nr^{n-1}\phi_r + n(n-1)r^{n-2}\phi \\ &+ \quad r^{n-1}\phi_r + nr^{n-2}\phi - n^2 r^{n-2}\phi = \hat{\zeta}, \end{aligned}$$

or

$$r^n \phi_{rr} + (2n+1)r^{n-1}\phi_r = \hat{\zeta}.$$

Multiply by r^β and choose β so that $n + \beta = 2n + 1$, i.e., $\beta = n + 1$. Thus r^{n+1} is the integrating factor. Then

$$\frac{d}{dr}\left[r^{2n+1}\phi(r)\right] = r^{n+1}\hat{\zeta}(r), \tag{5.40}$$

which may ne integrated to give

$$r^{2n+1}\frac{d\phi}{dr} = \int_r^\infty p^{n+1}\hat{\zeta}(p)dp + A,$$

where A is a constant. Therefore

$$\frac{d\phi}{dr} = \frac{1}{r^{2n+1}}\int_r^\infty p^{n+1}\hat{\zeta}(p)dp + \frac{A}{r^{2n+1}}$$
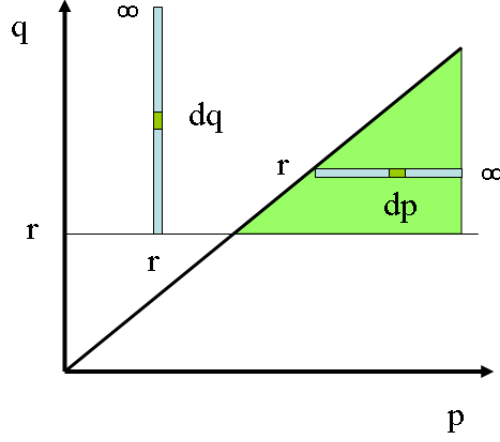
Figure 5.16: The domain of integration for the integral (5.41) is the shaded region.

Finally,

$$\phi = \int_r^\infty \frac{dq}{q^{2n+1}} \int_q^\infty p^{n+1}\hat{\zeta}(p)dp + \int_q^\infty \frac{Adq}{q^{2n+1}} + B, \qquad (5.41)$$

where B is another another constant. The domain of the double integral is the shaded region shown in Fig. 5.16 in which p goes from q to ∞ then q goes from r to ∞. If we change the order of integration in (5.41), q goes from r to p and then p goes from r to ∞, i.e.

$$
\begin{aligned}
\phi &= \int_r^\infty p^{n+1}\zeta(p)dp \int_r^p \frac{dq}{q^{(2n+1)}} - \frac{A}{2nr^{2n}} + B \\
&= \frac{1}{2n}\left[\int_r^\infty p^{n+1}\hat{\zeta}(p)dp - A\right]\frac{1}{r^{2n}} + B - \frac{1}{2n}\int_0^r p^{1-n}\hat{\zeta}(p)dp.
\end{aligned}
$$

Finally

$$\hat{\psi}(r) = -\frac{r^n}{2n}\int_0^r p^{1-n}\hat{\zeta}(p)dp + Br^n + \frac{1}{2nr^n}\left[\int_r^\infty p^{n+1}\hat{\zeta}(p)dp - A\right].$$

Now $\hat{\psi}(r)$ finite at $r = 0$ requires that

$$A = \int_0^\infty p^{n+1}\hat{\zeta}(p)dp$$

and $\hat{\psi}(r)$ finite as $r \to \infty$ requires that

$$B = \int_0^\infty p^{1-n}\hat{\zeta}(p)dp$$

Therefore

$$\hat{\psi}(r) = -\frac{r^n}{2n} \int_r^\infty p^{1-n} \hat{\zeta}(p) dp - \frac{r^{-n}}{2n} \int_r^0 p^{n+1} \hat{\zeta}(p) dp, \tag{5.42}$$

as required.

5.5.2 Solution of Eq. 5.25

The asymmetric flow $\mathbf{U}_a$ is obtained from Eqs. (5.17) and (5.18) and $\mathbf{c}$ is obtained from (5.21). We can calculate the streamfunction Ψ_a' of the *vortex-relative* flow $\mathbf{U}_a - \mathbf{c}$, from

$$\psi_n' = \psi_a - \psi_c,$$

where

$$\psi_c' = r(V_a \cos\lambda - U_a \sin\lambda) = r \left[\frac{\partial \Psi_1}{\partial r} \Big|_{r=0} \cos\lambda + \frac{\partial \Psi_2}{\partial r} \Big|_{r=0} \sin\lambda \right]. \tag{5.43}$$

Then using (5.15), (5.16), (5.20) and (5.43) we obtain

$$\psi_a' = \Psi_1'(r,t) \cos\theta + \Psi_2'(r,t) \sin\theta, \tag{5.44}$$

where

$$\begin{aligned} \Psi_n'(r,t) &= \Psi_n - r \left[\frac{\partial \Psi_n}{\partial r} \right]_{r=0}, \quad (n=1,2) \\ &= \frac{1}{2} r \int_0^r \left(1 - \frac{p^2}{r^2} \right) \zeta_n(p,t) dp. \end{aligned} \tag{5.45}$$

After a little more algebra it follows using (5.17), (5.18), (5.21) and (5.45) that

$$-(\mathbf{U}_a - \mathbf{c}) \cdot \nabla \zeta_s = \chi_1(r,t) \cos\lambda + \chi_2(r,t) \sin\lambda, \tag{5.46}$$

where

$$\begin{bmatrix} \chi_1(r,t) \\ \chi_2(r,t) \end{bmatrix} = \frac{1}{r} \frac{d\zeta_s}{dr} \times \begin{bmatrix} \psi_2'(r,t) \\ -\psi_1'(r,t) \end{bmatrix}. \tag{5.47}$$

Now using (5.46) and (5.47), Eq. (5.45) can be written as

$$\frac{d\zeta_{a1}}{dT} = \frac{1}{r} \frac{d\zeta_s}{dr} \left(\Psi_2'(r,t) \cos\lambda - \Psi_1'(r,t) \sin\lambda \right),$$

where d/dt denotes integration following a fluid parcel moving in a circular path of radius r about the vortex centre with angular velocity $\Omega(r)$. It follows that

$$\zeta_{a1} = \frac{1}{r} \frac{d\zeta_s}{dr} \int_0^t [\Psi_2'(r,t') \cos\lambda(t') - \Psi_1'(r,t') \sin\lambda(t')] dt',$$

where $\lambda(t') = \lambda - \Omega(r)(t - t')$. Using Eq. (5.45), this expression becomes

$$\zeta_{a1} = \frac{1}{2}\frac{d\zeta_s}{dr}\int_0^t\int_0^r\left(1 - \frac{p^2}{r^2}\right)\times[\zeta_2(p,t')\cos\lambda(t') - \zeta_1(p,t')\sin\lambda(t')]\,dpdt',$$

and it reduces further on substitution for ζ_n from (5.14) and the above expression for $\lambda(t')$ giving

$$
\begin{aligned}
\zeta_{a1} \quad = \quad & \frac{1}{2}\beta\frac{d\zeta_s}{dr}\int_0^r p\left(1 - \frac{p^2}{r^2}\right) \\
& \times \quad \int_0^t[\cos\{\lambda - \Omega(r)(t - t')\} - \cos\{\lambda - \Omega(r)(t - t') - \Omega(p)t'\}]dt'dp.
\end{aligned}
$$

On integration with respect to t' we obtain

$$\zeta_{a1}(r,\theta,t) = \zeta_{11}(r,t)\cos\lambda + \zeta_{12}(r,t)\sin\lambda \tag{5.48}$$

where

$$
\begin{aligned}
\zeta_{1n}(r,t) \quad = \quad & \int_0^t \chi_n(r,t)dt \\
= \quad & -\frac{1}{2}\beta\frac{d\zeta_s}{dr}\int_0^r p\left(1 - \frac{p^2}{r^2}\right)\eta_n(r,p,t)dp, \tag{5.49}
\end{aligned}
$$

and

$$\eta_1(r,p,t) = \frac{\sin\{\Omega(r)t\}}{\Omega(r)} - \frac{\sin\{\Omega(r)t\} - \sin\{\Omega(p)t\}}{\Omega(r) - \Omega(p)}, \tag{5.50}$$

$$\eta_2(r,p,t) = \frac{1 - \cos\{\Omega(r)t\}}{\Omega(r)} + \frac{\cos\{\Omega(r)t\} - \cos\{\Omega(p)t\}}{\Omega(r) - \Omega(p)}, \tag{5.51}$$

The integrals in (5.50) can be readily evaluated using quadrature.

Chapter 6

VORTEX ASYMMETRIES, VORTEX WAVES

Observations of tropical cyclones indicate that storms that may be closely approximated as axisymmetric are rare - such storms tend to be the most intense and then it is usually only the inner core region that is approximately axisymmetric. The outer region of storms is invariably asymmetric, and weaker storms are usually highly asymmetric. In the previous chapter we saw how vortex asymmetries, whether they are considered a part of the vortex or a part of its environment, can influence the vortex motion.

In the following section we study the motion of initially asymmetric vortices on an f-plane. The issues to be addressed are relevant to the problem of initializing tropical cyclone forecast models as well as to an understanding of possible track changes as cyclones develop new asymmetries or as existing asymmetries evolve.

Asymmetries have implications not only for tropical cyclone motion, but also for intensification. The processes involved are intimately tied up with wave motions. Therefore in later sections we examine the dynamics of waves on vortices.

6.1   Axisymmetrization

We construct an asymmetric vortex by adding a vortex dipole to the initial vorticity distribution shown in Fig. 5.11. The vortex dipole has the form

$$\zeta_d(r, \lambda) = \zeta_D(r/d)^2 exp(-r^2/d^2)cos(\lambda - \alpha), \tag{6.1}$$

where ζ_D, d and α are prescribed constants characterizing the dipole strength, scale and orientation. Thus the vorticity maximum and minimum of the dipole occur at (d, α) and $(d, \pi + \alpha)$, respectively.

We consider four calculations with $\alpha = 0$ so that the dipole is oriented west-east. In the first calculation, S1, $d = \sqrt{2}$ and $\zeta_D = 0.2\zeta_o$, the latter being the maximum value of zeta in the symmetric vortex. In the second calculation, S2, $d = 2\sqrt{2}$ and $\zeta_D = 0.1\zeta_o$ so that the velocity at the origin associated with the dipole is the same as

in S1[1]. These two calculations are carried out on an f-plane. The third and fourth calculations, S3 and S4, are the same as S1 and S2, but are for a β-plane. The calculations are carried out numerically by a direct integration of Eq. 5.1 with the initial vorticity distribution (symmetric vortex plus dipole) described above. The Kasahara-Platzman partitioning scheme is used to analyzing the subsequent vortex evolution so that the asymmetric component of the vortex is regarded as a part of the environment, even at the initial instant. Figure 6.1 shows the evolution of the asymmetric vorticity component and associated streamfunction at selected times for the calculations S1. It can be seen that within a circle of radius about $2r_{max}$ centred on the vortex, the asymmetric vorticity field undergoes rapid distortion due to the relatively large shear of the tangential wind field in this region. For example, for the flow parameters chosen, the angular velocity of the symmetric vortex decreases monotonically with radius (see Fig. 5.3b) so that in 6 h an air parcel of 20 km radius completes approximately 2-4 revolutions compared with 1-4 revolutions at 100 km (i.e. r_{max}) and 0-5 revolutions at 200 km. Outside this circle, the distortion of the asymmetry proceeds more slowly. Initially, the asymmetric flow across the vortex is towards the south Fig. 6.1a, but its direction rotates counterclockwise with the gyres of the asymmetric streamfunction as the vorticity asymmetry is rotated. Therefore the vortex track forms a counterclockwise arc as shown in Fig. 6.2a.

As the asymmetric vorticity distribution is wound around the vortex by the angular shear of the tangential wind, the associated flow is reduced in strength and after about 12 h, the vortex essentially stalls. The reduction in strength of the asymmetric flow as the asymmetric vorticity field suffers angular shear can be understood in terms of an analytic solution for the problem in which the motion of the basic vortex is ignored. Then, in the same spirit as the calculation leading to (5.13), we can show that the asymmetric vorticity distribution at time t is given by

$$\zeta_a(r, \lambda, t) = \zeta_D(r/d)^2 exp(-r^2/d^2)cos(\lambda - \Omega(r)t). \tag{6.2}$$

For an unbounded domain, we can solve the Poisson equation for the associated streamfunction using 5.15. Using complex notation the velocity of the asymmetric flow across the vortex centre, $U_o + iV_o$, may be shown to have the form

$$U_o + iV_o = -i\zeta_D r_{\max} \int_0^\infty (\eta s)^2 \exp[-\eta^2 s^2 + i(V_{\max}t/r_{\max})\Omega'(s)]ds, \tag{6.3}$$

where $\eta = r_{max}/d$ and $\Omega'(s) = r_{\max}\Omega(r)/V_{\max}$. For large values of t (i.e. $t \geq r_{\max}/V_{\max} = 42$ min), the integrand in (6.3) oscillates rapidly. As t increases, these oscillations become more numerous and as a result of cancellation the integral itself decreases monotonically in value.

Figure 6.3 shows the evolution of the asymmetric vorticity field for calculation S2 and Fig 6.2b shows the vortex track in this simulation. As expected, since the asymmetry is concentrated at a larger radius than S1, it is less rapidly wound up

---

[1]See Smith *et al.* (1990), Appendix B, Eq. (B8)
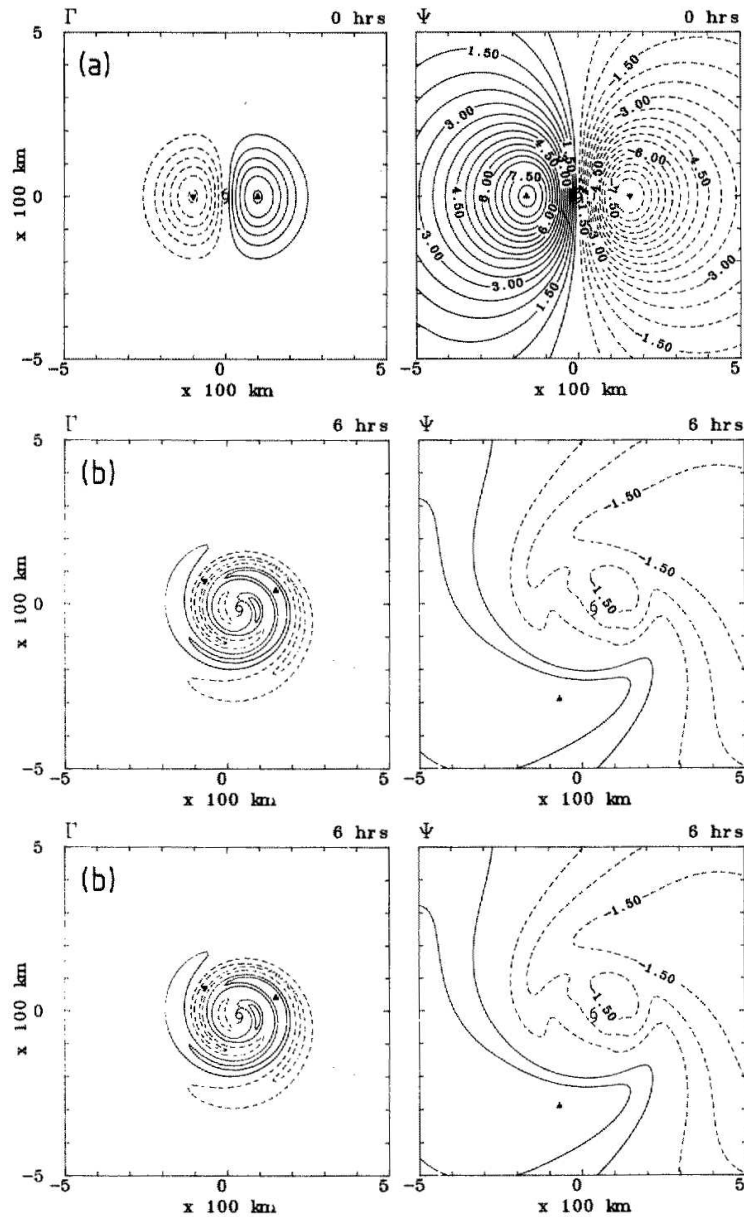
Figure 6.1: Evolution of the asymmetric vorticity field (ζ_a) and corresponding stream-function field for the initially asymmetric vortex on an f-plane in the case of small-scale asymmetry (calculation S1), Shown are (a) the initial fields, and the fields at (b) 6 h and (c) 12 h. Note that only one quarter of the total flow domain is shown. Contour intervals are 2×10^{-5} s^{-1} for ζ_a and 5×10^4 m^2 s^{-1} for ψ_a. Zero contours have been excluded.

by the radial shear of the basic vortex. Accordingly, the asymmetric component of flow across the streamfunction centre rotates less rapidly and decays less rapidly in strength. As a result, the vortex moves farther from its initial position than in S1
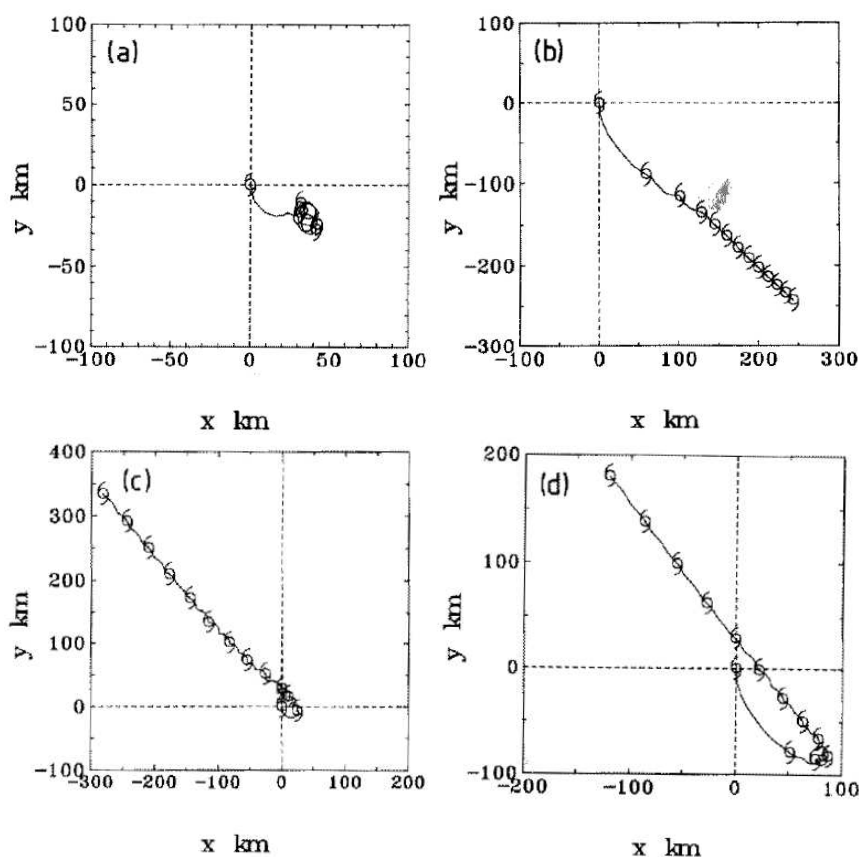
Figure 6.2: Tracks of initially asymmetric vortices in the calculations Sl to S4 defined in the text. (a) Small asymmetry, f-plane; (b) large asymmetry, f-plane; (c) small asymmetry, β-plane; and (d) large asymmetry, β-plane.

and its track rotates only slowly towards the east after the first three hours, As might be anticipated from the results of section 3.3.2. the effect of a nonzero beta would be to induce an east-west vorticity tendency in addition to the existing asymmetry. This is confirmed by the calculations S3 and S4, the vortex tracks for which are shown in panels (c) and (d) of Fig. 6.2. In S3 the vortex no longer stalls after 12 h, but recurves to move along a north-westwards track as the beta-induced asymmetries begin to dominate. In S4, the beta effect becomes important also, but not so rapidly, and again the track turns north-westwards as it does so. These calculations show that the importance of vortex asymmetry on the track depends strongly on the scale of the asymmetry. The larger this scale, the less rapidly can the asymmetry be wound up by the vortex circulation and the more persistent is the effect of the asymmetry. It is evident that initial asymmetries concentrated outside the radius of maximum tangential wind can have a significant effect on subsequent vortex positions and would need to be resolved or somehow represented in tropical-cyclone forecast models.

The asymmetries we investigated analytically in Chapter 5 were associated wholly
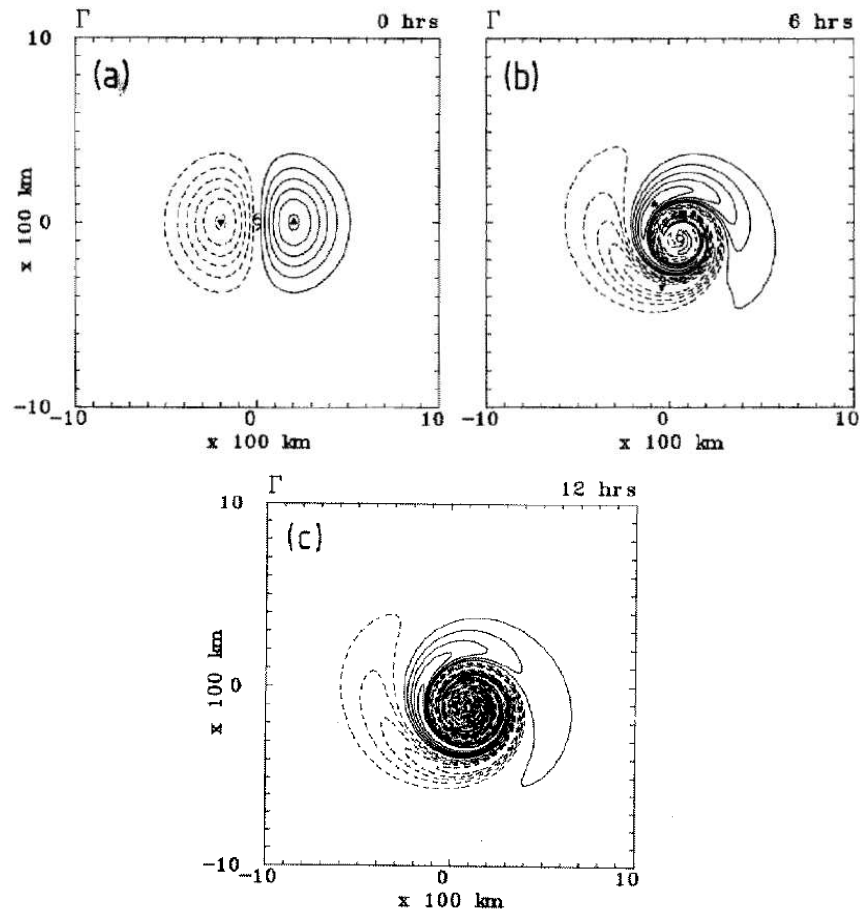
Figure 6.3: Evolution of the asymmetric vorticity field (Γ) for the initially asymmetric vortex on an f-plane in the case of large-scale asymmetry (simulation S2). Shown are (a) the initial field, and the fields at (b) 6 h and (c) 12 h. Contour interval is 1×10^{-5} s^{-1}. Note: the domain size is twice that shown in Fig. 11. Zero contours have been excluded.

with advective processes since we made the assumption that to a first approximation, the vorticity perturbation is advected by the tangential velocity of the initial axisymmetric vortex. This assumption precludes the existence of waves that propagate on the vorticity gradient of the basic vortex. However, in some situations, wave motions may be important to the dynamics and in this section we review the pertinent aspects of waves on vortices. We begin with two-dimensional non-divergent inviscid flow on an f-plane as the prototype model and go on in later sections to examine waves in a shallow-water model.

6.2 Vortex Rossby waves

We consider here the linear theory of waves on a circular vortex in gradient balance. In a stationary cylindrical coordinate-system, the linearized vorticity-equation is

$$\left(\frac{\partial}{\partial t} + \frac{V}{r}\frac{\partial}{\partial \lambda}\right)\zeta' - \frac{1}{r}\frac{\partial \psi'}{\partial \lambda}\frac{d\bar{\zeta}_a}{dr} = 0, \tag{6.4}$$

where ψ' denotes the perturbation streamfunction, $\zeta' = \nabla^2\psi'$ is the perturbation vorticity, $V(r)$ the basic-state tangential velocity at radius r, and $\bar{\zeta}_a = f + (1/r)d(rV)/dr$ the basic-state absolute vorticity. If f is a constant, it does not appear explicitly in the problem. When (6.4) has been solved for ψ', the perturbation radial and azimuthal winds are obtained from

$$u' = -\frac{1}{r}\frac{\partial \psi'}{\partial \lambda}, \quad v' = \frac{\partial \psi'}{\partial r}. \tag{6.5}$$

The solution to (6.4) may be obtained by an azimuthal Fourier analysis. Let

$$\psi' = \hat{\psi}_n(r,t)e^{in\lambda},$$

where $\hat{\psi}_n(r,t)$ denotes the Fourier amplitude of the azimuthal wave-number n, and let $\Omega = V/r$ be the local angular rotation rate of the basic-state vortex. Then the linearized vorticity equation in Fourier space becomes

$$\left(\frac{\partial}{\partial t} + in\Omega\right)\left[\frac{1}{r}\frac{\partial}{\partial r}\left(r\frac{\partial \hat{\psi}_n}{\partial r}\right) - \frac{n^2}{r^2}\hat{\psi}_n\right] - \frac{in}{r}\hat{\psi}_n\frac{d\bar{\zeta}_a}{dr} = 0. \tag{6.6}$$

Under certain circumstances n turns out to be complex, in which case there exist unstable solutions. It can be shown that a necessary condition for the existence of unstable solutions is that the radial gradient of the basic state vorticity, $d\bar{\eta}/dr$ changes sign somewhere within the flow. We defer consideration of the unstable case until **subsection 4.x.y**.

A formal solution to the general initial value problem for Eq. (6.6) may be obtained using Laplace transform techniques. The Laplace transform of an arbitrary function $\chi(r,t)$ is defined by

$$\hat{\chi}(r,s) = \int_0^\infty e^{-st}\chi(r,t)dt, \tag{6.7}$$

and if $\hat{\chi}(r,s)$ is known, the inverse transform is obtained as a contour integral in the complex plane:

$$\chi(r,t) = \frac{1}{2\pi i}\int_{c-i\infty}^{c+i\infty} e^{st}\hat{\chi}(r,s)dt, \tag{6.8}$$

where c is a constant so that the contour of integration in the complex s-plane lies to the right of all singularities of $\hat{\chi}(r,s)$. It is easy to show that the Laplace transform

of $\partial\chi/\partial t$ is $s\hat{\chi}(r,s) - \chi(r,0)$ and it follows that the Laplace transform of Eq. (6.6) satisfies the ordinary differential equation

$$(s + in\Omega(r)) \left[\frac{1}{r}\frac{\partial}{\partial r}\left(r\frac{\partial}{\partial r}\right) - \frac{n^2}{r^2} \right] \hat{\psi}(r,s) - in\frac{d\bar{\eta}}{dr}\hat{\psi}(r,s) = \left[\frac{1}{r}\frac{\partial}{\partial r}\left(r\frac{\partial}{\partial r}\right) - \frac{n^2}{r^2} \right] \psi(r,0)$$

(6.9)

Dividing by $s + in\Omega(r)$ and noting that the right-hand-side of (6.9) is the initial **vorticity** $\hat{\zeta}_o$ of the n-th Fourier component, we obtain

$$\left[\frac{1}{r}\frac{\partial}{\partial r}\left(r\frac{\partial}{\partial r}\right) - \frac{n^2}{r^2} \right] \hat{\psi}(r,s) - in\frac{d\bar{\eta}}{dr}\frac{\hat{\psi}(r,s)}{(s + in\Omega(r))} = \frac{\zeta(r,0)}{(s + in\Omega(r))} \qquad (6.10)$$

In principle, when this equation has been solved for $\hat{\psi}(r,s)$, the inverse transform must be obtained for $\psi(r,t)$. The transform involves the evaluation of contour integrals in the complex plane. From the calculus of residues we know that the general solution consists of a sum of discrete exponentials (or normal modes) associated with the zeros of the Wronskian together with an integral along branch cuts associated with the zeros of $(s + in\Omega(r))$ that characterizes the continuous spectrum. Explicit solutions have been obtained only in a few special cases, but an examination of these cases is instructive.

Case I: Bounded Rankine vortex: $V = \Gamma/r$, $\quad \Omega = \Gamma/r^2$, $\quad \Gamma = $ constant, $a \leq r \leq b$. In this case $d\bar{\zeta}_a/dr = 0$ and Eq. (6.6) becomes

$$\left(\frac{\partial}{\partial t} + \frac{in\Gamma}{r^2} \right) \left[\frac{1}{r}\frac{\partial}{\partial r}\left(r\frac{\partial\hat{\psi}_n}{\partial r}\right) - \frac{n^2}{r^2}\hat{\psi}_n \right] = 0. \qquad (6.11)$$

The inverse Laplace transform of (6.11) is

$$\left[\frac{\partial}{\partial r}\left(r\frac{\partial}{\partial r}\right) - \frac{n^2}{r} \right] \psi(r,t) = r\zeta(r,0)e^{-iant/r^2}. \qquad (6.12)$$

The solution of this equation in the domain $a \leq r \leq b$ is

$$\psi(r,t) = \int_a^b G(r,x)\zeta(r,0)e^{-iant/x^2}xdx, \qquad (6.13)$$

where the Green's function is given by

$$G(r,x) = \frac{1}{2nr^n(a^{2n} - b^{2n})} \begin{cases} (x^n - b^{2n}x^{-n})(a^{2n} - r^{2n}), & a \leq r \leq x \\ (x^n - a^{2n}x^{-n})(b^{2n} - r^{2n}), & x \leq r \leq b \end{cases} \qquad (6.14)$$

Finally, the Fourier inversion for wavenumber n is

$$\psi_n(r,\lambda,t) = e^{in\lambda} \int_a^b G(r,x)\zeta(r,0)e^{-iant/x^2}xdx. \qquad (6.15)$$
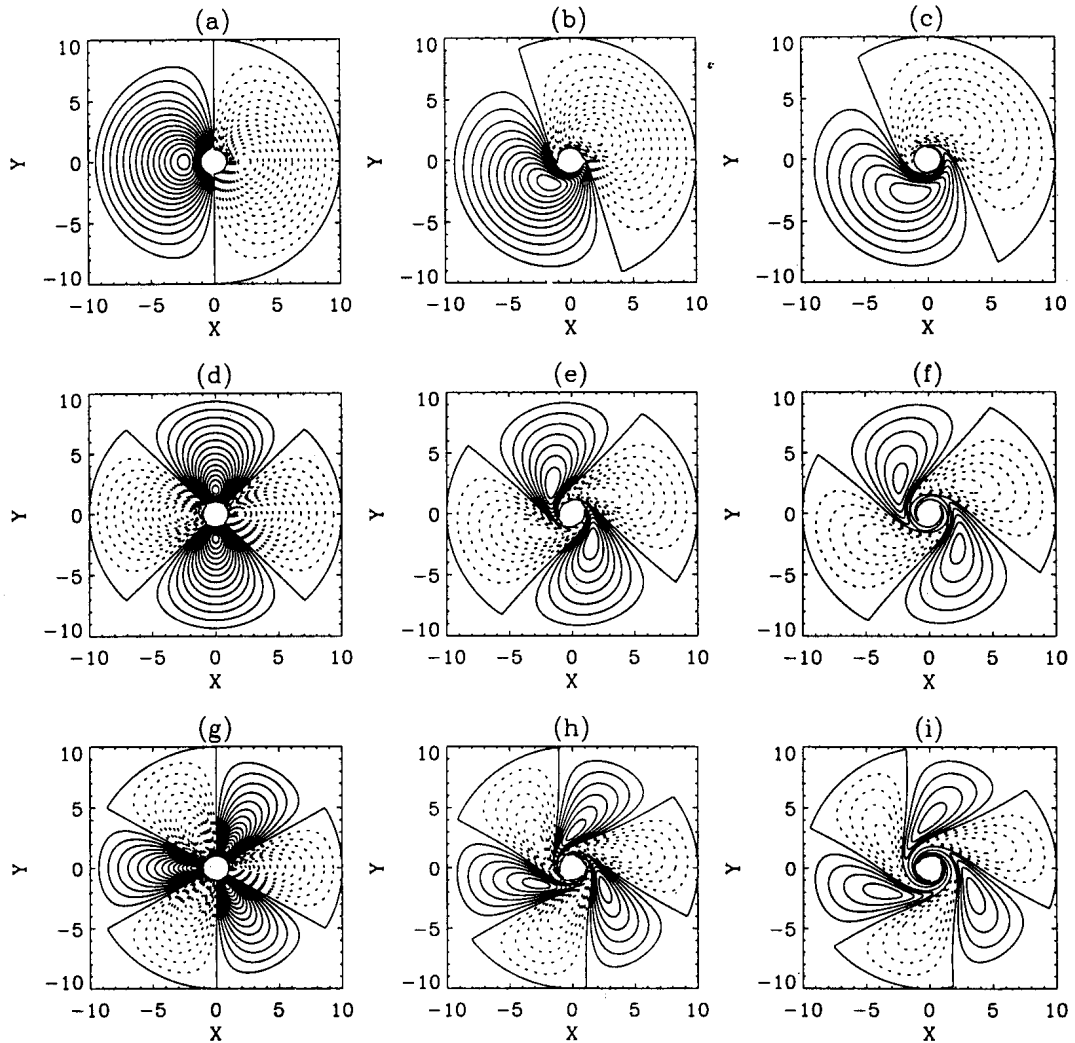
Figure 6.4: Perturbation streamfunction field for $\zeta(r,0) = 1/r^3$ for the hounded Rankine vortex in the region $a = 1, b = 10$. The columns show contours at times $t = 0$, $t = 3.6$ and $t = 7.2$, respectively. Panels (a)-(c) show contours for $n = 1$ where the contour interval is 1.1×10^{-2}. Panels (d)-(f) show contours for $n = 2$ where the contour interval it 5.67×10^{-3}. Panels (g)-(i) show contours for $n = 3$ where the contour interval is 3.31×10^{-3}.

Some solutions for various initial distributions of $\zeta(r,0)$ and n are given by Smith and Montgomery (1995). Figure 6.4 shows shows the streamfunction fields for an upright distribution of initial vorticity $\zeta(r,0) = 1/r^3$ and Fig. 6.5 shows the corresponding vorticity fields. The rows represent wavenumbers $n = 1, 2$ and 3 respectively, while the columns designate times $t = 0$, $t = 3.6$ and $t = 7.2$, respectively. These figures show how the initial disturbances are sheared out preferentially in the inner region of the vortex by the large angular shear of the vortex. However, unlike

in the calculations in Chapter 5, wave dynamics are involved on account of the term $u(d\bar{\eta}/dr)$ that is retained at first-order in Eq. (6.4). The solutions are cylindrical analogues of plane-wave solutions describing sheared disturbances in rectangular simple shear flow (see e.g. Smith and Montgomery, 1995). Physically pertinent properties of these solutions, such as the dependence of integrated kinetic energy on azimuthal wave-number, are examined by Smith and Montgomery *op. cit.*.
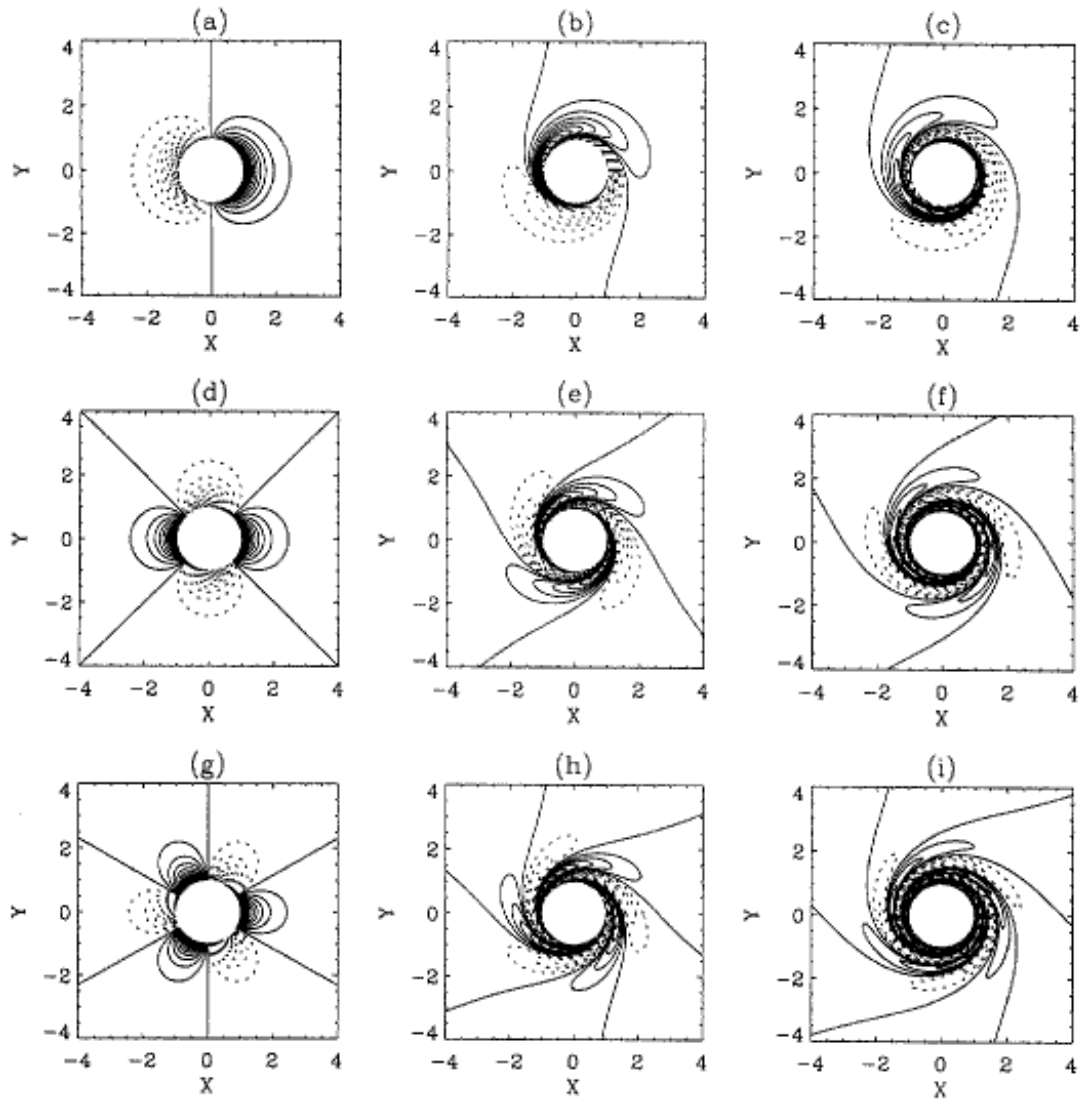
Figure 6.5: Perturbation vorticity-field corresponding to Fig. 6.4. The contour interval is 6.9×10^{-2}.

Case II: Unbounded Rankine vortex: $\bar{\zeta}_a$ discontinuous at $r = r_{max}$

The Rankine vortex is defined by the profile

$$V(r) = \begin{cases} r/a, & r \le a, \\ a/r, & a \le r, \end{cases} \qquad (6.16)$$

where a is the radius of maximum winds. The corresponding profile of basic-state vorticity is

$$\bar{\zeta}(r) = \begin{cases} 2/a, & r < a, \\ 0, & a < r, \end{cases} \qquad (6.17)$$

The profile of absolute vorticity is

$$\bar{\zeta}_a(r) = \begin{cases} Ro^{-1} + 2/a, & r < a, \\ Ro^{-1}, & a < r, \end{cases} \qquad (6.18)$$

where Ro is the Rossby number $= V_m/R_m$. The discontinuity in the mean-state vorticity at $r = a$ effectively introduces another boundary to the system. Since this boundary lies in the interior of the fluid, kinematic and dynamic boundary conditions must be satisfied at the disturbed interface $r = a + \eta$, where η is the interface displacement. The kinematic boundary condition requires that the normal velocity be continuous at $r = a + \eta$ while the dynamic boundary condition requires that the pressure be continuous at this radius. Consistent with the linearization of the equations, the matching conditions can be evaluated at $r = a$. Once u is determined, the evolution of the disturbed interface may be found by integrating

$$\left(\frac{\partial}{\partial t} + \frac{V}{r} \frac{\partial}{\partial \lambda} \right) \eta = u \qquad (6.19)$$

for η at $r = a$.

For the full Rankine vorticity profile (6.17) the linearized vorticity equation (6.4) is modified to

$$\left(\frac{\partial}{\partial t} + \frac{V}{r} \frac{\partial}{\partial \lambda} \right) \zeta = 0 \quad r \ne a. \qquad (6.20)$$

To solve (6.20), the discontinuity in the basic-state vorticity at $r = a$ must be accounted for. Since the problem is linear, the superposition principle may be used to separate the solution into two parts by letting $\zeta = \zeta_s + \zeta_1$, where ζ_s is defined to be smooth for all r and ζ_1 accounts for the discontinuity in the basic-state vorticity at $r = a$. The vorticity equation (6.20) is then split into two parts

$$\left(\frac{\partial}{\partial t} + \frac{V}{r} \frac{\partial}{\partial \lambda} \right) \zeta_s = 0 \quad \forall r \qquad (6.21)$$

$$\left(\frac{\partial}{\partial t} + \frac{V}{r} \frac{\partial}{\partial \lambda} \right) \zeta_1 = 0 \quad r \ne a. \qquad (6.22)$$

Equation (6.21) is formally identical to the system solved in Case I, but with the boundary conditions cited above. The corresponding solution in Fourier space is

$$\hat{\psi}_s(r,t) = \int_0^\infty G(r,\rho)\hat{\zeta}_{s0}(\rho)e^{-inV/\rho}\rho d\rho \tag{6.23}$$

where the appropriate Green's function is

$$G(r,t) = -\frac{1}{2n}\begin{cases} \rho^{-n}r^n, & 0 \le r \le \rho \\ \rho^n r^{-n}, & \rho \le r \le \infty \end{cases} \tag{6.24}$$

and $\hat{\zeta}_{s0}(\rho)$ is the smooth component of $\hat{\zeta}$ throughout the vortex at time $t = 0$.

The Fourier-space equivalent to (6.22) is

$$\left(\frac{\partial}{\partial t} + \frac{inV}{r}\right)\hat{\zeta}_1 = 0, \quad r \ne a. \tag{6.25}$$

Anticipating that the solution to (6.25) will yield the discrete normal modes which are irrotational on both sides of the mean-state vorticity discontinuity, $\hat{\zeta}_1$ is assumed to be separable and of the form

$$\hat{\zeta}_1 = \gamma(t)\delta(r-a). \tag{6.26}$$

Here, γ is an undetermined temporal multiplier for $\hat{\zeta}_1$, and $\delta(r-a)$ is the Dirac delta function. In terms of the perturbation streamfunction, (6.26) becomes

$$\nabla^2\hat{\psi}_1 = \gamma(t)\delta(r-a). \tag{6.27}$$

The streamfunction is also assumed to be separable and of the form $\hat{\psi}_1 = \gamma(t)\hat{\Psi}_1(r)$. Thus, (6.27) becomes

$$\left(\frac{1}{r}\frac{d}{dr}\left(r\frac{d}{dr}\right) - \frac{n^2}{r^2}\right)\hat{\Psi}_1 = \delta(r-a). \tag{6.28}$$

For $r \ne a$, (6.28) is Euler's equation. Two conditions are needed to match the solutions in each region across $r = a$. The first is the kinematic boundary condition requiring that the radial velocity u be continuous at $r = a$. Consequently, the Fourier streamfunction-amplitude must be continuous across $r = a$. The second condition results from integrating (5.12) over a small interval that includes r = a. This yields the following jump condition for $\hat{\psi}_1$

$$\frac{d}{dr}\hat{\Psi}_1 r(a^+) - \frac{d}{dr}\hat{\Psi}_1 r(a^-) = 1. \tag{6.29}$$

Applying the boundary conditions, and the continuity and jump conditions at $r = a$, yields

$$\hat{\Psi}_1 = -\frac{1}{2n}\begin{cases} a^{-n}r^n, 0 \le r \le a \\ a^n r^{-n}, a \le r \le \infty, \end{cases} \tag{6.30}$$

To complete the derivation, γ must be determined. The remaining constraint is the dynamic boundary condition which requires that the pressure be continuous at $r = a$. In Fourier space, the azimuthal-momentum equation is given by

$$\frac{\partial \hat{v}}{\partial t} + \frac{inV}{r}\hat{v} + \bar{\eta}\hat{u} = -\frac{in}{r}\hat{p}. \tag{6.31}$$

Evaluating (6.31) on each side of $r = a$ and subtracting gives

$$\frac{\partial}{\partial t}\left(\hat{v}(a^+) - \hat{v}(a^-)\right) + \frac{in}{a}\left(\hat{v}(a^+) - \hat{v}(a^-)\right) - \frac{2}{a}\hat{u}(a) = 0. \tag{6.32}$$

In terms of the *total* streamfunction, equation (6.32) becomes

$$\frac{\partial}{\partial t}\left(\frac{\partial \hat{\psi}}{\partial r}(a^+) - \frac{\partial \hat{\psi}}{\partial r}(a^-)\right) + \frac{in}{a}\left(\frac{\partial \hat{\psi}}{\partial r}(a^+) - \frac{\partial \hat{\psi}}{\partial r}(a^-)\right) + \frac{2in}{a^2}\hat{\psi}(a) = 0. \tag{6.33}$$

Now, from the superposition principle, $\hat{\psi} = \hat{\psi}_s + \gamma\hat{\Psi}_1$, where ψ_s and its derivatives are everywhere smooth by construction. Since Ψ_1 is continuous but has a unit jump in its derivative across $r = a$, equation (6.33) simplifies to

$$\frac{d\gamma}{dt} + \frac{i}{a}(n-1)\gamma = -\frac{2in}{a^2}\hat{\psi}_s(a,t) \tag{6.34}$$

a first-order linear differential equation for γ. Upon multiplying through by integrating factor $\exp\{i(n-1)t/a\}$ and substituting for $\hat{\psi}_s(a,t)$, equation (6.34) becomes

$$\frac{d}{dt}(\gamma e^{i(n-1)t/a}) = -\frac{2in}{a^2}\int_0^\infty G(a,\rho)\hat{\zeta}_{s0}e^{\{i(n-1)/a - in\bar{v}/\rho\}t}\rho d\rho. \tag{6.35}$$

Integrating in time and then multiplying through by $\exp\{-i(n-1)t/a\}$ gives

$$\gamma(t) = -\frac{2n}{a}\int_0^\infty \frac{G(a,\rho)\hat{\zeta}_{s0}}{(n-1-an\bar{v}/\rho)}e^{-in\bar{v}/\rho}\rho d\rho + c_1 e^{-1(n-1)t/a} \tag{6.36}$$

where c_1 is the constant of integration at $t = 0$. Equation (6.36) then yields

$$\gamma(t) = -\frac{2n}{a}\int_0^\infty \frac{G(a,\rho)\hat{\zeta}_{s0}}{(n-1-an\bar{v}/\rho)}e^{-in\bar{v}t/\rho}\rho d\rho$$

$$+ \left(\gamma_0 + \frac{2n}{a}\int_0^\infty \frac{G(a,\rho)\hat{\zeta}_{s0}}{(n-1-an\bar{v}/\rho)}\rho d\rho\right)e^{-i(n-1)t/a} \tag{6.37}$$

where γ_0 is the initial amplitude of the normal-mode (Rossby) edge-wave associated with the radial vorticity-gradient of the Rankine vortex. The Fourier streamfunction-amplitude, $\hat{\psi}$, is thus

$$\hat{\psi} = \int_0^\infty G(r,\rho)\hat{\zeta}_{s0}e^{-in\bar{v}t/\rho}\rho d\rho$$

$$- \quad \frac{2n}{a}\hat{\Psi}_1 \int_0^\infty \frac{G(a,\rho)\hat{\zeta}_{s0}}{(n-1-an\bar{v}/\rho)} e^{-in\bar{v}t/\rho} \rho d\rho$$

$$+ \quad \hat{\Psi}_1 \left(\gamma_0 + \frac{2n}{a} \int_0^\infty \frac{G(a,\rho)\hat{\zeta}_{s0}}{(n-1-an\bar{v}/\rho)} \rho d\rho \right) e^{-i(n-1)t/a} \qquad (6.38)$$

where G is given by (eq4.23) and $\hat{\Psi}_1$ is given (eq4.29). To obtain the physical-space streamfunction, the inverse Fourier transform must be applied to (6.38).

Equation (6.38) may be given a simple interpretation. The first line may he identified with the continuous-spectrum solution and represents the unbounded analogue of the solution presented in Case I. The second line is a conversion term that transfers a portion of the kinetic energy from the continuous-spectrum solution into the discrete mode (third of the three terms on the right-hand side of (6.38)). Note that even with no normal-mode component initially, i.e. $\gamma_o = 0$, the continuous-spectrum solution always projects onto the normal mode at later times provided the integral does not vanish (sec Fig. 18; cf, Farrell, 1984). For $n \neq 1$, the discrete modes rotate more slowly than the vortex and represent retrogressing Rossby edge-waves at $r = a + \epsilon$. It may he shown that, in the absence of perturbation vorticity inside the radius of maximum winds, as $t \to \infty$ only the edge-wave component remains. In particular, the asymptotic solution for $n = 1$ is the non-rotating normal-mode associated with a translation of the basic-state vortex. On the other hand, for non-zero perturbation vorticity inside the radius of maximum winds, the asymptotic solution for $n = 1$ has an oscillatory component. In hurricanes, where the basic-state angular velocity has a small, but generally non-zero radial gradient inside the radius of maximum winds, as $t \to \infty$ the latter effect would probably be of little significance. At early times, however, the transient wavenumber-one component could produce a cycloidal track in the fully non-linear formulation.

Explicit solutions have been constructed for an unbounded Rankine-vortex, wherein $\bar{\eta}$ experiences a finite jump at the radius of maximum winds, but is otherwise uniform inside and outside this radius (section 5 of Smith and Montgomery 1995). In this model the solution is a superposition of shear-wave (continuous spectrum) components and Rossby edge-wave (discrete spectrum) components that propagate azimuthally, at a slower speed than the vortex. However, because these waves do not propagate radially, they are not able to transport energy out of the vortex core.

Case III: Unbounded Rankine vortex: $\bar{\zeta}_a$ has multiple discontinuities

An extension of the unbounded-vortex model of SM allows multiple discontinuities in $\bar{\zeta}$. With more than one discontinuity, interference effects can arise. As an example, consider the simplest case of a three-region model in which the innermost vorticity $\bar{\zeta}_1$, is greater than the intermediate vorticity $\bar{\zeta}_2$, which is greater than the outermost vorticity $\bar{\zeta}_3$. Such a distribution can be regarded physically as a three-region approximation of a vortex monopole (or hurricane) possessing a finite transition region between its rapidly rotating core and its slowly rotating environment. Because the
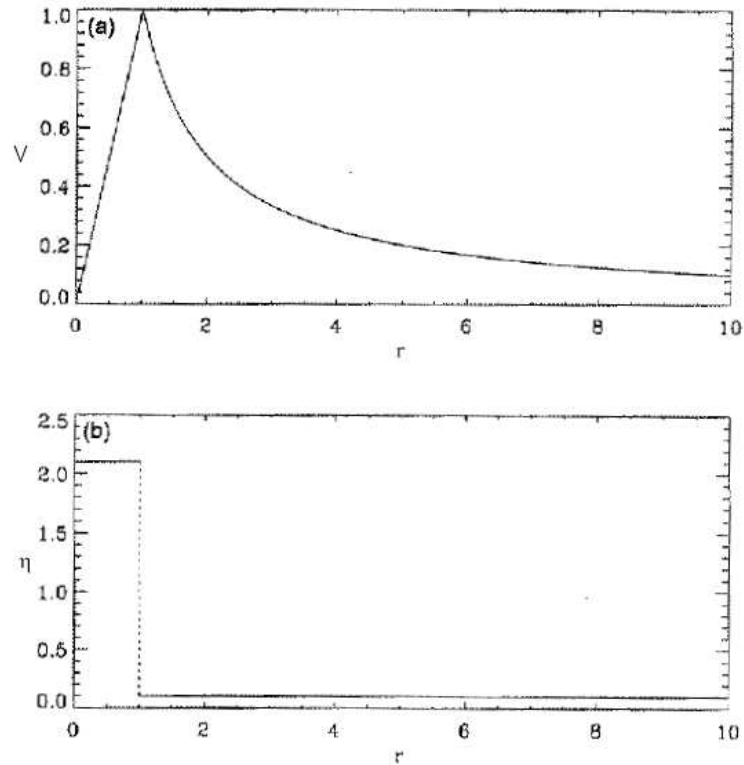
Figure 6.6: (a) Symmetric tangential winds V; for the full Rankine vortex; (b) corresponding absolute vorticity using an inverse Rossby number of 0.1.

generalized radial gradient of vorticity is non-positive, the vortex is exponentially stable. If the initial condition consists of no exterior edge-wave, but consists of smooth disturbance-vorticity in $r_1 \leq r \leq r_2$, some portion of the energy of the initial disturbance may be permanently transferred to the exterior edge-wave. Sheared disturbances play an essential role in this transfer process, for without them the disturbance energy as $t \rightarrow \infty$ resides solely in the interior edge-wave. Keeping the limitations of the three-region model in mind, we expect that the continuous model may possess an analogous mechanism for transferring energy outwards.

6.3 Free waves on a resting basic state

The following discussion is based on that of Montgomery and Lu (1997). We consider small-amplitude waves in rotating shallow layer of water. If the curvature of the free surface is neglected, the linearized shallow-water equations in cylindrical coordinates on an f-plane are

$$\frac{\partial u'}{\partial t} - fv' + g\frac{\partial h'}{\partial r} = 0, \tag{6.39}$$
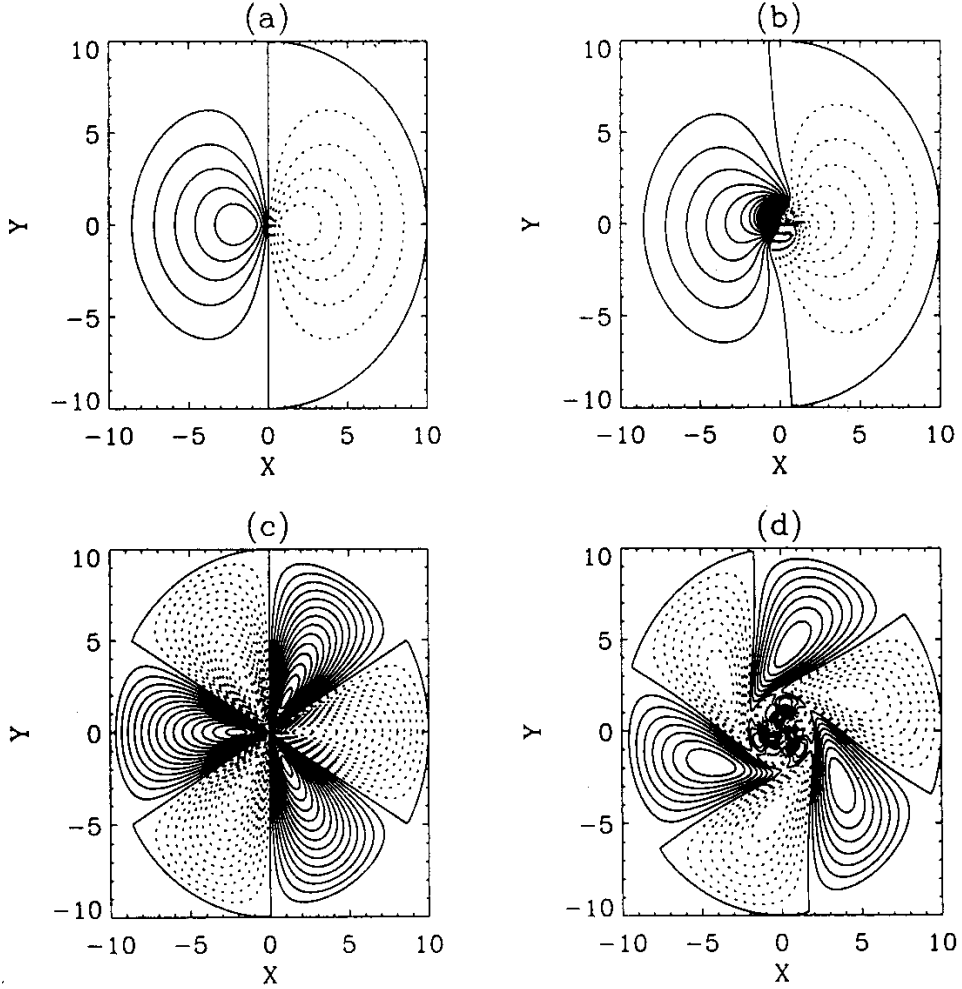
Figure 6.7: Perturbation streamfunction forced by initial vorticity-profile $\zeta_o = 1/(r+1)^3$. Panels (a) and (b) are for wave number $n = 1$ and the contour interval is 1.59×10^{-2}. Panels (c) and (d) are for $n = 3$ and the contour interval is 1.06×10^{-3} The columns are for times $t = 0.0$ and $t = 7.2$, respectively. Solid lines denote $\psi \geq 0$; dotted lines denote $\psi \leq 0$.

$$\frac{\partial v'}{\partial t} + fu' + \frac{g}{r}\frac{\partial h'}{\partial \lambda} = 0, \qquad (6.40)$$

$$\frac{\partial h'}{\partial t} + H\left(\frac{1}{r}\frac{\partial}{\partial r}(ru') + \frac{1}{r}\frac{\partial v'}{\partial \lambda}\right) = 0. \qquad (6.41)$$

Here, H is the depth of the fluid at rest, h' is surface-height perturbation, and (u', v') are perturbation radial and tangential winds, respectively.

The flow domain is the circular region $0 \le r \le a$. Perturbation quantities are assumed finite at $r = 0$, while the height perturbation is assumed to vanish at $r = a$. The latter condition is chosen in preference to a vanishing radial velocity at $r = a$ since the limit $a \to \infty$ corresponding to the unbounded domain is obtained most simply.

Free wave solutions of Eqs. (6.39)-(6.41) are obtained by substituting

$$(u', v', h') = (\hat{u}(r), \hat{v}(r), \hat{h}(r)) \exp[n\lambda - \omega t], \tag{6.42}$$

where n denotes the azimuthal wavenumber and ω the wave frequency. In azimuthal-Fourier space the linearized disturbance equations (6.39)-(6.41) can be written as a matrix equation

$$\begin{pmatrix} \omega & f & -g\frac{d}{dr} \\ f & \omega & -n\frac{g}{r} \\ \frac{H}{r}\frac{d}{dr}r & -\frac{nH}{r} & \omega \end{pmatrix} \begin{pmatrix} i\hat{u} \\ \hat{v} \\ \hat{h} \end{pmatrix} = 0, \tag{6.43}$$

which possesses three sets of solutions. The first set corresponds to steady geostrophic, flow ($\omega = 0$) in which the Coriolis force is balanced by the pressure gradient force,

$$f\hat{v} = g\frac{\partial \hat{h}}{\partial r}, \tag{6.44}$$

$$f\hat{u} = -\frac{in}{r}g\hat{h}. \tag{6.45}$$

Here, $g\hat{h}/f$ is a streamfunction for the geostrophic wind. The amplitudes of the vorticity ($\hat{\zeta}$) and potential vorticity ($\hat{P}$) are given by

$$\hat{\zeta} = \frac{d}{rdr}(r\hat{v}) - \frac{in}{r}\hat{u} = \frac{g}{f}\hat{\nabla}^2\hat{h}, \tag{6.46}$$

$$\hat{P} = \frac{\hat{\zeta}}{H} - f\frac{\hat{h}}{H^2} = \frac{g}{fH}\left(\hat{\nabla}^2\hat{h} - \gamma^2\hat{h}\right), \tag{6.47}$$

where $\hat{\nabla}^2 = (1/r)(d/dr)(rd/dr) - n^2/r^2)$ is the horizontal Laplacian in azimuthal-Fourier space and $\gamma^2 = f^2 - f^2gH$ is the inverse square of the Rossby radius of deformation. For isolated disturbances, $\hat{\zeta}$ and $\hat{P}$ are anti-correlated with $\hat{h}$.

If the parabolic free surface associated with the rotating annulus is neglected in Eqs. (6.39)-(6.41), the geostrophic modes become Rossby waves (see DM, Chapter 11). For small free-surface slopes, these waves retrogress in the rotating frame possess small frequencies compared to the rotation frequency, and are well described by quasi-geostrophic dynamics. The Rossby wave vorticity and PV are again anti-correlated with the height

$$\zeta' \propto -h',$$
$$P' \propto -h'. \tag{6.48}$$

Superposing the geostrophic and isallobaric winds shows that the total wind lags the height contours. The propagation of a monochromatic Rossby wave around the annulus can then be interpreted as an adjustment process whereby wind adjusts to mass,

$$\text{wind} \to \text{mass}, \tag{6.49}$$

where mass represents the perturbation height and wind represents the total perturbation wind.

Define $\beta_{eff} = f/H d/H/dr$. Then the local dispersion relation for topographic Rossby waves in an annulus takes the form

$$\omega = \frac{\frac{n}{r}\beta_{eff}}{k^2 + \frac{n^2}{r^2} + \frac{f^2}{gH}}, \tag{6.50}$$

where ω is wave frequency and k is radial wavenumber. For sufficiently small free-surface slopes, Rossby waves possess frequencies smaller than f therefore

$$\sigma^2 < f^2. \tag{6.51}$$

Substituting (2.36) xxxx into (??) yields

$$L^2 < \frac{c^2}{f^2}. \tag{6.52}$$

where $L = r/n$, the characteristic azimuthal length scale for azimuthal wavenumber n, and $c = \sigma r/n$, the azimuthal Rossby wave phase speed. Because (6.52) is formally identical to Rossby's adjustment criterion for balanced flow, it suggests a useful interpretation of linearized Rossby wave dynamics. Rewriting (6.52) yields

$$\frac{L^2}{c^2} > \frac{1}{f^2}, \tag{6.53}$$

indicating that if the wave timescale is sufficiently long the Coriolis force can effectively rotate the wind vectors, and thus wind adjusts to mass. Such wave disturbances are regarded as balanced and are customarily identified with **the slow manifold**.

Returning to the constant depth model (??), the second and third solutions are unsteady ($\sigma \neq 0$). In this case, (??) may he solved by eliminating winds in favor of height yielding a simplified Tidal equation

$$\frac{d^2\hat{h}}{dr^2} + \frac{1}{r}\frac{d\hat{h}}{dr} + \left(\kappa^2 - \frac{n^2}{r^2}\right)\hat{h} = 0, \tag{6.54}$$

where κ represents the eigenvalue for azimuthal wave-number n. The frequency σ is determined from dispersion relation for gravity-inertia waves (Poincaré waves),

$$\sigma^2 = f^2 + \kappa^2 gH. \tag{6.55}$$

Solutions to (2.12) that are bounded at $r = 0$ are given bv

$$\hat{h}(r) = AJ_n(\kappa r), \tag{6.56}$$

where J_n is the Bessel function of the first kind of order n and A is an arbitrary amplitude. The outer boundary condition $\hat{h}(a) = 0$ furnishes discrete eigenvalues $(\kappa; j = l, 2, \ldots)$ for each azimuthal wavenumber n. the dispersion relation (2.13) then yields a positive and negative frequency for each j. As a is increased, so as to better approximate an unbounded domain, the eigenfrequencies (2.13) become more closely spaced and ultimately approach a twofold continuum as $a \to \infty$. Nonaxisymmetric modes ($n = 1, 2, \ldots$) with $\sigma > 0$ propagate around the origin in a counterclockwise sense, (progress relative to f), while nonaxisymmetric modes with $\sigma < 0$ propagate around the origin in a clockwise sense (retrogress relative to f). Velocity amplitudes follow from the polarization relations

$$i\hat{u} = \frac{\left(\frac{-nf}{r}g\hat{h} + \sigma g\frac{d\hat{h}}{dr}\right)}{\sigma^2 - f^2}, \tag{6.57}$$

$$\hat{v} = \frac{\left(\frac{-n\sigma}{r}g\hat{h} + fg\frac{d\hat{h}}{dr}\right)}{\sigma^2 - f^2}. \tag{6.58}$$

On making use of (2.12), the PV amplitude is then

$$
\begin{aligned}
\hat{P} &= \frac{\hat{\zeta}}{H} - f\frac{\hat{h}}{H^2} \\
&= \frac{-gf}{H(\sigma^2 - f^2)}\left\{\hat{\nabla}^2\hat{h} + \kappa^2\hat{h}\right\} = 0
\end{aligned} \tag{6.59}
$$

Gravity-inertia waves are thus invisible on PV maps and vorticity is correlated with height

$$\zeta' \propto h'. \tag{6.60}$$

For gravity waves, a rising (fallilig) free-surface follows convergent (divergent) flow and so to wind

$$\text{mass} \to \text{wind}. \tag{6.61}$$

Gravity-inertia waves always possess frequencies greater than f thus

$$\sigma^2 > f^2, \tag{6.62}$$

implying

$$\frac{L^2}{c^2} < \frac{1}{f^2}, \tag{6.63}$$

where again $L = R/n$; yet $c = \sigma r/n$ the azimuthal gravity-inertia wave phase speed. In contrast to Rossby waves, (3.1) indicates if the wave timescale is sufficiently short, the, Coriolis force has too little time to rotate the wind vectors and hence mass adjusts to wind. Such wave disturbances are regarded as unbalanced and are customarily identified with the fast manifold.

The geostrophic and gravity-inertia wave solutions constitute a complete basis for the linear problem Eqs. (**??**)-(**??**) from which an arbitrary initial condition in the height and/or velocity field may be represented and evolved forward in time.

6.4 Free waves on barotropic vortices

6.4.1 Disturbance equations

Having reviewed the free waves on a resting fluid layer, we now investigate the free waves on a circular vortex in gradient balance

$$fv + \frac{v^2}{r} = g\frac{dh}{dr}, \tag{6.64}$$

where $v = v(r)$ denotes the basic-state tangential wind and $\overline{h} = \overline{h}(r)$ the basic-state free surface height. For small-amplitude disturbances on a stationary vortex, the linearized f-plane momentum and continuity equations are, respectively,

$$\left(\frac{\partial}{\partial t} + \frac{v}{r}\frac{\partial}{\partial \lambda}\right)u' - \left(f + \frac{2v}{r}\right)v' + g\frac{\partial h'}{\partial r} = 0, \tag{6.65}$$

$$\left(\frac{\partial}{\partial t} + \frac{v}{r}\frac{\partial}{\partial \lambda}\right)v' + \left(f + \frac{d}{rdr}(rv)\right)u' + g\frac{\partial h'}{r\partial \lambda} = 0, \tag{6.66}$$

$$\left(\frac{\partial}{\partial t} + \frac{v}{r}\frac{\partial}{\partial \lambda}\right)h' + \overline{h}\left(\frac{\partial}{r\partial r}(ru') + \frac{\partial v'}{r\partial \lambda}(rv)\right) + u'\frac{d\overline{h}}{dr} = 0. \tag{6.67}$$

The modal ansatz

$$(u', v', h') = [\hat{u}(r), \hat{v}(r), \hat{h}(r)]exp[i(n\lambda - \sigma t)] \tag{6.68}$$

again yields a matrix equation

$$\begin{pmatrix} \hat{\sigma} & \tilde{f} & -g\frac{d}{dr} \\ \overline{\eta} & \hat{\sigma} & -g\frac{n}{r} \\ \frac{d}{rdr}[r\overline{h}(\ )] & -\frac{nh}{r} & \hat{\sigma} \end{pmatrix} \begin{pmatrix} i\hat{u} \\ \hat{v} \\ \hat{h} \end{pmatrix} = \begin{pmatrix} 0 \\ 0 \\ 0 \end{pmatrix}, \tag{6.69}$$

though now $\sigma = \sigma - n\Omega/r$ denotes the Doppler-shifted frequency, $\Omega(r) = v/r$ the mean angular velocity, $\overline{\eta} = f + d(rv)/dr$ the, absolute vertical vorticity, and $\tilde{f} = f + 2\Omega/r$ the modified Coriolis parameter. At $r = 0$, perturbation quantities are assumed to be finite and symmetry considerations require that $d\hat{h}/dr = 0$ for $n = 0$

(symmetric modes) and that $\hat{h} = 0$ for $n \neq 0$ (asymmetric modes). To retain the analog of the two-fold continuum of gravity-inertia waves derived in section 6.3, we require a vanishing perturbation height field as, $r \to \infty$.

6.5   The basic state: A PV inversion problem

Among the many vortex profiles that could be selected, this work-focuses on basic states representative of hurricanes. A distinguishing property of such vortices is the manner in which the azimuthally averaged tangential winds decay with radius in the near-vortex region. To maintain a quasi-steady state under the influence of quadratic surface drag, the near-surface tangential winds in the near-vortex region must decay approximately as the inverse square root of the radius (Riehl 1963. Pearce 1993). Although one may readily construct wind profiles that are consistent with this property and are furthermore inertially (centrifugally) stable, the vortex may still be susceptible to shear instability if the radial PV gradient changes sign. As our objective is to first elucidate the structure of neutral waves in hurricane-like vortices, we limit the $(\overline{v}, \overline{h})$ profiles to be descendants of PV profiles

$$\bar{P} = \frac{1}{\overline{h}} \left[f + \frac{1}{r} \frac{d(r\bar{v})}{dr} \right], \tag{6.70}$$

which decrease monotonically from the Storm center, are positive in the Northern Hemisphere (inertial stability), and exhibit the proper $\overline{v}$ decay in the near-vortex region. For vanishing disturbances at infinity monotonic PV pro guarantee shear stability in the asymmetric balance (AB) slow manifold (Montgomery and Shapiro 1995).

In defining the basic state, it proves convenient to introduce nondimensional variables indicated by an asterisk:

$$\overline{h} = H h^*, \quad r = R_m r^*, \quad \overline{v} 0 V_m v^*.$$

Here, H denotes the resting depth V_m the maximum tangential wind speed, and R_m the radius of maximum tangential winds. Differentiating (6.70) with respect to radius and substituting (6.64) furnishes the nondimensional invertibility problem for $\overline{v}(r)$,

$$\frac{d^2\bar{v}}{dr^2} + \left(\frac{1}{r} - \beta \right) \frac{d\bar{v}}{dr} - \left(\frac{1}{r^2} + \frac{\beta}{r} + \frac{F\bar{P}}{R^2} \right) \bar{v} - \frac{\bar{P}\bar{v}^2}{r} \frac{F}{R} = \frac{\beta}{R}, \tag{6.71}$$

where $\beta = 1/\overline{P} \cdot \overline{P}/dr$, a normalized basic-state PV gradient, $R = V_m/f R_m$ a Rossby number, and $F = V_m^2/gH$ a squared Froude number. In (6.71) asterisk have been dropped. Solutions are sought subject to the boundary conditions that $\overline{v}(0) = 0$ and that at sufficiently large radius the tangential wind decays as an equivalent point vortex with a deformation radius of $\sqrt{gH}/f$. Mathematically this latter condition

takes the form $\bar{v}(r)K_1(\sqrt{Fr}/R)$ for $\sqrt{Fr}/R \gg 1$, where K_1, is the modified Bessel function of the second kind of order one.

When $R \gg 1$, the nonlinearity of (6.71) prevents analytical solution. Denoting $\bar{v}_i = \bar{v}(r_i)$ where $r_i = i \cdot \sigma r$,

6.5.1 Wave-mean flow interaction

Here we investigate the effects of radially propagating vortex Rossby-waves on the mean vortex. Provided the amplitudes of the asymmetries remain small, the mean-flow changes at second order in disturbance amplitude can be obtained from the divergence of the eddy-momentum flux

$$\frac{\partial \bar{v}}{\partial t} = -\frac{1}{r^2}\frac{\partial}{\partial r}\overline{(r^2 u' v')} \qquad (6.72)$$

where $\bar{\phi}$ denotes azimuthal mean of ϕ. If the momentum flux vanishes after some time t, the change in the mean tangential wind follows on integrating (6.72)

$$\Delta \bar{v}(r) = -\int_0^\tau \frac{1}{r^2}\frac{\partial}{\partial r}\overline{(r^2 u' v')}dt. \qquad (6.73)$$

Although asymmetries cannot change the area-integrated angular-momentum and circulation, they can change local values of these quantities. An equally valid representation for the change in the mean tangential wind is given by the integrated radial flux of vorticity.

Chapter 7

MOIST PROCESSES

Review of Smith (2000)

7.1 Idealized modelling studies

History - Ooyama, Emanuel
    Papers with Hongyan

7.2 Other modelling studies

Rosenthal, Anthes, Kurihara Braun (2000)

Chapter 8

TROPICAL CYCLONE PREDICTION

Chapter 9

ADVANCED TOPICS

9.1 Vortex stiffness

Paper of Schubert and Hack

9.2 Potential Radius coordinates

9.3 Asymmetric balance theory

xxxx xxxx

Chapter 10

Appendices

10.1 Thermodynamics

Here are a few notes on important thermodynamic quantities. More details are to be found in Emanuel (1994).

10.1.1 Basic quantities

The specific enthalpy, k, is defined by $k \equiv u + p\alpha$, where u is the specific internal energy. For an ideal gas, $k = c_p T$. Then the first law of thermodynamics can be written

$$dq = dk - \alpha dp. \tag{10.1}$$

The specific enthalpy of a mixture of dry air, water vapour and liquid water is

$$k = k_d + r_v k_v + r_L k_L, \tag{10.2}$$

where k_d, k_v and k_L are the specific enthalpies of the components and r_v and r_L are the mixing ratios of water vapour and liquid water.

The latent heat is defined by

$$L_v(T) = k_v - k_L. \tag{10.3}$$

Then (10.2) may be written

$$k = k_d + L_v r + k_L r_T, \tag{10.4}$$

where r_T is the total water content. From the definitions of k_d and k_v, (10.4) becomes

$$k = (c_p d + r_T c_L)T + L_v r. \tag{10.5}$$

10.1.2   CAPE and CIN

The convective available potential energy of an air parcel lifted from a height z_i to its level of neutral buoyancy (LNB) is defined as

$$CAPE_i = \int_{z_i}^{LNB} F \cdot dl \,, \tag{10.6}$$

where $\mathbf{F}$ is the force per unit mass that acts on on the parcel and $\mathbf{dl}$ is a unit vector along the path of the displacement. In the case of upright convection, this may be written

$$CAPE_i = \int_{z_i}^{LNB} B dz \tag{10.7}$$

where z measures height (normal to geopotential surfaces) and B is the buoyancy force. Using (Check), we may write

$$CAPE_i = \int_{z_i}^{LNB} g \left(\frac{\alpha_p - \alpha_a}{\alpha_a} \right) dz \tag{10.8}$$

or assuming the environment to be in hydrostatic equilibrium,

$$CAPE_i = \int_{p_{LNB}}^{p_i} (\alpha_p - \alpha_a) \, dp \tag{10.9}$$

where p_i and $p_L NB$ are the pressures at the initial parcel level and its LNB, respectively. Finally, using the ideal gas law, (10.9) may be written

$$CAPE_i = \int_{p_{LNB}}^{p_i} R_d (T_{\rho p} - T_{\rho a}) \, d\ln p. \tag{10.10}$$

It follows that $CAPE_i$ is proportional to the area enclosed by the density temperature of the lifted parcel and that of the environment, respectively, on a thermodynamic diagram whose coordinates are linear in temperature and in $\log p$. $CAPE$ depends on the initial parcel, i, and on the thermodynamic process assumed in lifting the parcel. It can be defined only for those parcels that are positively buoyant somewhere on the sounding.

Another method of assessing stability is to plot a sounding on a thermodynamic diagram with a conserved state variable as one of the coordinates. A convenient choice is the saturation pseudoentropy, s_p^*, which is related to the saturation pseudoequivalent potential temperature, and is conserved following the pseudoadiabatic displacement of a saturated parcel. The density of the (unsaturated) environment may be approximated as a function of p and s_p^*. The approximation involves replacing the mixing ratio by its saturation value in the virtual temperature. Using (10.10) the parcel CAPE can be approximated in terms of p, s_p^* and r, as

$$CAPE_i = \int_{p_{LNB}}^{p_i} \frac{1}{1+r} \left\{ \left(\frac{\partial \alpha_d}{\partial s_p^*} \right)_{r,p} \left(s_{pp}^* - s_{pa}^* \right) + \left[\left(\frac{\partial \alpha_d}{\partial r^*} \right)_{s_p^*,p} - \alpha \right] (r_p - r_a) \right\} dp \tag{10.11}$$

where we have assumed that s_p^* and $r_p - r_a$ are reasonably small and have used the result that $\alpha = \alpha_d/(1+r)$[1]. If we neglect the direct effect of water substance on density, this can be further approximated as

$$CAPE_i = \int_{p_{LNB}}^{p_i} \left(\frac{\partial \alpha_d}{\partial s_p^*} \right)_p \left(s_{pp}^* - s_{pa}^* \right) dp \tag{10.12}$$

which is the desired result. where we have used Maxwell's relation (2.52). It follows that $CAPE_i$ is approximately given by the area between the parcel's s_p^* line and the environmental curve on a diagram with s_p^* as the abscissa and T as the ordinate. A diagram of this type is shown in **Fig. 4.3**.

It should be pointed out that the level of approximation used in deriving (4.21) can be large, with errors of up to 100% in the calculations of $CAPE_i$ for moist tropical soundings.

10.1.3   Maxwell's Equations

In a saturated atmosphere it is possible to define a saturated moist entropy, s^*, which is invariant under moist reversible processes. This quantity satisfies a modified form of the first law of thermodynamics:

$$T ds^* = du + pda - L dq^*, \tag{10.13}$$

where u is the internal energy, L is the heat of vaporization, and q^* is the saturation mixing ratio. It is also possible to define a saturated moist enthalpy h^* such that

$$h^* - u + pa - Lq^*. \tag{10.14}$$

From (10.13) and (10.14) it follows that

$$dh^* = T ds^* + \alpha dp. \tag{10.15}$$

From this it may be deduced that

$$\left(\frac{\partial h^*}{\partial p} \right)_{s^*} = \alpha \tag{10.16}$$

$$\left(\frac{\partial h^*}{\partial s^*} \right)_p = T. \tag{10.17}$$

---

[1]Note that

$$\delta \alpha = \frac{1}{1+r} \left[\frac{\partial \alpha_d}{\partial s_p^*} \delta s_p^* + \frac{\partial \alpha_d}{\partial r} \delta r \right] - \frac{\alpha_d}{(1+r)^2} \delta r$$

and the last term in this expression is simply

$$-\frac{\alpha}{1+r} \delta r.$$

Now, because q^* is a function of temperature and pressure alone, h^* is a state variable which may be expressed as a function of any other two state variables, such as p and s^*. Thus

$$\left(\frac{\partial h^*}{\partial s^*}\right)_p \left(\frac{\partial h^*}{\partial p}\right)_{s^*} = \left(\frac{\partial h^*}{\partial p}\right)_{s^*} \left(\frac{\partial h^*}{\partial s^*}\right)_p \tag{10.18}$$

Substituting (10.16) and (10.17) into the above we obtain

$$\left(\frac{\partial \alpha}{\partial s^*}\right)_p = \left(\frac{\partial T}{\partial p}\right)_{s^*} \tag{10.19}$$

10.2 Transformation of Euler's equation to an accelerating frame of reference

The Euler equation may be written

$$\frac{\partial \mathbf{u}}{\partial t} + \mathbf{u} \cdot \nabla \mathbf{u} + \mathbf{f} \wedge \mathbf{u} = -\frac{1}{\rho} \nabla p$$

and

$$\mathbf{u} \cdot \nabla \mathbf{u} = \omega \wedge \mathbf{u} + \nabla(\frac{1}{2}\mathbf{u}^2)$$

Therefore

$$\frac{\partial \mathbf{u}}{\partial t} + (\omega + \mathbf{f}) \wedge \mathbf{u} = -\frac{1}{\rho} \nabla \left(p + \frac{1}{2}\mathbf{u}^2 \right)$$

Now transform the coordinate system $(\mathbf{x}, t)$ to $(\mathbf{X}, T)$, where

$$\mathbf{x} = \mathbf{X} + \mathbf{x_c}(\mathbf{t}), \quad t = T$$

and

$$\frac{d\mathbf{x_c}}{dt} = \mathbf{c}(t) = (c_1(t), c_2(t)).$$
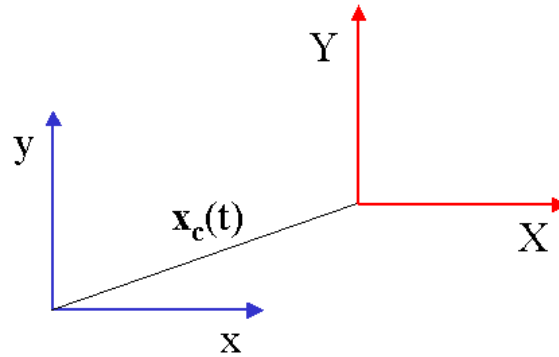
Figure 10.1:

Then

$$\frac{\partial}{\partial x} = \frac{\partial}{\partial X} \underbrace{\frac{\partial X}{\partial x}}_{=1} + \frac{\partial}{\partial Y} \underbrace{\frac{\partial Y}{\partial x}}_{=0} + \frac{\partial}{\partial T} \underbrace{\frac{\partial T}{\partial x}}_{=0}$$

$$\frac{\partial}{\partial y} = \frac{\partial}{\partial X} \underbrace{\frac{\partial X}{\partial y}}_{=0} + \frac{\partial}{\partial Y} \underbrace{\frac{\partial Y}{\partial y}}_{=1} + \frac{\partial}{\partial T} \underbrace{\frac{\partial T}{\partial y}}_{=0}$$

$$\frac{\partial}{\partial t} = \frac{\partial}{\partial X} \underbrace{\frac{\partial X}{\partial t}}_{=-c_1} + \frac{\partial}{\partial Y} \underbrace{\frac{\partial Y}{\partial t}}_{=-c_2} + \frac{\partial}{\partial T} \underbrace{\frac{\partial T}{\partial t}}_{=1}$$

$$
\begin{pmatrix} \frac{\partial}{\partial x} \\[2ex] \frac{\partial}{\partial y} \\[2ex] \frac{\partial}{\partial t} \end{pmatrix} = \begin{pmatrix} 1 & 0 & 0 \\[1ex] 0 & 1 & 0 \\[1ex] -c_1 & -c_2 & 1 \end{pmatrix} \begin{pmatrix} \frac{\partial}{\partial X} \\[2ex] \frac{\partial}{\partial Y} \\[2ex] \frac{\partial}{\partial T} \end{pmatrix},
$$

or

$$
\frac{\partial}{\partial t} = \frac{\partial}{\partial T} - \mathbf{c} \cdot \nabla_X, \quad \nabla_{\mathbf{x}} = \nabla_{\mathbf{X}}
$$

Note that although

$$
T = t, \qquad \partial/\partial T \neq \partial/\partial t.
$$

Let $\mathbf{U}$ be the velocity in the moving frame, i.e., $\mathbf{U} = \mathbf{u} - \mathbf{c}$. Then the Euler equation transforms to

$$
\left(\frac{\partial}{\partial T} - \mathbf{c} \cdot \nabla \right) (\mathbf{U} + \mathbf{c}) + (\omega + \mathbf{f}) \wedge (\mathbf{U} + \mathbf{c}) = \frac{1}{\rho} \nabla p - \nabla \left(\frac{1}{2} (\mathbf{U} + \mathbf{c})^2 \right),
$$

where

$$
\omega = \nabla_{\mathbf{x}} \wedge \mathbf{u} = \nabla_{\mathbf{X}} \wedge \mathbf{U} \qquad \text{and} \qquad \mathbf{U} \wedge \mathbf{c} = 0.
$$

Further reduction gives

$$
\frac{\partial \mathbf{U}}{\partial T} + (\omega + \mathbf{f}) \wedge \mathbf{U} = -\frac{1}{\rho} \nabla p - \nabla(\tfrac{1}{2} \mathbf{U}^2) - \frac{\partial \mathbf{c}}{\partial t} + \mathbf{c} \cdot \nabla \mathbf{U} - (\omega + \mathbf{f}) \wedge \mathbf{c} - \nabla(\mathbf{U} \cdot \mathbf{c}),
$$

using the fact that $\nabla \mathbf{c} = \mathbf{0}$ because $\mathbf{c} = \mathbf{c}(t)$. Now

$$
\nabla(\mathbf{U} \cdot \mathbf{c}) = \mathbf{U} \cdot \underbrace{\nabla \mathbf{c}}_{=0} + \mathbf{c} \cdot \nabla \mathbf{U} + \mathbf{U} \wedge \underbrace{(\nabla \wedge \mathbf{c})}_{=0} + \mathbf{c} \underbrace{(\nabla \wedge \mathbf{U})}_{=\omega}
$$

$$
\therefore \qquad \frac{\partial \mathbf{U}}{\partial T} + (\omega + \mathbf{f}) \wedge \mathbf{U} = -\frac{1}{\rho} \nabla(p + \tfrac{1}{2} \rho \mathbf{U}^2) - \mathbf{f} \wedge \mathbf{c} - \frac{d\mathbf{c}}{dt}. \tag{10.20}
$$

The vorticity equation takes the form

$$
\frac{\partial \omega}{\partial T} + \mathbf{U} \cdot \nabla(\omega + \mathbf{f}) = (\omega + \mathbf{f}) \cdot \nabla \mathbf{U} - \mathbf{c} \cdot \nabla f \tag{10.21}
$$

using

$$
\nabla \wedge (\mathbf{f} \wedge \mathbf{c}) = \mathbf{f} \underbrace{(\nabla \cdot \mathbf{c})}_{=0} - \underbrace{(\nabla \cdot \mathbf{f})\mathbf{c}}_{\substack{=0 \\ \mathbf{f}=(0,0,f) \\ \text{and } \partial f/\partial z = 0.}} + \mathbf{c} \cdot \nabla \mathbf{f} - \underbrace{\mathbf{f} \cdot \nabla \mathbf{c}}_{=0}
$$

10.3 Angular momentum and vorticity fluxes

Consider an axisymmetric flow $(u(r, z, t), v(r, z, t), w(r, z, t))$ expressed in cylindrical coordinates and assume a Boussinesq fluid for simplicity. Then

$$\frac{\partial v}{\partial t} + u\frac{\partial v}{\partial r} + w\frac{\partial v}{\partial z} + \frac{uv}{r} + fu = 0 \tag{10.22}$$

and

$$\frac{\partial}{\partial r}(\rho ur) + \frac{\partial}{\partial z}(\rho wr) = 0 \tag{10.23}$$

and the vorticity vector for this flow is

$$\omega = (\xi, \eta, \zeta) = \left(\frac{\partial v}{\partial z}, \frac{\partial u}{\partial z} - \frac{\partial w}{\partial r}, \frac{1}{r}\frac{\partial}{\partial r}(rv)\right) \tag{10.24}$$

Equation (10.22) can be written as

$$\frac{\partial v}{\partial t} + u(\zeta + f) + w\frac{\partial v}{\partial z} = 0 \tag{10.25}$$

Define the *relative circulation* to be $\Gamma = 2\pi rv$. Then (10.25) can be written

$$\frac{\partial \Gamma}{\partial t} + (2\pi ru)(\zeta + f) + w\frac{\partial \Gamma}{\partial z} = 0 \tag{10.26}$$

Thus the local rate-of-change of circulation about a circle of radius r equals the flux of vorticity into the circle plus the vertical advection of circulation at radius r.

The absolute angular momentum per unit mass is $M = rv + \frac{1}{2}fr^2$. Multiplying (10.22) by r gives

$$\frac{\partial}{\partial t}(rv) + ru\frac{\partial v}{\partial r} + rw\frac{\partial v}{\partial z} + u(v + fr) = 0 \tag{10.27}$$

Now

$$\frac{\partial}{\partial t}(rv) = \frac{\partial M}{\partial t} \quad \text{and} \quad \frac{\partial}{\partial z}(rv) = \frac{\partial M}{\partial z}, \quad \text{while} \quad \frac{\partial M}{\partial r} = r\frac{\partial v}{\partial r} + rf.$$

Thus (10.27) becomes

$$\frac{\partial M}{\partial t} + u\frac{\partial M}{\partial r} + w\frac{\partial M}{\partial z} = 0. \tag{10.28}$$

Hence M is conserved by the flow in the meridional $(r - z)$ plane. Consider now a non-axisymmetric vortex. Then (10.22) and (10.22) become

$$\frac{\partial v}{\partial t} + u\frac{\partial v}{\partial r} + \frac{v}{r}\frac{\partial v}{\partial \lambda} + w\frac{\partial v}{\partial z} + \frac{uv}{r} + fu = -\frac{1}{\rho r}\frac{\partial p}{\partial \lambda} \tag{10.29}$$

and

$$\frac{\partial}{\partial r}(ur) + \frac{\partial v}{\partial \lambda} + \frac{\partial}{\partial z}(wr) = 0 \tag{10.30}$$

In this case

$$\omega = (\xi, \eta, \zeta) = \left[\frac{1}{r}\frac{\partial w}{\partial \lambda} - \frac{\partial v}{\partial z}, \ \frac{\partial u}{\partial z} - \frac{\partial w}{\partial r}, \ \frac{1}{r}\left(\frac{\partial}{\partial r}(vr) - \frac{\partial u}{\partial \lambda} \right) \right]$$

The flux form of (10.29) is

$$\frac{\partial}{\partial t}(vr) + \frac{\partial}{\partial r}(ruv) + \frac{\partial}{\partial \lambda}(v^2) + \frac{\partial}{\partial z}(wvr) + u(v + fr) = -\frac{1}{\rho}\frac{\partial p}{\partial \lambda}. \qquad (10.31)$$

Put $v = \bar{v} + v'$, where an overbar denotes some sort of average (e.g. a Reynolds' average or an azimuthal average) for which, by definition, $\overline{v'} = 0$ then the average of (10.31) becomes

$$\frac{\partial}{\partial t}(\bar{v}r) + \frac{\partial}{\partial r}(r\overline{uv}) \ + \ (r\overline{u'v'}) + \frac{\partial}{\partial \lambda}(\bar{v}^2 + \overline{v'^2}) + \frac{\partial}{\partial z}(\overline{rwv} + r\overline{w'v'})$$

$$+ \ \bar{u}(\bar{v} + fr) + \overline{u'(v' + rf')} = -\frac{1}{\rho}\frac{\partial \bar{p}}{\partial \lambda}. \qquad (10.32)$$

Then

$$\frac{\partial \bar{v}}{\partial t} \ + \ \frac{1}{r}\frac{\partial}{\partial r}(r\overline{uv}) + \frac{1}{r}\frac{\partial}{\partial \lambda}\bar{v}^2 + \frac{\partial}{\partial z}(\overline{wv}) + \frac{\bar{u}}{r}(\bar{v} + fr)$$

$$= \ -\frac{1}{\rho}\frac{\partial \bar{p}}{\partial \lambda} - \frac{1}{r}\frac{\partial}{\partial r}(r\overline{u'v'}) - \frac{1}{r}\frac{\partial}{\partial \lambda}(\overline{v'^2}) - \overline{u'\left(\frac{v'}{r} + f' \right)} - \frac{\partial}{\partial z}(\overline{w'v'}). \ (10.33)$$

Also, the average of (10.30) gives

$$\frac{\partial}{\partial r}(\bar{u}r) + \frac{\partial \bar{v}}{\partial \lambda} + \frac{\partial}{\partial z}(\bar{w}r) = 0, \qquad (10.34)$$

so that (10.33) may be reduced to

$$\frac{\partial \bar{v}}{\partial t} + \bar{u}\left(\frac{\partial \bar{v}}{\partial r} + \frac{\bar{v}}{r} + f \right) + \bar{v}\frac{\partial \bar{v}}{\partial \lambda} + \bar{w}\frac{\partial \bar{v}}{\partial z}$$

$$= -\frac{1}{\rho}\frac{\partial \bar{p}}{\partial \lambda} - \underbrace{\frac{1}{r}\frac{\partial}{\partial r}(r\overline{u'v'}) - \overline{u'\left(\frac{v'}{r} + f' \right)} - \frac{1}{r}\frac{\partial}{\partial \lambda}(\overline{v'^2}) - \frac{\partial}{\partial z}(\overline{w'v'})}_{\text{can this be simplified in terms of vorticity?}}. \qquad (10.35)$$

Note if $(\overline{\ \ })$ is an azimuthal average, then the terms involving $\partial/\partial \lambda$ are identically zero.

If $\bar{v}$ is a Reynolds' average, we can calculate the sum of the eddy terms on the r.h.s. of (10.35) as a residual if we have two consecutive analysis of v. We can then carry out an azimuthal Fourier analysis of the equation.

Suppose that $(\bar{\varphi})$ denotes a Reynolds' average and $(\varphi)'$ a deviation therefrom, while $[\varphi]$ is an azimuthal average and $(\tilde{\varphi})$ is a deviation from this. Then ϕ can be written as:

$$\phi = [\bar{\phi}] + [\phi'] + \tilde{\bar{\phi}}, \tilde{\phi}',$$

where

- $[\overline{\phi}]$ is the symmetric part of the Reynolds' average,

- $[\phi']$ is the symmetric part of the 'sub-grid-scale' motions,

- $\widetilde{\overline{\phi}}$ is the asymmetric part of the Reynolds' average, and

- $\tilde{\phi}'$ is the asymmetric part of the 'sub-grid-scale' motions.

10.4   References

Anthes, R. A., 1974: The dynamics and energetics of mature tropical cyclones. *Rev. Geophys. Space Phys.*, **12**, 495-522.

Anthes, R. A., 1979: Modelling of tropical cyclones and their environment. *Aust. Meteor. Mag.*, **27**, 213-228.

Arakawa, A., 1969: xxx *Aust. Meteor. Mag.*, **27**, 213-228.

Betts, A. K., 1997: of tropical cyclones. *J. Atmos. Sci.*, **26**, 3-40.

Emanuel, K. A., 1986: of tropical cyclones. *J. Atmos. Sci.*, **26**, 3-40.

Emanuel, K. A., 1989: of tropical cyclones. *J. Atmos. Sci.*, **26**, 3-40.

Emanuel, K. A., 1994: Atmospheric Convection. *Oxford University Press.*, , pp580.

Gray W. M., and R. W. Jacobson, 1977: Diurnal variation of deep cumulus convection. *Mon. Wea. Rev.*, **105**, 1171-1188.

Moss and Merceret, A. K., 1976: of tropical cyclones. *J. Atmos. Sci.*, **26**, 3-40.

Ooyama, K. V., 1969: Numerical simulation of the life cycle of tropical cyclones. *J. Atmos. Sci.*, **26**, 3-40.

Ooyama, K. V., 1982: Conceptual evolution of the theory and modeling of the tropical cyclone. *J. Meteor. Soc. Japan*, **60**, 369-380.

Smith, R. K., 1968: The surface boundary layer of a hurricane. *Tellus*, **20**, 473-484.

Smith, R. K., 1980: Tropical cyclones eye dynamics. *J. Atmos. Sci.*, **37**, 1227-1232.

Smith, R. K., 2003: A simple model for the hurricane boundary layer. *Quart. J. Roy. Meteor. Soc.*, **129**, 1007-1027.

Willoughby, H. E., 1978: Forced secondary circulations in hurricanes. *J. Geophys. Res.*, **84**, 3173-3183

Willoughby, H. E., 1990: Gradient balance in tropical cyclones. *J. Atmos. Sci.*, **47**, 265-274.

Willoughby, H. E., 1995: Mature structure and motion. Chapter 2 of *A global view of tropical cyclones*. (Ed. R. L. Elsberry), World Meteorological Organization, Geneva, pp21-62

Zhu, H., and R. K. Smith. 2002: The importance of three physical processes in a three-dimensional tropical cyclone model. *J. Atmos. Sci.*, **59**, 1825-1840.

AMS Council, 2000: Policy statement: Hurricane research and forecasting. Bull. Amer. Meteor. Soc., 81, 13411346.

Andreas, E. L, and K. A. Emanuel, 2001: Effects of sea spray on tropical cyclone intensity. J. Atmos. Sci., 58, 37413751.

Bender,M. A., and I. Ginis, 2000: Real-case simulations of hurricane ocean interaction using a high-resolution coupled model: Effects on hurricane intensity. Mon. Wea. Rev., 128, 917946.

Bengtsson, L., 2001: Hurricane threats. Science, 293, 440441.

Bister, M., and K. A. Emanuel, 1998: Dissipative heating and hurricane intensity. Meteor. Atmos. Phys., 65, 233240.

Bluestein, H. B., J. G. Ladue, H. Stein, D. Speheger, and W. P. Unruh, 1993: Doppler radar wind spectra of supercell tornadoes. Mon. Wea. Rev., 121,

22002221.

Bolton, D., 1980: The computation of equivalent potential temperature. Mon. Wea. Rev., 108, 10461053.

Bosart, L. F., C. S. Velden, W. E. Bracken, J. Molinari, and P. G. Black, 2000: Environmental influences on the rapid intensification of Hurricane Opal (1995) over the Gulf of Mexico. Mon. Wea. Rev., 128, 322352.

Braun, S. A., 2002: A cloud-resolving simulation of Hurricane Bob (1991): Storm structure and eyewall buoyancy. Mon. Wea. Rev., 130, 15731592.

Businger, S., and J. A. Businger, 2001: Viscous dissipation of turbulent kinetic energy in storms. J. Atmos. Sci., 58, 37933796.

Camp, J. P., 1999: Hurricane maximum intensity: Past and present. M.S. thesis, Colorado State University, 147 pp.

, and M. T. Montgomery, 2001: Hurricane maximum intensity: Past and present. Mon. Wea. Rev., 129, 17041717.

Chen, Y., and M. K. Yau, 2001: Spiral bands in a simulated hurricane. Part I: Vortex Rossby wave verification. J. Atmos. Sci., 58, 2128 2145.

DeCosmo, J., K. B. Katsaros, S. D. Smith, R. J. Anderson, W. A. Oost, K. Bumke, and H. Chadwick, 1996: Airsea exchange of water vapor and sensible heat: The Humidity Exchange Over the Sea (HEXOS) results. J. Geophys. Res., 101, 12 00112 016.

DeMaria, M., 1996: The effect of vertical shear on tropical cyclone intensity change. J. Atmos. Sci., 53, 20762087.

Eliassen, A., 1951: Slow thermally or frictionally controlled meridional circulation in a circular vortex. Astrophys. Norv., 5, 19 60.

Emanuel, K. A., 1986: An airsea interaction theory for tropical cyclones. Part I: Steady-state maintenance. J. Atmos. Sci., 43, 585604.

, 1988: The maximum intensity of hurricanes. J. Atmos. Sci., 45, 11431155.

, 1989: The finite-amplitude nature of tropical cyclogenesis. J. Atmos. Sci., 46, 34313456.

, 1995a: The behavior of a simple hurricane model using a convective scheme based on subcloud-layer entropy equilibrium. J. Atmos. Sci., 52, 39603968.

, 1995b: Sensitivity of tropical cyclones to surface exchange coefficients and a revised steady-state model incorporating eye dynamics. J. Atmos. Sci., 52, 39693976.

, 2000: A statistical analysis of tropical cyclone intensity. Mon. Wea. Rev., 128, 11391152.

Fairall, C. W., J. D. Kepert, and G. J. Holland, 1994: The effect of sea spray on surface energy transports over the ocean. Global Atmos. Ocean Syst., 2, 121142.

Fiedler, B. H., 1994: The thermodynamic speed limit and its violation in axisymmetric numerical simulations of tornado-like vortices. Atmos.Ocean, 32, 335359.

, and R. Rotunno, 1986: A theory for the maximum windspeeds in tornado-like vortices. J. Atmos. Sci., 43, 23282340.

Frank, W. M., and E. A. Ritchie, 1999: Effects of environmental flow upon tropical cyclone structure. Mon. Wea. Rev., 127, 2044 2061.

, and , 2001: Effects of vertical wind shear on the intensity and structure of numerically simulation hurricanes. Mon. Wea. Rev., 129, 22492269.

Fulton, J. D., 2001: Insights into the hurricane vortex using a high resolution numerical simulation of Hurricane Bob (1991). M.S. thesis, Colorado State University, 84 pp.

Gray, S. L., 1998: Analysis of the eyes formed in simulated tropical cyclones and polar lows. Quart. J. Roy. Meteor. Soc., 124, 2357 2375.

Gray, W. M., 1968: Global view of tropical disturbances and storms. Mon. Wea. Rev., 96, 669700.

Guinn, T. A., and W. H. Schubert, 1993: Hurricane spiral bands. J. Atmos. Sci., 50, 33803403.

Halliday, D., and R. Resnick, 1988: Fundamentals of Physics, 3d ed. John Wiley and Sons, 977 pp.

Hausman, S. A., 2001: Formulation and sensitivity analysis of a nonhydrostatic, axisymmetric tropical cyclone model. Atmospheric Science Paper 701, Dept. of Atmospheric Science, Colorado State University, 210 pp.

Heisler, H., 1995: Advanced Engine Technology. Arnold, 794 pp.

Holton, J. R., 1992: An Introduction to Dynamic Meteorology. 3d ed. Academic Press, 511 pp.

Hoskins, B. J., and F. P. Bretherton, 1972: Atmospheric frontogenesis models: Mathematical formulation and solution. J. Atmos. Sci., 29, 1137.

Jacob, S. D., L. K. Shay, A. J. Mariano, and P. G. Black, 2000: The 3D oceanic mixed layer response to Hurricane Gilbert. J. Phys. Oceanogr., 30, 14071429.

Jin, D. Z., and D. H. E. Dubin, 1998: Regional maximum entropy theory for vortex crystal formation. Phys. Rev. Lett., 80, 4434 4437.

Jones, S. C., 1995: The evolution of vortices in vertical shear. I: Initially barotropic vortices. Quart. J. Roy. Meteor. Soc., 121, 821851.

Jordan, C. L., 1958: Mean soundings for the West Indies area. J. Meteor., 15, 9197.

Kleinschmidt, E., 1951: Grundlagen einer Theorie der Tropischen Zyklonen (Basic principles for a theory of tropical cyclones). Arch. Meteor. Geophys. Bioklimatol., A4, 5372.

Klemp, J. B., and R. B. Wilhelmson, 1978: The simulation of threedimensional convective storm dynamics. J. Atmos. Sci., 35, 10701096.

Knutson, T. R., and R. E. Tuleya, 1999: Increase hurricane intensities with CO_2-induced warming as simulated using the GFDL hurricane prediction system. Climate Dyn., 15, 503519.

Kossin, J. P., and M. D. Eastin, 2001: Two distinct regimes in the kinematic and thermodynamic structure of the hurricane eye and eyewall. J. Atmos. Sci., 58, 10791090.

, and W. H. Schubert, 2001: Mesovortices, polygonal flow patterns, and rapid pressure falls in hurricane-like vortices. J. Atmos. Sci., 58, 21962209.

LeeJoice, R. N., 2000: Hurricane inner-core structure as revealed by GPS dropwindsondes. M.S. thesis, Colorado State University, 56 pp.

Lilly, D. K., 1962: On the numerical simulation of buoyant convection. Tellus, 14, 148172.

Liu, Y., D.-L.Zhang, and M. K. Yau, 1999: A multiscale numerical study of Hurricane Andrew (1992). Part II: Kinematics and innercore structures. Mon. Wea. Rev., 127, 25972616.

Lorenz, R. D., J. I. Lunine, P. G. Withers, and C. P. McKay, 2001: Titan, Mars and Earth: Entropy production by latitudinal heat transport. Geophys. Res. Lett., 28, 415418.

Malkus, J. S., and H. Riehl, 1960: On the dynamics and energy transformations in steady-state hurricanes. Tellus, 12, 120.

Malkus, W. V. R., and G. Veronis, 1958: Finite amplitude cellular convection. J. Fluid Mech., 4, 225260.

McIntyre, M. E., 1992: Isentropic distributions of potential vorticity and their relevance to tropical cyclone dynamics. Tropical Cyclone Disasters: Proceedings of ISCU/WMO International Symposium, J. Lighthill et al., Eds., Peking University Press, 143 156.

Michalke, A., and A. Timme, 1967: On the inviscid instability of certain two-dimensional vortex-type flows. J. Fluid Mech., 29, 647666.

Mo ller, J. D., and M. T. Montgomery, 2000: Tropical cyclone evolution via potential vorticity anomalies in a three-dimensional balance model. J. Atmos. Sci., 57, 33663387.

, and L. J. Shapiro, 2002: Balance contributions to the intensi- fication of Hurricane Opal as diagnosed from a GFDL model forecast. Mon. Wea. Rev., 130, 18661881.

Montgomery, M. T., and R. J. Kallenbach, 1997: A theory for vortex Rossby-waves and its application to spiral bands and intensity changes in hurricanes. Quart. J. Roy. Meteor. Soc., 123, 435 465.

, V. A. Vladimirov, and P. V. Denissenko, 2002: An experimental study on hurricane mesovortices. J. Fluid Mech., 471, 132.

OBrien, D. M., 1997: A yardstick for global entropy flux. Quart. J. Roy. Meteor. Soc., 123, 243260.

Ooyama, K. V., 2001: A dynamic and thermodynamic foundation for modeling the moist atmosphere with parameterized microphysics. J. Atmos. Sci., 58, 20732102.

Ozawa, A., and H. Ohmura, 1997: Thermodynamics of a global-mean state of the atmosphere: A state of maximum entropy increase. J. Climate, 10, 441445.

Paltridge, G. W., 2001: A physical basis for a maximum thermodynamic dissipation of the climate system. Quart. J. Roy. Meteor. Soc., 127, 305313.

Persing, J., M. T. Montgomery, and R. E. Tuleya, 2002: Environmental interactions in the GFDL hurricane model for Hurricane Opal. Mon. Wea. Rev., 130, 298317.

Roll, H. V., 1965: Physics of the Marine Atmosphere. Academic Press, 426 pp.

Rotunno, R., and K. A. Emanuel, 1987: An airsea interaction theory for tropical cyclones. Part II: Evolutionary study using a nonhydrostatic axisymmetric

numerical model. J. Atmos. Sci., 44, 542561.

Sawada, Y., 1981: A thermodynamic variational principal in nonlinear non-equilibrium phenomena. Prog. Theor. Phys., 66, 6876.

Schecter, D. A., D. H. E. Dubin, K. S. Fine, and C. F. Driscoll, 1999: Vortex crystals from 2D Euler flow: Experiment and simulation. Phys. Fluids, 11, 905914.

Schubert, W. H., M. T. Montgomery, R. K. Taft, T. A. Guinn, S. R. Fulton, J. P. Kossin, and J. P. Edwards, 1999: Polygonal eyewalls, asymmetric eye contraction, and potential vorticity mixing in hurricanes. J. Atmos. Sci., 56, 11971223.

, S. A. Hausman, M. Garcia, K. V. Ooyama, and H.-C. Kuo, 2001: Potential vorticity in a moist atmosphere. J. Atmos. Sci., 58, 31483157.

Shapiro, L. J., 1983: The asymmetric boundary layer flow under a translating hurricane. J. Atmos. Sci., 40, 19841998.

Shay, L. K., A. J. Mariano, S. D. Jacob, and E. H. Ryan, 1998: Mean and near-inertial ocean current response to Hurricane Gilbert. J. Phys. Oceanogr., 28, 858889.

Smagorinsky, J., 1963: General circulation experiments with the primitive equation. I: The basic experiment. Mon. Wea. Rev., 91, 99164.

Smith, R. K., 2003: A simple model for the hurricane boundary layer. Quart. J. Roy. Meteor. Soc., 129, 10071027.

Stephens, G. L., and D. M. OBrien, 1993: Entropy and climate. I: ERBE observations of the entropy production of the earth. J. Roy. Meteor. Soc., 119, 121152.

Wang, Y., 2002a: Vortex Rossby waves in a numerically simulated tropical cyclone. Part I: Overall structure, potential vorticity, and kinetic energy budgets. J. Atmos. Sci., 59, 12131238.

, 2002b: Vortex Rossby waves in a numerically simulated tropical cyclone. Part II: The role in tropical cyclone structure and intensity changes. J. Atmos. Sci., 59, 12391262.

, and G. J. Holland, 1996: The beta drift of baroclinic vortices. Part I: Adiabatic vortices. J. Atmos. Sci., 53, 411427.

Willoughby, H. E., 1990: Gradient balance in tropical cyclones. J. Atmos. Sci., 47, 265274.

, 1998: Tropical cyclone eye thermodynamics. Mon Wea. Rev., 126, 16531680.

, J. A. Clos, and M. G. Shoreibah, 1982: Concentric eye walls, secondary wind maxima, and the evolution of the hurricane vortex. J. Atmos. Sci., 39, 395411.

Yamasaki, M., 1983: A further study of the tropical cyclone without parameterizing the effects of cumulus convection. Pap. Meteor. Geophys., 34, 221260.

Zhang, D.-L., Y. Liu, and M. K. Yau, 2000: A multiscale numerical study of Hurricane Andrew (1992). Part III: Dynamically induced vertical motion. Mon. Wea. Rev., 128, 37723788.

, , and , 2002: A multiscale numerical study of Hurricane Andrew (1992). Part V: Inner-core thermodynamics. Mon. Wea. Rev., 130, 27452763.

————————-

Anthes, R. A., 1982: Tropical Cyclones: Their Evolution, Structure, and Effects. Meteor. Monogro., No. 41, Amer. Meteor. Soc., 208 pp.

Bister, M., 2001: Effect of peripheral convection on tropical cyclone formation. J. Atmos. Sci., in press.

, and K. Emanuel, 1998: Dissipative heating and hurricane intensity. Meteor. Atmos. Phys., 65, 223240.

Camp, J. P., 1999: Hurricane maximum intensity: Past and present. M. S. thesis, Dept. of Atmospheric Sciences, Colorado State University, 147 pp.

Cione, J. J., P. G. Black, and S. H. Houston, 2000: Surface observations in the hurricane environment. Mon. Wea. Rev., 128, 15501561.

DeMaria, M., and J. Kaplan, 1999: An updated Statistical Hurricane Intensity Prediction Scheme (SHIPS) for the Atlantic and Eastern North Pacific basins. Wea. Forecasting, 14, 326337.

Dodge, P., R. W. Burbee, and F. D. Marks Jr., 1999: The kinematic structure of a hurricane with sea level pressure less than 900 mb. Mon. Wea. Rev., 127, 9871004.

Emanuel, K., 1986: An airsea interaction theory for tropical cyclones. Part I: Steady state maintenance. J. Atmos. Sci., 43, 585 604.

, 1988a: The maximum potential intensity of hurricanes. J. Atmos. Sci., 45, 11431155.

, 1988b: Towards a general theory of hurricanes. Amer. Sci., 76, 371379.

, 1989: The finite-amplitude nature of tropical cyclogenesis. J. Atmos. Sci., 46, 34313456.

, 1991: The theory of hurricanes. Annu. Rev. Fluid Mech., 23, 179196.

, 1995a: The behavior of a simple hurricane model using a convective scheme based on subcloud-layer entropy equilibrium. J. Atmos. Sci., 52, 39603968.

, 1995b: Sensitivity of tropical cyclones to surface exchange coefficients and a revised steady-state model incorporating eye dynamics. J. Atmos. Sci., 52, 39693976.

, 1997: Some aspects of hurricane inner-core dynamics and energetics. J. Atmos. Sci., 54, 10141026.

, 1999: Thermodynamic control of hurricane intensity. Nature, 401, 665669.

, K. Speer, R. Rotunno, R. Srivastava, and M. Molina, 1995: Hypercanes: A possible link in global extinction scenarios. J. Geophys. Res., 100, 13 75513 765.

Frank, W. M., 1977: The structure and energetics of the tropical cyclone I. Storm structure. Mon. Wea. Rev., 105, 11191135.

Gray, S., 1994: Theory of mature tropical cyclones: A comparison between Kleinschmidt (1951) and Emanuel (1986). JCMM Rep. 40, 50 pp. [Available from Joint Centre for Mesoscale Meteorology, University of Reading, P.O. Box 240, Reading, Berkshire RG6 2FN, United Kingdom.]

Guinn, T. A., and W. H. Schubert, 1993: Hurricane spiral bands. J. Atmos. Sci., 50, 33803403.

Hawkins, H. F., and D. T. Rubsam, 1968: Hurricane Hilda, 1964. 2. Structure and budgets of the hurricane on October 1, 1964. Mon. Wea. Rev., 96, 617636.

Holland, G. J., 1997: The maximum potential intensity of tropical cyclones. J. Atmos. Sci., 54, 25192541.

Jordan, C. L., 1958: Mean soundings for the West Indies area. J. Meteor., 15, 9197.

Kleinschmidt, E., 1951: Grundlagen einer theorie der tropischen zyklonen. Arch. Meteor. Geophys. Bioklimatol., A4, 5372.

Knutson, T. R., and R. E. Tuleya, 1999: Increased intensities with CO2-induced warming as simulated using the GFDL hurricane prediction system. Climate Dyn., 15, 503519.

Malkus, J. S., and H. Riehl, 1960: On the dynamics and energy transformations in steady-state hurricanes. Tellus, 12, 120.

Miller, B. I., 1958: On the maximum intensity of hurricanes. J. Meteor., 15, 184195.

Moeller, J. D., and M. T. Montgomery, 1999: Vortex Rossby waves and hurricane intensification in a barotropic model. J. Atmos. Sci., 56, 16741687.

Montgomery, M. T., and R. J. Kallenbach, 1997: A theory for vortex Rossby-waves and its application to spiral bands and intensity changes in hurricanes. Quart. J. Roy. Meteor. Soc., 123, 435 465.

, and J. Enagonio, 1998: Tropical cyclogenesis via convectively forced vortex Rossby waves in a three-dimensional quasigeostrophic model. J. Atmos. Sci., 55, 31763207.

Ooyama, K., 1969: Numerical simulation of the life cycle of tropical cyclones. J. Atmos. Sci., 26, 340.

Rosenthal, S. L., and M. S. Moss, 1971: Numerical experiments of relevance to Project STORMFURY. NOAA Tech. Memo. ERL NHRL-95, Coral Gables, FL, 52 pp.

Rotunno, R., and K. A. Emanuel, 1987: An airsea interaction theory for tropical cyclones. Part II: Evolutionary study using a nonhydrostatic axisymmetric numerical model. J. Atmos. Sci., 44, 542561.

Schade, L. R., 2000: Tropical cyclone intensity and sea surface temperature. J. Atmos. Sci., 57, 31223130.

Schubert, W. H., and J. J. Hack, 1982: Inertial stability and tropical cyclone development. J. Atmos. Sci., 39, 16871697.

Shay, L. K., P. G. Black, A. J. Mariano, J. D. Hawkins, and R. L. Elsberry, 1992: Upper ocean response to Hurricane Gilbert. J. Geophys. Res., 97, 20 22720 248.

Willoughby, H. E., 1998: Tropical cyclone eye dynamics. Mon. Wea. Rev., 126, 30533067.

, D. P. Jorgensen, R. A. Black, and S. L. Rosenthal, 1985: Project STORMFURY: A scientific chronicle 19621983. Bull. Amer. Met. Soc., 66, 505514.